Parametrization of a lithium-ion battery

ELSA ARKSAND

Master of Science Thesis

Parametrization of a lithium-ion battery

Author:
Elsa Arksand

Supervisor at Scania CV AB:
PhD Alexander Bessman

Examinator at KTH:
Prof. Göran Lindbergh

July 2, 2021

Host company: Scania CV AB

KTH Royal Institute of Technology School of Engineering Sciences in Chemistry, Biotechnology and Health Department of Chemistry- Division of Applied Electrochemistry Chemistry

100 44 Stockholm, Sweden

Abstract

Battery models are used to represent batteries. For purposes like battery management systems, empirical based models like the equivalent circuit models are widely used. These models have downsides regarding for example inability to simulate internal states and parametrization time that make engineers look at physics-based models as an alternative. The physics-based models are made up of physical relationships that offer insights into what is happening inside the battery. These are too computationally demanding to be used for certain applications, like battery managements systems. The Single Particle Model (SPM) is a physics-based model that is utilized in this thesis project. The aim of the project is to find a method to parametrize the SPM for fresh commercial cylindrical HTPFR18650 1100mAh 3.2V lithium iron phosphate cells. Literature survey and experiments were used to extract the parameter values.

17 parameters were selected from the literature survey since they could be used to parametrize the model. Geometrical parameters were found through a cell opening. Three types of non-destructive experiments inspired by literature were performed to extract values for the other non-geometric parameters. A low-rate cycling test was performed to get pseudo-OCV curve and to extract capacity related parameters. A sensitivity analysis is done for the GITT and the Pulse test for the parameters that were connected to the transport and kinetic phenomena. Python mathematical battery modelling (PyBaMM) was used to simulate the experiments. The Prada 2013 parameter set was be used as default values. The default values for the selected parameters were replaced by the values found through experiments.

The sensitivity analysis showed that some of the selected parameters were sensitive while others were not. The parameters were extracted through physical relations and through curve fitting procedures during discharge. Values for 14 out of the 17 parameters were extracted in the method. The parametrized model was validated against two potential applications, one for a battery electric vehicle and the other for a mild hybrid.

The parametrized model showed that the negative particle radius cannot be found through the proposed parametrization procedure. The simulation matched the experimental data better for discharging cells than charging cells.

Several improvements for future work have been suggested such as extending the sensitivity analysis, obtaining the OCV-curve from GITT instead of low-rate cycling, having stricter bounds for the curve fitting as well as creating more optimal tests to extract the parameter values.

Key words: Parametrization, LiFePO4, Single particle model, Li-ion battery, Pseudo-OCV, GITT, Pulse test

Sammanfattning

Batterimodeller används för att representera batterier. För ändamål som batterihanteringssystem används idag främst empiriska modeller som representerar ett batteri med en motsvarande kretsmodell. Några nackdelar för dessa modeller ligger i dess oförmåga att simulera interna tillstånd och en tidskrävande parametriseringsprocess. Dessa nackdelar motiverar ingenjörer att vända sig till modeller som är baserade på fysiska lagar som ett alternativ eftersom de kan ge insikt i vad som händer inuti batteriet. Batterimodellerna som är baserade på de fysiska lagarna har alltför krävande beräkningar för att kunna användas för vissa applikationer, som batterihanteringssystem. Singel-partikelmodellen (SPM) är en fysikbaserad modell som används i detta avhandlingsprojekt. Syftet med projektet var att hitta en metod för att parametrisera SPM för nya kommersiella cylindriska HTPFR18650 1100mAh 3.2V litiumjärnfosfatceller. En litteraturundersökning och experiment användes för att extrahera parametervärdena.

17 parametrar valdes från litteraturundersökningen eftersom de kunde användas för att parametrisera modellen. Geometriska parametrar hittades genom en cellöppning. Tre typer av icke-destruktiva experiment som var inspirerade av litteraturen utfördes för att extrahera värden för de andra icke-geometriska parametrarna. Ett cykeltest med låg strömhastighet utfördes för att få en pseudo-OCV-kurva och för att extrahera kapacitetsrelaterade parametrarna. En känslighetsanalys genomfördes för galvanostatisk intermittent titreringsteknik testet (GITT) och pulstestet för de parametrar som var kopplade till transport- och kinetiska fenomen. Python matematisk batterimodellering (PyBaMM) användes för att simulera experimenten. Parametersamlingen Prada 2013 användes som standardvärden. Standardvärdena för de valda parametrarna ersattes av de värden som hittades genom experiment.

Känslighetsanalysen visade att några av de valda parametrarna var känsliga för experimenten medan andra inte var det. Parametrarna extraherades genom fysiska relationer och genom att anpassa parametervärde för simuleringen så att den passar den experimentella datan under urladdningsförloppet. Värden för 14 av de 17 parametrarna extraherades i metoden. Den parametriserade modellen validerades mot två potentiella applikationer, en för ett batteri-elfordon och den andra för ett mild-hybridfordon.

Den parametriserade modellen visade att den negativa partikelradien inte kan hittas med den föreslagna parametriseringsmetoden. Simuleringen visade sig också matchade den experimentella datan bättre under urladdning av cellerna jämfört till uppladdning.

Flera förbättringar för framtida arbete har föreslagits, såsom att utvidgning av känslighetsanalysen, att erhålla OCV-kurvan från GITT istället för att använda pseudo-OCV-kurvan, att använda strängare gränser vid kurvanpassningarna samt att skapa mer optimala tester för att extrahera parametervärdena.

Nyckelord: Parametrization, LiFePO4, enkelpartikelmodell, Li-ion-batteri, Pseudo-OCV, GITT, Pulstest

Acknowledgements

Table of contents

List of symbols and acronyms

Symbol	Description	Symbol	Description
t_+	Electrode thickness	$D_{s,-}$	Negative electrode diffusivity
w_+	Electrode width	r_+	Positive particle radius
h_+	Electrode height	r_-	Negative particle radius
$t_{CC,+}$	Positive current collector thickness	$i_{0,+}$	Exchange current density in positive electrode
$t_{CC,-}$	Negative current collector thickness	$i_{0,-}$	Exchange current density in negative electrode
t_s	Separator thickness	k_+	Reaction rate coefficient
e_+	Active particles volume fraction in the positive electrode	e_-	Active particles volume fraction in the negative electrode
k_-	Reaction rate coefficient	σ_+	Positive electrode conductivity
R	Cell resistance	σ_-	Negative electrode conductivity
$X_{0\%}$, $z_{+,min}$	Stoichiometry of lithium in positive electrode in 0% SOC	$X_{100\%}$, $z_{+,max}$	Stoichiometry of lithium in positive electrode in 100% SOC
$Y_{100\%}$, $z_{-,max}$	Stoichiometry of lithium in negative electrode in 100% SOC	k_{f+}	Factor introduced to fit the reaction rate in the positive electrode
$Y_{0\%}$, $z_{-,min}$	Stoichiometry of lithium in negative electrode in 0% SOC	k_{f-}	Factor introduced to fit the reaction rate in the negative electrode
$D_{s,+}$	Positive electrode diffusivity	I	Current
t	Time	Q_{cell}	Capacity
Q_+	Total available capacity in the positive electrode	Q_{max}	Maximum capacity
Q_-	Total available capacity in the negative electrode		

Acronym	Description
LFP	Lithium iron phosphate
LIB	Lithium-ion battery
LFP/C	Lithium iron phosphate and graphite
BEV	Battery electric vehicle
HEV	Hybrid electric vehicle
ICE	Internal combustion engine
GHG	Greenhouse gas
DFN	Doyle Fuller Newman model
CO_2	Carbon dioxide
SPM	Single particle model
ECM	Equivalent circuit model
BMS	Battery management system
GITT	Galvanostatic intermittent titration technique
SOH	State of health
SOC	State of charge

1. INTRODUCTION

The anthropogenic climate change is a threat to the world as it is known today. Along with the emissions of heat-accumulating greenhouse gases (GHG), such as carbon dioxide (CO_2), the global average temperature has risen [1]. In 2019, the global average temperature had increased by 0.95 ℃ compared to the average during the past century [2]. To make the impacts of climate change less severe, our way of living needs to be adapted and mitigated through innovations and transitions to new solutions and lower GHG emissions. The Paris agreement has been signed by leaders worldwide but more need to be done [3],[4].

One of the world's largest GHG emitting sectors is the transport sector. The road transport sector is responsible for 11.9 % of global GHG emissions [3]. This is mostly due to the combustion of fossil fuels such as petrol and diesel for energy. By changing the source of energy, it is possible to decarbonize this sector which would have a large effect on the global emissions and by that the severity of climate change. 60 % of the road transport emissions comes from passenger travels (cars, motorcycles and buses) while the remaining 40 % comes from road freight (trucks) [3]. In Sweden, 2016, the total transport sector is the largest GHG emitter per sector with 20 million tonnes of CO_2-equivalents [4]. Fossil fuels are neither sustainable nor renewable and our sources of energy need to be shifted to more sustainable and renewable alternatives [5].

Electrification is one way of tackling the GHG emissions from the transport sector. Other solutions are to use for example, biofuels or E-fuels. There is a paradigm shift taking place regarding the transition to non-fossil fuels and infrastructure that can support the new energy system. Several studies point to the use of renewable energy and new technologies in the new generation of transport systems. Electrochemical solutions like batteries and fuel cells are promising solutions to electrifying the transport sector. The powertrain will likely go towards more hybrid vehicles (HEV) and electrified solutions such as electrical vehicles (EV), which increase dependency of batteries [6].

Even though the electric vehicle isn´t a recent invention, it has gotten a lot of interest and demand in the recent decade, mostly for passenger vehicles. Since the invention of the first kinds of electric vehicles, the technology has been competing with other technologies, most notable the internal combustion engine (ICE) technology that has dominated the market for the latest century. It is expected that it will be cheaper to own a BEV passenger car than an ICE within this decade [7]. With new batteries and research effort a similar development is expected to take place for the heavy-duty vehicles [7].

The main advantage of transitioning from ICE cars to hybrid-electric and electric cars is to reduce the use of petroleum, decrease the emissions of greenhouse gases and pollutants and increase the energy efficiency. The falling cost and increased energy density of lithium-ion batteries (LiBs) over the last years has also contributed in the electrification of the transport sector [9].

Batteries are complex systems that can be described in varying level of detail by models. Battery models are descriptions of a system and can for example give insights for range predictions for EVs, safety limits for charge and discharge and optimal usage conditions [10].

Conventional battery management systems (BMS) commonly use empirical electrical equivalent circuit models (ECMs) that is made up by a voltage source, capacitors, and resistors in a network with the task to mimic the current-voltage response of a battery cell. The parameters extracted from the ECMs can vary with the state-of-charge (SOC), state-of-health (SOH), temperature and current. To get data for a wide range of operating conditions, the process of extracting experimental data is time- and resource consuming. In the integration procedure of battery cells, the powertrain systems need to be adapted. This adaptation procedure is resource and time consuming and can hinder smooth technology development for example when a new battery cell with other characteristics is to be implemented. The model can only predict the behaviour of the cell within these operating conditions, data cannot be extrapolated, and factors such as degradation is challenging to capture because of the lack of electrochemical significance in the model parameters [10].

As more research and effort is put into batteries and energy storage solutions there is a desire to reduce the implementation time for adjusting the systems to new battery types and use models with electrochemical properties. Two electrochemical battery models are the Doyle-Fuller-Newman (DFN) and the single particle model (SPM). These models are made up of complex electrochemical relations and can be based on different chemistries and assumptions. The models need to be parametrized to accurately predict the behaviour of a specific type of cell. Parametrization methods and resources like PyBaMM (Python Battery Mathematical Modelling) that aims solve for electrochemical models might decrease the development time and give more accurate predictions than ECMs because of their electrochemical significance [11].

1.1 Purpose and goals

The purpose of the thesis is to acquire knowledge and about physics-based battery models, battery properties of the lithium-ion phosphate cell and challenges associated with parametrization. The vision behind the project is to transition the empirical-based models to electrochemical-based models to get the electrochemical significance and possibly lower the development time. This thesis will be a part of the vision by aiming to develop a method or process for parametrizing a SPM for a lithium iron phosphate and graphite (LFP/C) battery. PyBaMM will be used to solve the model and the parameter set Prada 2013 will be used as default parameter values. There are 84 parameters in the Prada 2013 parameter but not all parameters will be parametrized in this thesis mainly due to time restrictions but also issues with identifiability of the model. A selection of 17 parameters is chosen from a literature study and discussions with supervisors. The goals of the project are:

- Parameterize the SPM from the open source PyBaMM modelling library for commercial LFP cells.
- Parametrization will involve a literature survey as well as experimental work.
- Validate the model parametrization against standard drive cycles.

The target group for this report is Scania CV and others interested in models for LiBs.

1.2 Methodology

To fulfill the purpose of the thesis project, a literature review is done to get familiar with the topic and narrow down the project. The topics covered are different types of battery models, lithium-ion batteries, the LFP/C battery, and its characteristics followed by parametrization methods, sensitivity analysis and the open-source battery modelling tool PyBaMM.

From the literature study, three types of experiment are chosen because parameters are able to be extracted from the experimental data. A sensitivity analysis is conducted to confirm that the parameters are sensitive for the excitations in the experiments. The experiments are conducted to get the data from the cell. The parameter values are then extracted through methods found in the literature and through curve fitting. The curve fitting is done by editing the parameter values of the Prada 2013 parameter set to make the simulation in PyBaMM match the experimental data.

The edited parameter set will be used to simulate two potential application scenarios with a battery electric vehicle and a mild hybrid solution in order to investigate the accuracy and validity of the parameter set. This is done in a qualitative manner by comparing the simulations from PyBaMM with experimental data for the potential applications.

1.3 Scope and limitations

All experiments will be done on fresh commercial LFP/C cells. Cell ageing is a process that is much researched but complicated to model [12]. In this test, new cells will be used and therefore the effect of ageing is not a focus of this study. All experiments will take place at 25 °C. Some parameters (exchange current density and diffusion coefficient) are temperature dependent, but temperature dependence will not be included in the study. The parameters will be extracted from the discharge of the full cell only.

The Prada 2013 parameter set will be used as default values while 17 out of these will be edited and changed to the identified values.

2. BACKGROUND

The background provides insights into a general battery introduction followed by lithium-ion batteries and specific characteristics of the lithium iron phosphate cell which will be used in this thesis. A brief overview of battery models including ECMs, the DFN and the SPM will be introduced to give insights in how they differ from each other. The SPM will be used for the simulations in this thesis. The background will also include information about parametrization and relevant work regarding parameter selection. The background will inform the reader about terms and phenomena mentioned later in the report starting off with battery introductions.

2.1 Battery introductions

Batteries are electrochemical systems that store and release energy through electrochemical reactions. There are several different kinds of batteries consisting of different materials, types and sizes. Three common types are cylindrical, pouch and prismatic [7]. Batteries are used in a wide range of both mobile and stationary applications, like telephones, automobiles and wind power plants. There are both primary and secondary systems, where the latter is rechargeable while the former is not. The oldest rechargeable battery, the lead acid battery, is still common as starter or back-up systems in vehicles [13].

An electrochemical cell is composed of two electrodes, connected with an electrolyte. The reaction that takes place at the interface between an ionically conductive electrolyte material and the electrically conductive electrode material is a redox reaction. The current flow is the opposite direction of the electron flow.

The chemical driving force within a battery cell is the difference in potential between the two electrodes. The total difference in Gibbs free energy comes out as the difference in energy of the electrons in each electrode. The chemical driving force drives redox reactions where electrons are exchanged when one reactant is oxidized, and the other is reduced. In a galvanic cell, energy is released during the reaction while in an electrolytic cell, energy is required to drive the reaction. The chemical energy is converted to electrical energy [14]. One example of a battery cell is the Daniel cell seen in Figure 1.
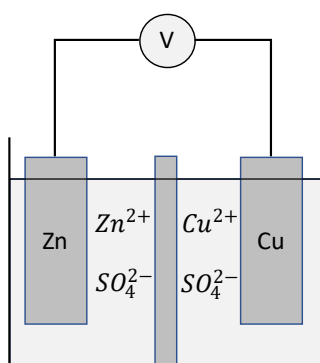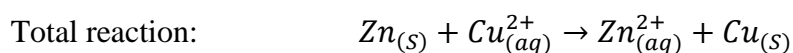

Figure 1, Daniel cell

The Daniel cell is a classic example of a battery cell. It consists of a positive copper electrode and a negative zinc electrode. Electrodes can have porous or non-porous structure. Porous structures offer a large surface area where reactions take place. The electrodes are in contact with an electrolyte consisting of $ZnSO_4(aq)$ and $H_2SO_4(aq)$ on the negative electrode side and $CuSO_4(aq)$ and $H_2SO_4(aq)$ on the positive side as well as a wire with a load. A porous separator can be used to separate the electrolytes from each other. A salt bridge could also be used to transport ions. The purpose of the electrolyte is to transport ions and heat. The separator´s purpose is to hinder mixing of species and electrical short circuits. It also allows for different electrolytes in the electrode chambers. For the Daniel cell, the electrodes act as the current collectors. If the electrodes need support in collecting the current, the separate current collectors can be used. They are usually made of highly conductive material [15].

There is a potential difference between the positive and the negative electrode. This potential difference will cause a spontaneous reaction where the negative electrode, zinc in the Daniel cell case, will oxidize and the ions at the positive electrode surface, copper for the Daniel cell case, will be reduced. When oxidation takes place at an electrode it is called an anode and when reduction takes place, the electrode is called a cathode. See the reactions taking place below.

Oxidation: $$Zn_{(S)} \rightarrow Zn^{2+}_{(aq)} + 2e^-$$

Reduction: $$Cu^{2+}_{(aq)} + 2e^- \rightarrow Cu_{(S)}$$

Total reaction: $$Zn_{(S)} + Cu^{2+}_{(aq)} \rightarrow Zn^{2+}_{(aq)} + Cu_{(S)}$$

The ions will move through the electrolyte while the electrons will move from the electrode through the wire to the electrode on the other side. An electric load, for example a light bulb,

can be connected to the wire and will light up when electrons are passed through. The reaction is driven by difference in potential which can be seen to the right of the above reactions. The open-cell voltage is described by Equation 1.

$$E^{\circ}_{cell} = \varphi_{cathode} - \varphi_{anode} \tag{1}$$

In Equation 1, E°_{cell} is the open-cell voltage, $\varphi_{cathode}$ and φ_{anode} are the potential for the cathode and the anode. For the Daniel cell, the open-cell voltage is 1.1018 V. Batteries are usually arranged in modules or packs to give a higher voltage.

The cell potential is dependent on the concentration of the dissolved species that take part in the redox reactions. This is described by the Nernst equation (2).

$$E_{cell} = E^{\circ}_{cell} + \frac{RT}{nF} ln \left(\frac{a_{ox}^{v_{ox}}}{a_{red}^{v_{red}}} \right) \tag{2}$$

The electrode and electrolytes potential differs throughout the cell. In Figure 2, different sources of resistance in the cell can be seen.
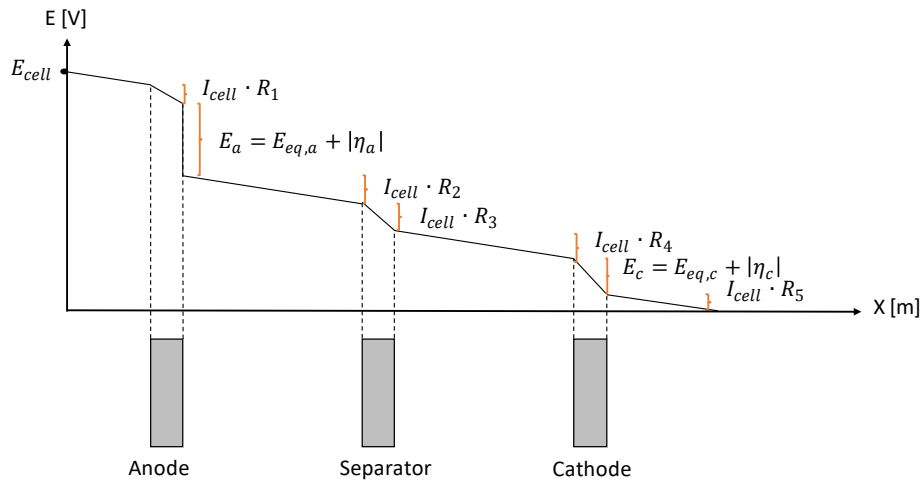

Figure 2, potential change in cell components recreated from [16]

What Figure 3 visualizes can also be expressed with Equation 3.

$$E_{cell} = E_{eq,c} - E_{eq,a} - |\eta_c| - |\eta_a| - I_{cell} \cdot (R_1 + R_2 + R_3 + R_4 + R_5) \tag{3}$$

In Equation 3, $E_{eq,c}$ and $E_{eq,a}$ are the equilibrium potentials at the cathode and anode. $|\eta_c|$ and $|\eta_a|$ are the overpotentials connected to the cathode and anode. I_{cell} is the current in the cell and the R terms represent the resistance in different parts of the cell.

The voltage change as the cell gets polarized. The cell becomes polarized when the current is not zero. The polarization can be seen a while after the circuit is broken or current is zero. Figure 3 shows the polarization curve.
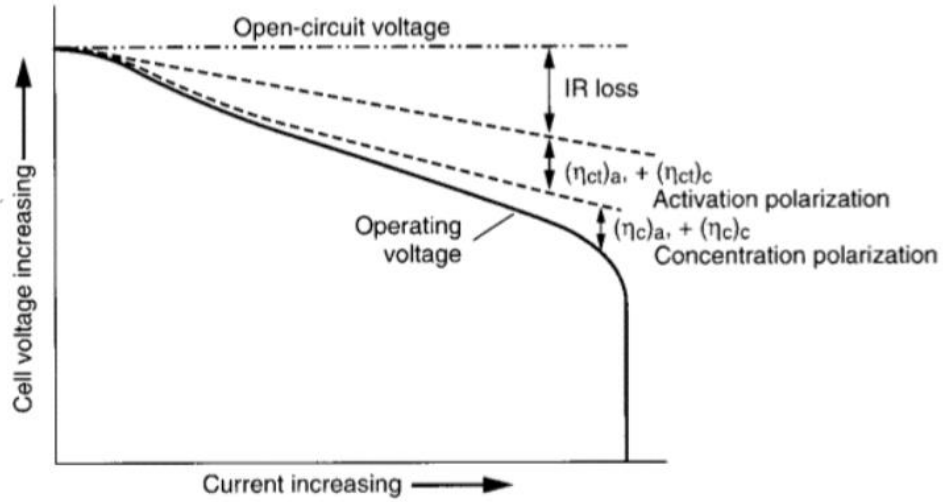
Figure 3, Cell polarization as a function of current [16]

From Figure 3 three different types of polarizations takes place. The IR-drop is due to current that flows through the cell´s internal resistance described by Ohms law. The activation polarization is related to the kinetics of the electrochemical reaction where the slowest process determines the rate of the reaction. Concentration polarization is related to resistance during the mass transfer phenomena. The mass transport in an electrolytic solution can be described by diffusion, migration, and convection by Nernst-Planck´s equation (4) [8].

$$J_i = -D_i \nabla c_i - F \frac{z_i}{|z_i|} u_i c_i \nabla \varphi + c_i \gamma \qquad (4)$$

In Equation 4, the first term is related to the diffusion, the second to the migration and the third to convection. $\nabla \varphi$ is the gradient of the potential that describe an electric field. γ is the bulk velocity. The other symbols are specific for species i. J_i is the flow of a species, D_i is the diffusion coefficient, ∇c_i is the concentration gradient, F is Faraday's constant, z_i is the charge number, u_i is the mobility. The Nernst Planck Equation 4 describes the flux of ions under the influence of both an ionic concentration gradient and an electric field [17].

To talk about current rates (C-rates) to explain which current that the cell experiences while doing experiments on battery cells are usually used. A C-rate of 1C means that a fully charged cell is discharges after 1 hour while operating at the C-rate. A C-rate of 2 C or $\frac{1}{2}$ C means that the fully charge cell is discharged after 0.5 and 2 hours, respectively.

There are several other types of batteries than the Daniel cell that uses different materials and compositions. A Ragone plot with different battery types can be seen in Figure 4.
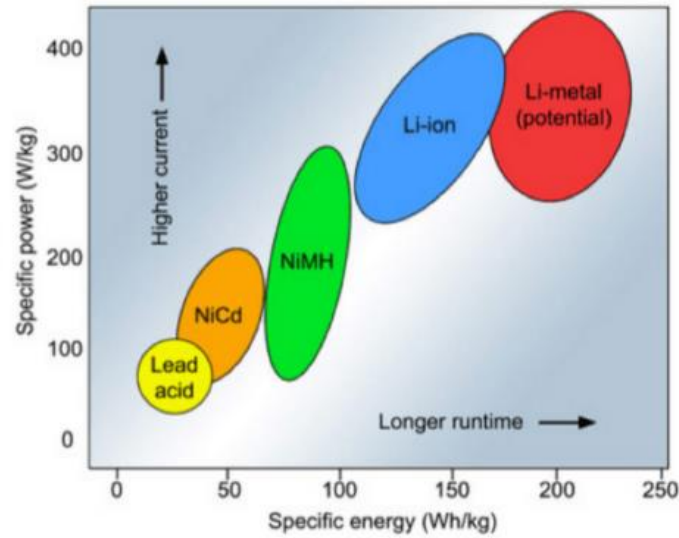
Figure 4, Ragone plot [7]

One type that has gotten a lot of focus within the automotive market is the lithium-ion batteries for on-board storage solutions [13]. From the Ragone plot in Figure 4, lithium-ion batteries (LiB) have a relatively high specific power and specific energy density. In the next part, more information about lithium-ion batteries will be covered.

2.1.1 Lithium-ion batteries

Due to their high energy and power densities, the LiB technologies are leading in the new generation of EVs and plug-in hybrid electric vehicles (PHEV) [12]. Common kinds of LiBs found in electrical vehicles are Lithium Cobalt Oxide (LCO), Lithium Manganese Oxide (LMO), Lithium Iron Phosphate (LFP) and Lithium Nickel–Manganese–Cobalt Oxide (NMC) [6]. Different electrode materials have different advantages like lower cost, higher thermal stability, longer cycle life etc that makes them useful for different applications [8]. Some benefits and drawbacks of lithium-ion batteries compared to other types of secondary battery chemistries can be seen in Table 1.

Table 1. *Some benefits and downsides to LiBs compared to other secondary battery chemistries* [8]

Benefits	Drawbacks
High operating voltage	High sensitivity to overcharging
High energy densities	Special requirement of chargers
Less cells per applications are needed	
Low self-discharge rate	

The positive electrode material of LiBs is typically a metal oxide with a layered or tunnelled structure on an aluminium current collector. The negative electrode material is typically graphitic carbon on a copper current collector. The electrolyte consists of a non-aqueous solutions [18], [19], [20]. An overview of the cell structure can be seen in Figure 5 below.
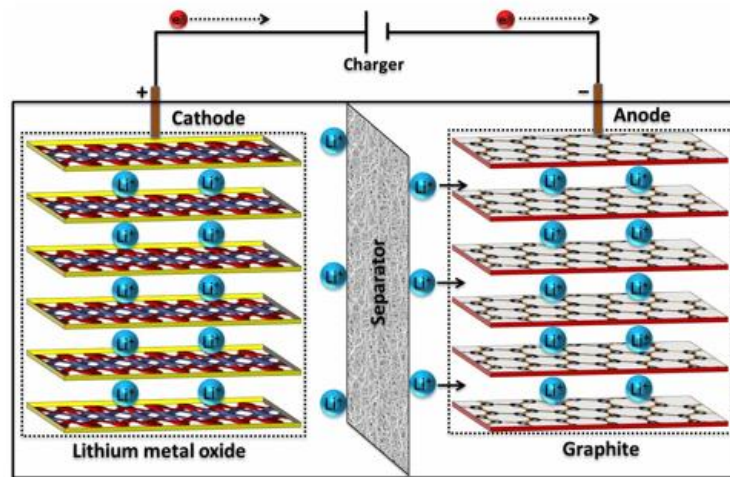
Figure 5, Lithium-ion cell [21]

Intercalation is a property of some electrode materials where the crystal structure allows the lithium ions to be inserted and removed without changing the materials structure significantly. The intercalation electrode stays intact during cycling unlike conversion electrodes where the electrodes are degraded and reformed upon cycling. This reversible intercalation/deintercalation reduces the problem of dendrite formation of lithium which provides improvements in safety and cyclability compared to other batteries [18], [19], [20]. During the charge-discharge process, the lithium ions are inserted or extracted from the layers of the active material [22]. This can be seen in Figure 6 below.
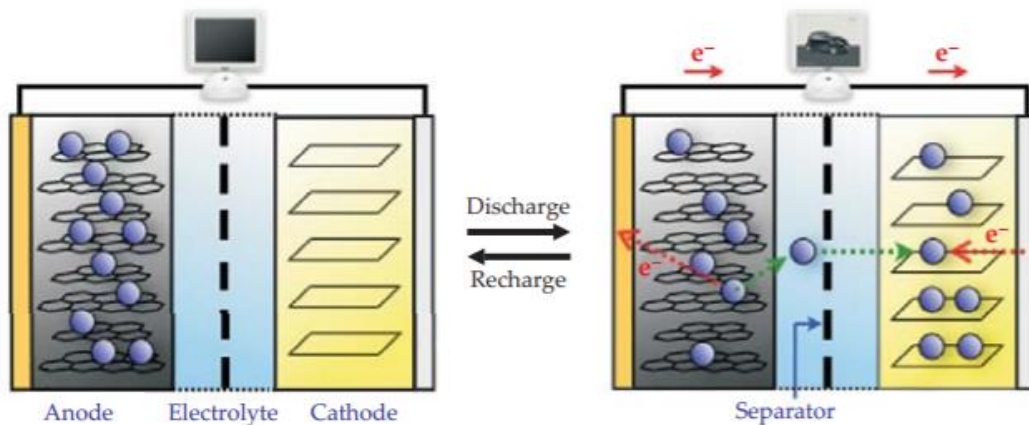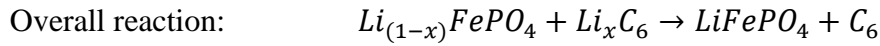

Figure 6, Charging and discharging a LiB. During discharge the lithium ions (purple) are released and transported through the electrolyte to the cathode. Electrons travel through the wire to the cathode [22].

The electrolyte is not stable for the cell voltage and decomposes to form a passivation layer, called solid electrolyte interface (SEI), at the negative electrode [23].

2.1.2 Lithium iron phosphate and graphite characteristics
One type of LiB has lithium iron phosphate as positive electrode material and graphite as negative. These lithium iron phosphate and graphite cells are usually called LFP cells. The lithium ions can be intercalated in the LFP and graphite structure [18], [19], [20].

The main electrochemical reactions taking place in this cell during charge and discharge can be seen below. The reactions are stated during discharge.

Reduction: $$Li_{(1-x)}FePO_4 + x \cdot Li^+ + e^- \rightarrow LiFePO_4$$

Oxidation: $$Li_xC_6 \rightarrow x \cdot Li^+ + C_6 + e^-$$

Overall reaction: $$Li_{(1-x)}FePO_4 + Li_xC_6 \rightarrow LiFePO_4 + C_6$$
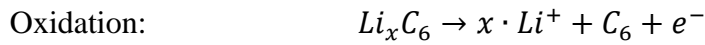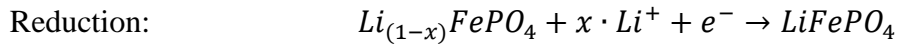
The "x" in the reactions indicate that the material can hold a variable stoichiometry of lithium between 0-1. From the reactions it can be seen that only the lithium ions move between the electrodes during charging and discharging. The name, "lithium-ion" batteries comes from this mechanism [18], [19], [20].

Graphite is a layered compound that consists of hexagonal graphene sheets of atoms. The sheets are weakly bonded through van der Waals forces [24]. See the structure of a graphite unit cell in Figure 7.
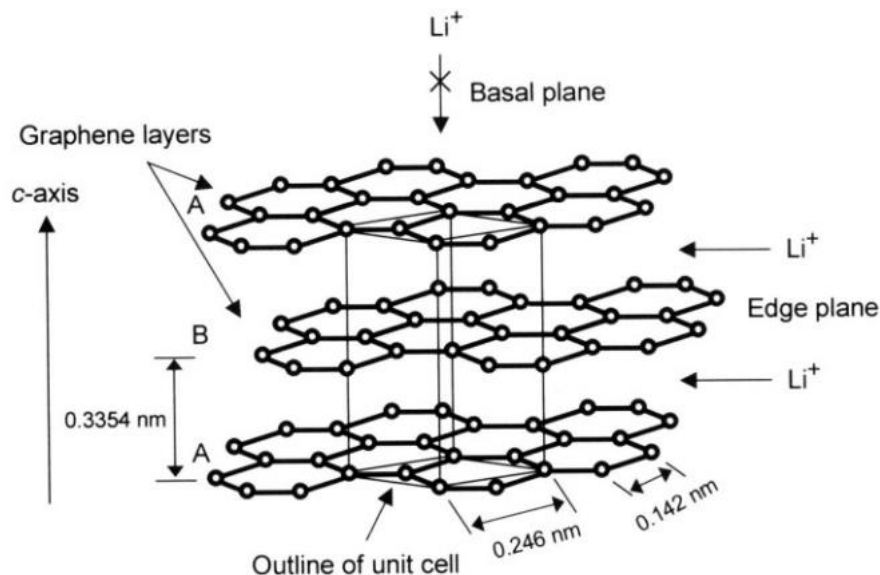

Figure 7, Crystalline structure of hexagonal graphite showing the stacking of graphene sheets and the unit cell [24]

The LFP/C cell differs from most other LiBs with its flat OCV-curve. See the OCV-curves of LFP/C, NMC/C and NMC/LTO in Figure 8 below.
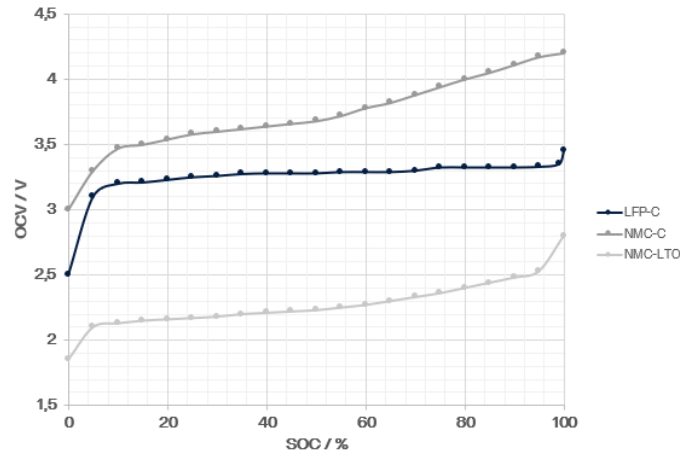
Figure 8, Typical OCV vs SOC for different lithium-ion batteries [21]

The OCV curve provides important thermodynamic information of the electrode properties after relaxation of kinetic processes. The LFP electrode has a very flat OCV curve during lithium intercalation/deintercalation through most of the two-phase reaction in the range between x=0 to x=1 in Li_xFePO_4 at room temperature [25], [26]. Two-phase regions are shown as voltage plateaus while the slopes show the phase transitions according to Gibbs' phase rule. The small "bumps" that can be seen in Figure 8 comes from the graphite electrodes staging phenomenon when Li is intercalated into the graphite layers. The full cell OCV-curve mainly exhibit the graphite characteristics [27], [19]. The flat OCV-curve in combination with path dependence [28] and inherent hysteretic behaviour [29] [26], makes the SOC difficult to determine with OCV-monitoring. The relationship between SOC and OCV is essential for battery modelling [30] and to control cell performance in battery management systems (BMS) [31], [27].

2.2 Battery models

When the demand for electric, hybrid electric and plug-in hybrid electric vehicles increases, further understanding and development of the batteries are needed to make more accurate predictions and estimations of the battery. Battery models are commonly used in BMS to make predictions and estimations about the cell. They are used to understand behaviour, discover new designs and usage scenarios for batteries. Information like the state of health (SOH), SOC and their power limits are important to understand changes in the cell like ageing to increase the lifetime of the cell. This information can help companies to protect and use the batteries in the best way and estimate the remaining performance [32]. Depending on which information is desired, there are different models to use, for example atomistic models for material optimization, continuum electrochemical engineering models to understand drive performance and manufacturing and techno-economical models that can be used to understand lifecycle impacts and costs [33]. To estimate the internal states for control systems, empirical ECMs are often used although there is a desire to integrate physics-based models with this aim.

The physics-based models are based on parameters with electrochemical meaning which can provide insights in the different electrochemical phenomena inside the battery. Two examples of physics-based models are the Doyle-Fuller-Newman (DFN) and the Single particle model (SPM). A very common type of empirical models is called Equivalent circuit models (ECM).

2.2.1 Equivalent circuit models

ECMs are used to mimic a cell for a set usage. ECMs can be build-up of resistors, capacitors, inductors, constant phase elements in different configurations. Figure 9 shows a simple schematic of a part of an electric circuit with resistors (R,s and R,p) and a capacitor (C).
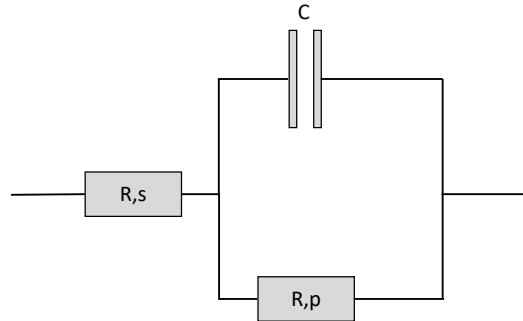

Figure 9, A simple schematic of a part of an electric circuit

By adding more elements, the model can generate more accurate and precise simulations of the battery behaviour. The disadvantage of more elements in the equivalent circuit is that more information about the cell is needed for parameterization and the CPU time for calculations is increased [34].

The empirical model can become very well adapted to the battery and give an accurate description, but it needs to be tested for all possible scenarios of which the cell should be used. This is a time-consuming process, which can take months to years. Because of the simple model structure, relatively low computational burden, and rather easy parametrization process, ECMs are used for a wide range of industry applications [35]. The simplicity of the model is also restricting it from describing the physical meaning of the states and parameters in the cell. The model is only applicable within the scenarios that it has been tested for, it is hard to extrapolate from data and explain what is physically going on. Processes like ageing are also difficult to account for in the model which could lead to unwanted effects of operation. The adaptation needs to be done again and new empirical data must be collected [35].

2.2.2 Doyle-Fuller-Newman model

The Doyle-Fuller-Newman model (DFN), also called pseudo-two-dimensional (P2D) model or the Newman model is an electrochemical model that is based on the porous electrode theory and contains a large number of parameters with physical meaning. This can give a deeper understanding into processes taking place inside the battery than the ECMs can provide. Since the DFN model is based on governing physics-based relations and conditions, it can give more insights into the processes and internal states of the battery, and it is not limited by a pre-defined scenario window as the ECMs. It is also possible to extrapolate from these models, adapt and parametrize them to different battery chemistries since they are based on the same governing equations.

The model have inputs regarding thermodynamic, geometric and kinetic properties of the cell to be able to describe a specific cell [36]. The accuracy of the input parameters has a large impact on the reliability of the DFN and other physics-based models. Not all parameter values can be transferred between cell type, chemistries and sizes, therefore a main challenge in

battery modelling is to find a set of parameters which can and cannot be transferred and how to find the values needed [36]. To identify electrochemical parameters in a fast and accurate manner is a vision of many engineers and researchers [35].

The model is complex and is described by a set of highly coupled nonlinear partial differential equations. This makes it too computationally complex for some applications, like today´s BMS. For these cases, simpler electrochemical models are of interest.

The governing equations of the DFN are related to charge conservation, molar conservation and electrochemical reactions. The boundary conditions are the current, concentration in electrolyte, concentration in electrode active material, reference potential and initial conditions [36], [37], [38].

2.2.3 Single particle model

A physics-based model that is simpler than the DFN model is the Single Particle model (SPM). The SPM describes the main phenomena taking place in a Li-ion cell: solid state diffusion, intercalation and de-intercalation and conduction. It neglects the diffusion in the electrolyte. See a simple schematic of a battery with the SPM in Figure 10.
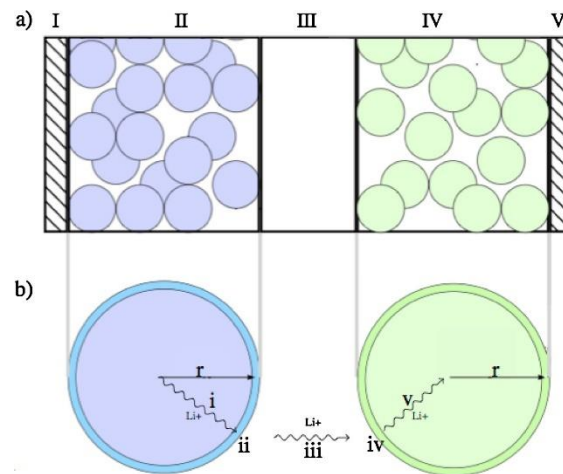

Figure 10, (a) Structure of a Li-ion cell: (I) negative current collector; (II) anode; (III) separator; (IV) cathode; (V) positive current collector. (b) single-particle model schematic [39]

It is assumed that all the particles in the electrode behave the same way and that it is sufficient to solve the model for one particle. This assumption allows for a considerable simplification in the model structure and dimension and is generally considered to be acceptable at current rates (C-rates) up to $1 - 2$ C, when electrodes are thin and highly conductive. Following the assumption, the diffusion and intercalation phenomena occur in a uniform manner in the electrodes, making it possible to model the electrodes as two spherical particles. This leads to a simpler version of the DFN model [37]. For several applications with energy optimized batteries, such as electric vehicles, the average C-rates are lower than 1C [10].

The SPM is not as computationally demanding as the DFN, but it can give more insights into the physics taking place inside of the cell than ECMs.

2.3 Parametrization of a model

While models consist of mathematical relationships and parameters that together describe a system, parametrization is related to finding the values of the parameters that makes the model describe the system in an acceptable way.

The accuracy of the parameters that build up the model have a strong impact on the reliability of the model. The parameters are specific to the cell design, geometry, and chemistry so not all parameters can be transferred between cells. Finding a suitable set of parameters that can simulate a desired aspect of a cell is a challenging task for battery modelling. To find a suitable set of parameter values, different methods can be used. One method is to fit the simulation and the model to experimental data such as terminal voltage. This method might not be feasible without good initial guesses because of the large number of parameters and the complexity of the model. Secondary, parameter values can be found in literature but there is a risk of poor model predictions if the values in different sources have different conditions. A third method would be to measure the parameters experimentally. This could potentially give more accurate model predictions for the cell but it needs robust approaches and might be technically complicated and time consuming [36].

A structural property of a model is its identifiability. That a model is identifiable means that the different parameter values must create different probability distributions of the model output. When the same model output can be attained with different parameter values, the model is non-identifiable. A model can be identifiable within certain restrictions. The requirements for the restriction are called identification conditions [40]. If there is a risk for co-dependency between parameters, then it can be difficult to have a model or find requirements where it is identifiable.

2.3.1 Related work

There are several papers available that describes different methods to estimate the parameters in ECM [41]. Methods to estimate the parameters in the DFN and SPM are scarce. Some parameters in these electrochemical-based models are possible to find through experiments but the measurements needed are complicated. The electrochemical models also involve a larger number of parameters compared to the ECM which makes the estimation more computational complex. The Gauss-Newton method for non-linear optimization and homotopy optimization has been used to estimate parameters in the SPM. QR factorisation is used in the sensitivity analysis for the DFN model in [41] where non-linear least-square optimization is used to parametrize the sensitive parameters.

2.3.2 Target parameters

While conducting analysis on electrochemical systems, the parameters describing the system can be grouped into different properties that they are related to, for example into physical, chemical and electrochemical [36]. In [41] the parameters of the DFN model is divided into thermodynamic and kinetic parameters. In [35] the groups are geometric, transport and concentration. The parameters have also been grouped regarding to which phenomena they are related like diffusive phenomena, intercalation and equilibrium related [39].

The parameter set called Prada 2013 that can be used in simulations with PyBaMM is a collection of parameters that can be used for LFP/C cells. The parameters in the set orgins from three different sources [12], [36],[42]. There are in total 84 parameters in the parameter

set that will give different effects on the simulations with PyBaMM [43]. A table with all parameter values in the Prada 2013 parameter set can be found in Appendix A.

A collection of the parameters found in [35], [36], [39] and [41] as well as other parameters who are thought to be sensitive or that could be used to parameterize the SPM can be seen in Table 2.

Table 2. *Thermodynamic, transport and kinetic parameters with literature values*

Sign	Unit	Description	Prada 2013	Literature values
t_+	μm	Electrode thickness	81	72, 52 and 80 [44]
w_+	m	Electrode width	1.78	
h_+	mm	Electrode height	64.9	
$t_{CC,+}$	m	Positive current collector thickness	1.9e-5	
$t_{CC,-}$	m	Negative current collector thickness	1e-5	
t_s	m	Separator thickness	1.8e-5	
e_+	-	Active particles volume fraction in the positive electrode	0.28485556	0.456, 0.483, and 0.354 [44]
e_-	-	Active particles volume fraction in the negative electrode	0.75	0.4-0.5 [35]
$X_{100\%}$	-	Stoichiometry of lithium in positive electrode in 100% SOC	-	-
$X_{0\%}$	-	Stoichiometry of lithium in positive electrode in 0% SOC	-	-
$Y_{100\%}$	-	Stoichiometry of lithium in negative electrode in 100% SOC	-	0.676 [45]
$Y_{0\%}$	-	Stoichiometry of lithium in negative electrode in 0% SOC	-	0.126 [38]
D_+	m^2/s	Positive electrode diffusivity	5.9e-18	8e-18 [46] 1e-12 –1e-13 [47]
D_-	m^2/s	Negative electrode diffusivity	3.3e-14	2e-9 – 1e-10 [24]
r_+	m	Positive particle radius	1e-08	-
r_-	m	Negative particle radius	5.86e-6	3-22e-6 [48] 7.28e-6 [49] 12.5e-6 [50] 1-11e-6 [35]
$i_{0,+}$	A/m^2	Exchange current density in positive electrode	Available as a function	3.14e-6 [46] 6.50e-3, 1-67e-2 and 4.73e-3 [44]
$i_{0,-}$	A/m^2	Exchange current density in negative electrode	Available as a function	2.1 [51] 3.6e-3 [45]

k_+	$m^{2.5}mol^{0.5}s$	Reaction rate coefficient	-	-
k_-	$m^{2.5}mol^{0.5}s$	Reaction rate coefficient	-	1e-11 – 2e-10 [35]
σ_+	S/m	Positive electrode conductivity	0.33795074	10e-7 –10e-8 [46] 1e-7 [47] 0.001-1 [52]
σ_-	S/m	Negative electrode conductivity	215.0	(2-1)e5 [47] 2-3e5 [53] 3e5 [46] 100 [45]
R	Ω	Cell resistance	-	

Diffusivity

The transport parameters are linked to the cell´s capability to transport particles and ions. Diffusion is the movement along concentration gradients. Atoms move in a predictable fashion to eliminate concentration differences and produce a uniform and homogeneous composition [53]. Nernst Plack equation (Equation 4) describes the diffusion in electrolytic solutions [47].

The intercalation process of lithium ions into electrodes involves several processes like the diffusion through the electrolyte, migration in the surface film, charge transfer at the electrode/electrolyte interface followed by the diffusion in electrode. While using the SPM, the mass transport in the electrolyte is assumed to be instantaneous and the transport in the electrodes are most important. In carbon electrodes the mass transport of lithium ions is regarded as a diffusive process and since the diffusion process in solids is generally slow, the rate of diffusion is limiting the overall reaction rate [24]. The diffusion coefficient, or diffusivity, of Li-ions in the electrode´s active material can be seen as a parameter of interest for a sensitivity analysis and parameter estimation of LiBs [41], [50], [35], [39], [24].

There are several methods to determine the diffusion coefficients of lithium in solids. Some examples are galvanostatic intermittent titration technique (GITT), current pulse relaxation, potential step chronoamperometry and AC impedance spectroscopy. A precise determination of the diffusivity is generally difficult to conduct, and the results depend on which kind of material and additives that make up the electrodes and the technique that is used. For some of these techniques, the variation of the open-circuit potential with lithium composition and the surface area of the sample need to be highly accurate [24].

Particle radius

The particle radius of the electrode material depends on the production. To offset the solid-phase diffusion limitation, the particle radius of the LFP active materials are usually prepared in nano-size particles [47]. The reversibility of the intercalated lithium ion in graphite is strongly dependant on the particle size of graphite [54]. Scanning electron microscopy (SEM) can be used to find a particle size distribution [44].

Reaction rate

The reaction rate in the electrode is an important kinetic parameter because it is linked to the rate limiting processes within the cell. The reaction rate is not an individual parameter in the Prada 2013 parameter set but is expressed through the exchange current densities in the

electrodes. Through the Butler-Volmer and Arrhenius equations, the connection between reaction rate and the exchange current density can be found.

$$j(\eta) = j_0 \cdot \left\{ exp\left(\frac{\alpha_a F \eta}{RT}\right) - exp\left(\frac{-\alpha_c F \eta}{RT}\right) \right\} \qquad (5)$$

The Butler Volmer equation (5) describes the current density as a function of the overpotential. j_0 is the exchange current density. F is the Faraday constant, η is the overpotential, R is the ideal gas constant, T is the temperature, and α the transfer coefficient (one for the anode and one for the cathode) [16].

Arrhenius equation (6) predicts kinetics based on thermal activation [47].

$$rate \approx e^{\left(\frac{-\Delta G}{k_B T}\right)} \qquad (6)$$

In Arrhenius equation, ΔG is the change in Gibbs free energy, k_B is the Boltzmann constant and T is the temperature.

Exchange current density
The exchange current density is the current density when the electrode is at equilibrium. Since the electrode is at equilibrium the reduction and oxidation take place at the same rate and there is no net current density. The exchange current density is dependent on the temperature, electrolyte concentration and particle surface concentration. In PyBaMM, the exchange current densities are expressed as functions of these parameters.

Pulse test and Electrochemical Impedance Spectroscopy (EIS) are alternative methods to find information about exchange current density, activation energy and reaction rate [55]. The exchange current density can be obtained from Tafel plot that can be made from the Butler-Volmer Equation (5)

A functional form of the exchange current can be used. When assuming that α=0.5 it takes the form of Equation 7 [36].

$$j_0 = k \cdot \sqrt{c_e \cdot c_s \cdot (c_s^{max} - c_s)} \qquad (7)$$

In Equation 7, j_0 is the exchange current density, k is the reaction rate, c_e is the electrolyte concentration, c_s is the electrode surface concentration and c_s^{max} is the maximum electrode surface concentration.

Electrode conductivity
The internal resistance of the cell is regarded as an important parameter in order to make a parametrization of a battery cell [39]. The cell resistance is not included as a parameter in the Prada 2013 parameter set, but it is related to the conductivities. How the resistance in a wire is related to its conductivity can be seen in Equation 8.

$$R_{cell} = \frac{l}{\sigma A} \qquad (8)$$

R_{cell} represents the internal resistance, A represents the area, σ represents the conductivity and l represents the length of the wire.

The electrical conductivity of an electrode is a material property that determines how well the material will conduct electricity. LFP is known to have poor electrical conductivity [46],[47].

Several ways to increase the electrical conductivity of the LFP electrode has been made such as adding or coating carbon to LFP electrodes and/or current collectors to increase the electrical conductivity of the electrode and lessen the contact resistance. Factors like the carbon content, the quality of the carbon coating, calendaring, and doping materials have impacts on the electrical conductivity. The low electrical conductivity can result in a considerable ohmic drop within the electrode [46], [52], [47].

Graphite has a higher electrical conductivity than LFP. The electrical conductivity is closely related to the morphology of the graphite. The smaller the particle size and the higher the surface area, the lower the conductivity [56].

3. METHOD AND THEORY

3.1 Method overview

In order to parametrize a LFP/C cell for the SPM, a step-wise procedure is taken. Starting with a literature review, followed by a simple sensitivity analysis, experiments, numerical simulations and parameter estimation.

The literature values available in the Prada 2013 parameter set was be used as initial guesses/default values while some targeted parameters, that is found in literature, will be estimated in order to find more parameter values that better describe the system. This will be done through conducting a number of experiments form which the values will be calculated from or found through a curve fitting procedure. A summarized workflow can be seen in Figure 11.
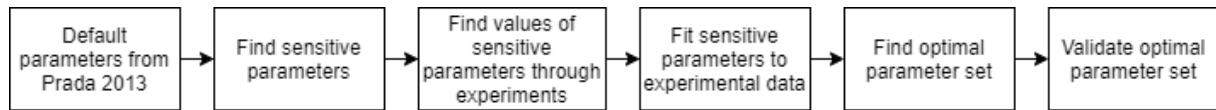

Figure 11, workflow to find optimal parameter values.

3.1.1 Literature review

To fulfil the purpose of the thesis project, a literature review is done to get familiar with the topic and narrow down the project. The topics covered are different types of battery models, lithium-ion batteries, the LFP/C battery, and its characteristics followed by parametrization methods, sensitivity analysis and PyBaMM. The databases used are mainly KTH Library and Google Scholar.

Form the literature study, three types of experiment are chosen because parameters are able to be extracted from the experimental data or used as basis for a curve fitting procedure.

3.1.2 Sensitivity analysis

A sensitivity analysis was conducted to check if the parameters are sensitive for the experiments.

For the experiments used to find the transport and kinetic parameters, a sensitivity analysis of the simulated response of a disturbance of ± 10 % in each parameter was done. To disturb the parameters by 10 % might in reality be an unrealistic disturbance if for instance, the parameters could only be within a smaller range. An alternative method is to find within

which ranges the parameters are usually found and then disturb the parameters within that range. The simpler method is chosen due to the restricted amount of time.

The SPM is based on several non-linear differential equations, like the OCV-curves and the Butler-Volmer equation [50]. Some equations and parameters show linear characteristics in some parts, but the model is mostly non-linear. To care for the non-linearity, it is possible to grid the problem and select several different points in the SOC or temperature to see where the parameters are the most sensitive. A convenient way to do this would be to check in three different points of the SOC. The sensitivity is taken in targeted SOC regions in the beginning, the centre and end of the simulation.

3.1.3 Numerical simulation

Simulations with the SPM were performed using the open-source software package Python Battery Mathematical Modelling (PyBaMM). PyBaMM can be used to solve continuum battery models using asymptotic analysis and numerical methods [11]. For the simulations in this thesis, PyBaMM v. 0.4.0 was used to solve the SPM without electrolyte. The Prada 2013 parameter set was be used as default values for the parameters. The SPM without electrolyte is based on the equations described in [37].

3.1.4 Experimental setup

LFP/C cells of the model HTPFR18650-1100mAh-3.2V were be used in the experiments. The technical parameters of the cylindrical cells received from the producers' data sheet can be seen in Figure 12.

No.	Item		Standard	Note
1	Standard Capacity		1100mAh	0.5C,(current value of 1100mA at 1C)
2	Capacity Range		1050~1200mAh	0.5C
3	Standard Voltage		3.2 V	
4	Alternating Internal Resistance		≤18mΩ	
5	Charge Conditions	Cut-off Voltage	3.65±0.05V	constant-current charge to 3.65V at 0.5C, constant voltage charge to stop until 0.01C mA
		Cut-off Current	0.01C	
6	Discharge Cut-off Voltage		2.0V	
7	Cycle Characteristic		500times（100%DOD）	the residual capacity is no less than 70% of rated capacity at 1C Charge ， 10C Discharge rate.
			1000 times（80%DOD）	
			3000 times（50%DOD）	
8	Max. charging current		5.5A	
9	Max. Continuous Discharge Current		33A	
10	Pulse Discharge Current		40A, 10s	
11	Working Temperature		Charge:0°C~55°C Discharge:-20°C~60°C	
12	Storage Temperature		-20°C ~ 45°C	Short-term storage (< 3 months)
13	Battery Weight		41 g (Approx.)	

Figure 12, Major technical parameters [57]

A total of 4 cells were used in the experiments. To see if the cells were working well, the cell voltage is tested with a multimeter before the cells are entered into the cell holder and tests started.

The cells were placed in a cell holder which is built for the experiment, see setup in Figure 13. This is a four-probe setup.
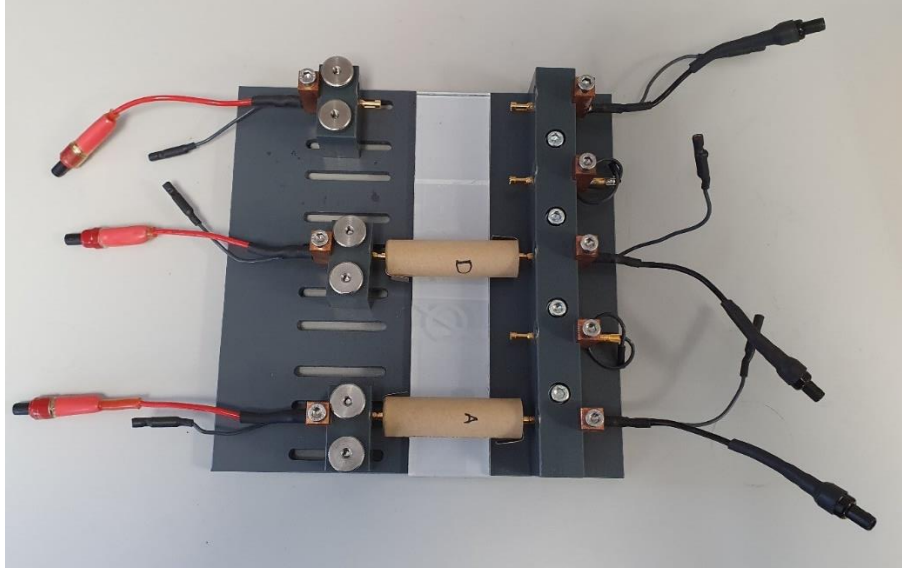
Figure 13, Cell setup

The cells and the holder were then placed in a climate chamber which keeps a constant temperature of 25 °C in steady state conditions. There was a power source that can do potentiostatic and galvanostatic experiments, a control PC with EC-lab software which was used to perform the monitoring and control of the system. A booster was used to access higher currents.

3.1.5 Parameter fitting

The experiments were conducted to get the data and the parameters were extracted through methods found in the literature, mostly [39]. Curve fitting by editing the parameter values of the Prada 2013 parameter set to make the simulation in PyBaMM match the experimental data were also performed. A non-linear least squares method was used to fit a function to data via the curve fit method of the Python library scipy.optimize [58]. Scipy version 1.5.2 was used. The formula for a least square method for a simple line, with the form y=mx+b with m being the slope and b being the intercept with the y-axis, can be seen in Equation 9.

$$y = \frac{N \sum (xy) - \sum x \sum y}{N (x^2) - (\sum x)^2} x + \frac{\sum y - m \sum x}{N} \tag{9}$$

3.2 Experimental methods

The experiments were inspired by the ones described in [39] where experiments were performed on lithium-titanate cells in order to extract parameters related to the equilibrium, diffusive and intercalation phenomena. In the paper, a reformulation of the SPM was conducted to get a minimum amount of group parameters. Three non-intensive methods were proposed to identify the parameter values that would be sufficient to parameterize the reformulated SPM. The experiments were made so that parameter values could be extracted through curve fitting methods and equations. These procedures seemed promising and were adapted for the LFP/C cells investigated in this thesis. The parameters were also adapted to match the once available in PyBaMM.

The geometric parameters $t_+, w_+, h_+, t_{CC,+}, t_{CC,-}$ and t_s will be found by measuring them during a cell opening. They are linked to the volume of the electrode and therefore also the capacity of the cell. The geometrical parameters can also be related to the resistance in the cell

according to Figure 2. The other thermodynamic parameters e_+, e_-, $X_{100\%}$, $X_{0\%}$, $Y_{100\%}$ and $Y_{0\%}$ will be found through a curve fitting procedure similar to the one described in [39]. The transport and kinetic parameters will undergo a sensitivity analysis and a curve fitting procedure to find the parameter values. See the theoretic background behind the experiments chosen and the block diagrams for the cycling, GITT and pulse test in the following sections.

3.2.1 Thermodynamic parameters via low-rate cycling

Depending on the desired resolution, the OCV can be derived from galvanostatic intermittent titration technique (GITT). This procedure is done by moving small steps in the SOC window with low currents, like C/20. This procedure can be relatively time consuming, not unusual with week-month periods, demanding depending on the number and sizes of the SOC steps that are taken. To get information of the OCV in a faster manner, a cell can be cycled at very low currents, such as C/25, to generate a pseudo-OCV curve [39], [27]. The low current is used to minimize kinetic contributions, reduce ohmic heat generation and electrode polarization [27]. It is assumed that the reactions happen at equilibrium state and that within a part of the SOC window, a pseudo OCV curve can be found [59]. Hysteresis can however still occur in the pseudo-OCV curves that are received from low rate cycling [60].

In order to determine parameters such as the capacities of the two electrodes, cycling tests with a low C-rate was conducted in a procedure that is influenced by a method presented in [39]. The low-rate tests include a full discharge followed by a full charge with a constant and low C-rate of C/30. This experiment makes it possible to determine the capacity of the full cell as well as the OCV characteristics. When operating in the SOC-window it is important to consider the different capacities of the electrodes. SOC is the ratio between the capacity and the maximum cell capacity [49]. A block diagram of the cycling test can be seen in Figure 14.
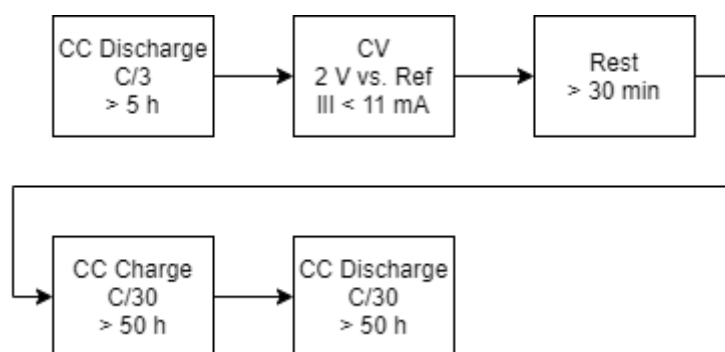

Figure 14, Low-rate cycling block diagram

Three cells were be tested with this procedure, some at C/30 and some at C/50 to make sure that the cell is in equilibrium.

3.2.2 Transport related parameters via GITT

GITT is a procedure useful to retrieve several kinds of parameters. The GITT procedure consists of a series of current pulses, each followed by a relaxation time where no current passes through the cell. The current is positive during charge and negative during discharge.

As mentioned in the *Background* several different methods can be applied to find the diffusion coefficient/diffusivity in the solid phase. The choice of method can also affect the values of the diffusion coefficient. For this thesis, only one method will be utilized. A series

of GITT tests can be used to find the solid diffusion coefficients of the electrodes. This is performed by a sequence of constant current discharge at low C-rate, followed by resting phases that brings the cells back to equilibrium. The experiment set up was influenced by the method used in [39] where test are done on a lithium titanate cell. In [39], the diffusion coefficient was extracted with a curve fitting procedure that assumed that the cell reaches equilibrium potential after a relaxation period. See Figure 15 for the desired appearance of the GITT pulse.
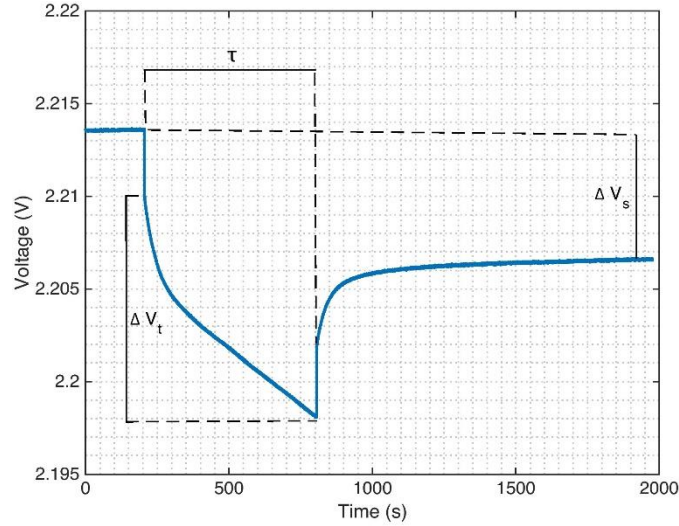
Figure 15, Shape of GITT pulse [39]

In Figure 15, the change in voltage ΔV_t in the pulse and ΔV_s which is the voltage in the equilibrium state after the pulse can be seen as well as τ which is the time of the pulse.

Equation 10 shows a general way to calculate the diffusion coefficient from GITT experiments for half cells. R_i is the internal resistance.

$$D_i = \frac{4}{\pi \tau} \left(\frac{R_i}{3}\right)^2 \left(\frac{\Delta V_s}{\Delta V_t}\right)^2 \tag{10}$$

By finding ΔV_t and ΔV_s for different parts of the SOC window, the diffusivity that is normalized with the particle radius can be found through a curve fitting procedure. Another more flexible approach to find values that are related to the diffusive phenomena is by fitting the relaxation region from the experimental data to simulated values. To compare the simulated and experimental data, these conditions need to be fulfilled:

1. The cell should be at rest in the start of the data set.
2. The current is the same in simulation and experiment.
3. The voltage should be the same in the start for the simulation and experiment.

The time needed for the cell to relax depends on the cell type [49]. While the relaxation time used in [39] was 15 minutes, a rest time of 2 hours was initially applied for the LFP/C cell. After finding that the cell did not reach equilibrium within the 2 hours, the relaxation time was extended to 4 hours. Due to the flat OCV curve of the LFP/C cell, a relative long time is required to get to equilibrium conditions. Because of this the cell is found not be relaxed even after 4 hours of rest so the latter approach is chosen.

The apparent diffusion coefficients and OCV characteristics can, as mentioned earlier, be found by performing GITT. By making GITT at different cell configurations like full cell, half-cell and three electrode set-up, the parameters can be compared [36] but only full cell test will be done in this work as is described in [39].

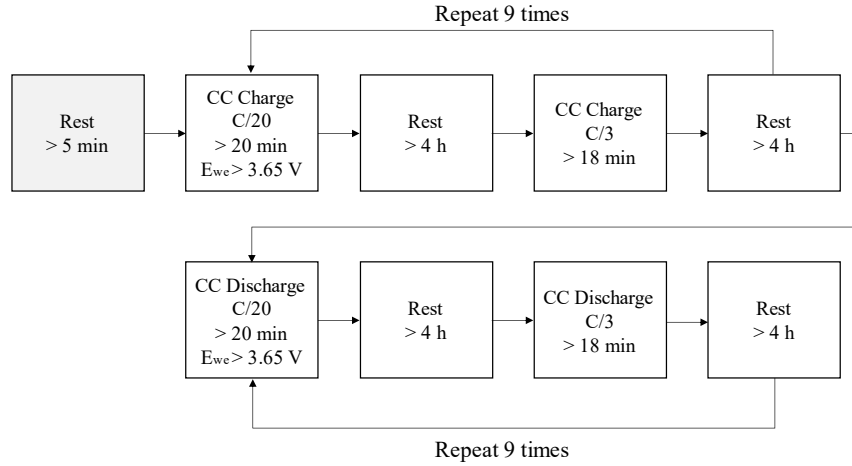The block diagram of the GITT test can be seen in Figure 16. The C/20 pulses are the GITT pulses while the C/3 pulses are used to move to another SOC level.

Figure 16, GITT block diagram

3.2.3 Kinetic parameters via pulse test

In [39] a pulse test consisting of a series of pulses with different C-rates were proposed as a method to find the reaction rate in the positive electrode, negative electrode and the resistance in the cell. Even though the reaction rates at each electrode nor the cell resistance are explicitly tuneable parameters in PyBaMM, the experimental setup does seem feasible to give the desired information. This was because the reaction rates in the electrode was related to the exchange current density at each electrode and the internal cell resistance was connected to the electrode conductivity which was tuneable in PyBaMM. The reaction rate was a factor that describes the exchange current density according to Equation 7. By adding a factor k_f to the equation, the effect on the exchange current density by changing the reaction rate can be found. The Equation 7 can be rewritten as Equation 11 for this purpose.

$$j_0 = k_f \cdot k \cdot \sqrt{c_e \cdot c_s \cdot (c_s^{max} - c_s)} \qquad (11)$$

With Equation 11, it is possible to find the k_f value that makes the simulation match the experimental data from the pulse test. The block diagram for the pulse test can be seen in Figure 17.
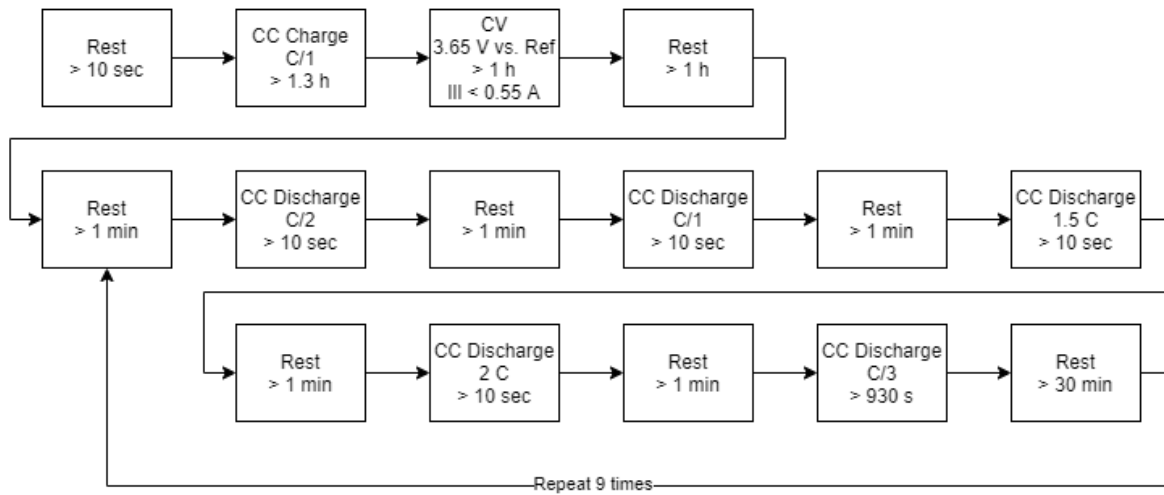
Figure 17, Pulse test block diagram

In [39] the parameter values can be related to the SOC and the current rates at the pulses. In this thesis only the first C/2 pulses will be used for fitting the values due to time restrictions.

3.3 Sensitivity analysis

For the GITT and pulse test a sensitivity analysis was performed to find how sensitive parameters are in relation to one another. The parameter values were changed by ± 10 % and the effect in different regions of the voltage profile will be investigated for each experiment.

Some parameters show linear characteristics in some parts, but the model is mostly non-linear. To care for the non-linearity, it is possible to grid the problem up and select several different points in the grid to see where the parameters are the most sensitive. This was done by selecting pulses in three different points of the grid: the beginning, centre and end. The sensitivity of the parameters D_+, D_-, r_+, r_-, k_{f+}, k_{f-}, σ_+ and σ_- will be found for GITT and pulse test simulations.

3.3.1 Sensitivity analysis for GITT

By shifting the cell from equilibrium with a small current during a long time, the ohmic and kinetic effect on the cell voltage want to be minimized while the effect from transport phenomena is maximized. The most relevant aspect to look at is the relaxation time and the region where the cell relaxes. In principle it would be possible to find the parameter values from the pulse region too. The reason why the pulse region was not included in the fit was because when the current is not zero, the deviation from equilibrium and the equilibrium itself is time-dependant which complicates the mathematical description taking place. When the current is zero, only the deviation from equilibrium is time-dependant. Therefore, the three C/20 GITT pulses were analysed based on their change in the dynamic relaxation region. A simulation of the GITT procedure during discharge can be seen in Figure 18. The pulses number 2, 6 and 9 were chosen to investigate to see the sensitivity in the beginning, middle and end of the SOC window.
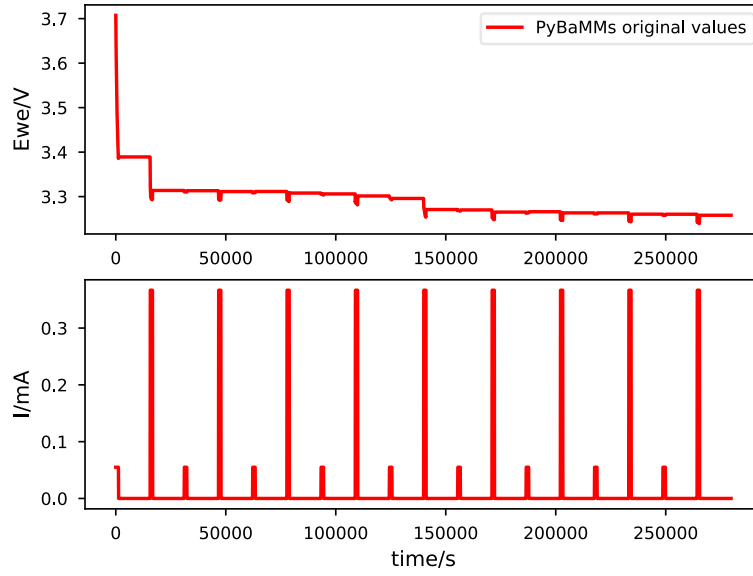
Figure 18, GITT simulation based on Prada 2013 parameter set

The period of interest was from the bottom of the pulse, where the relaxation starts, until the simulation have reach equilibrium at around half of the rest time until the next pulse.

A linear first order system can be described with this differential equation:

$$T\frac{dy}{dt} + y = Ku \qquad (12)$$

In Equation 12, K is the system´s steady state gain and the T is the time constant. The shape of the relaxation is very similar to the step answer of a first order linear time invariant system, see Figure 19. It was therefore assumed that the dynamic relaxation region acts like a first order linear time invariant system.
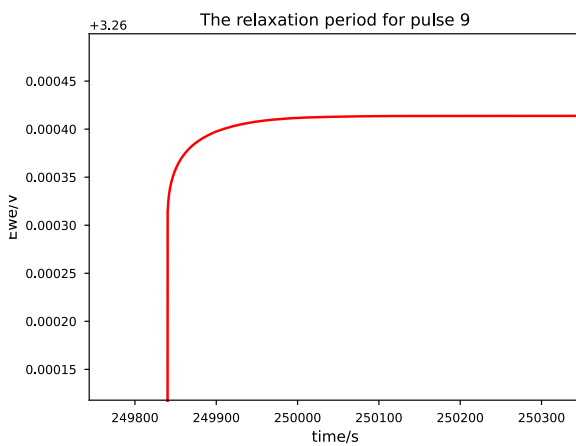
(a)
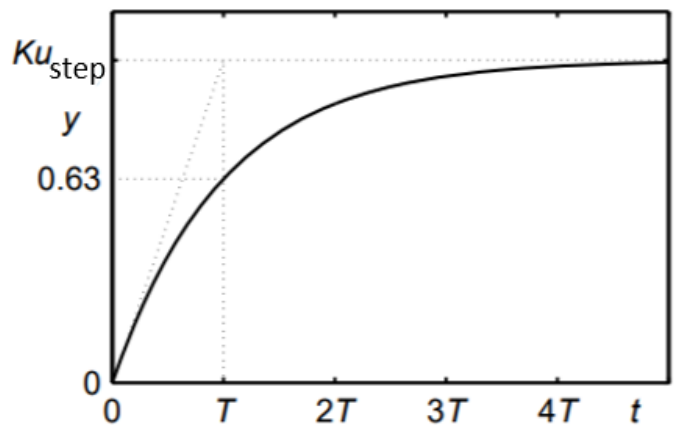
(b) [61]

Figure 19, (a) Zoom in on dynamic relaxation region (b) The step answer from a 1st order linear time invariance.

The dynamic relaxation resembles the response of a step answer which can be seen in Equation 13 [61].

$$y(t) = Ku_{step} \cdot \left(1 - e^{-t/\tau}\right) \tag{13}$$

By changing the parameters one by one, $\pm$ 10% from the original values, the changes of the disturbance can be seen for K and τ. By finding the K and τ values when no disturbance is done and then a measurement of the sensitivity could be calculated with Equation 14.a and 14.b.

$$Sensitivity_\tau = \frac{\left|\tau_{param,0.9} - \tau_{param,1.1}\right|}{\tau_{param,1}} \tag{14.a}$$

$$Sensitivity_K = \frac{\left|K_{param,0.9} - K_{param,1.1}\right|}{K_{param,1}} \tag{14.b}$$

3.3.2 Sensitivity analysis for Pulse test

During the pulse test, the pulse was conducted with a higher C-rate than in the GITT test and at a shorter time. The physical effect of this was that the overpotentials are mostly linked to activation and ohmic drop. The pulse duration of 10 seconds was on the limit of changing the cell concentration significantly. It is therefore assumed that concentration overpotentials are not affecting the pulses. The most interesting feature to capture for this test was the change in voltage during a pulse.

From the literature review (see *Background*), the reaction rates (related to the current density) and the internal resistance in the cell (related to the conductivity in the electrodes) would affect the depth of the voltage drop. Therefore, the region with the instantaneous voltage drops is the most interesting feature for the purpose of finding the targeted parameter values. In [39] the parameter values can be related to the SOC and the current rates at the pulses. For the sensitivity analysis, three pulses will be analysed for their effect on the voltage depth during a pulse.

Since the first pulse set is affected by relaxation, as seen in the steep appearance in Figure 20, the pulses set number 2, 6 and 10 were chosen to investigate to see the sensitivity in the beginning, middle and end of the SOC window. Only the first C/2 pulse in each pulse set is analysed.
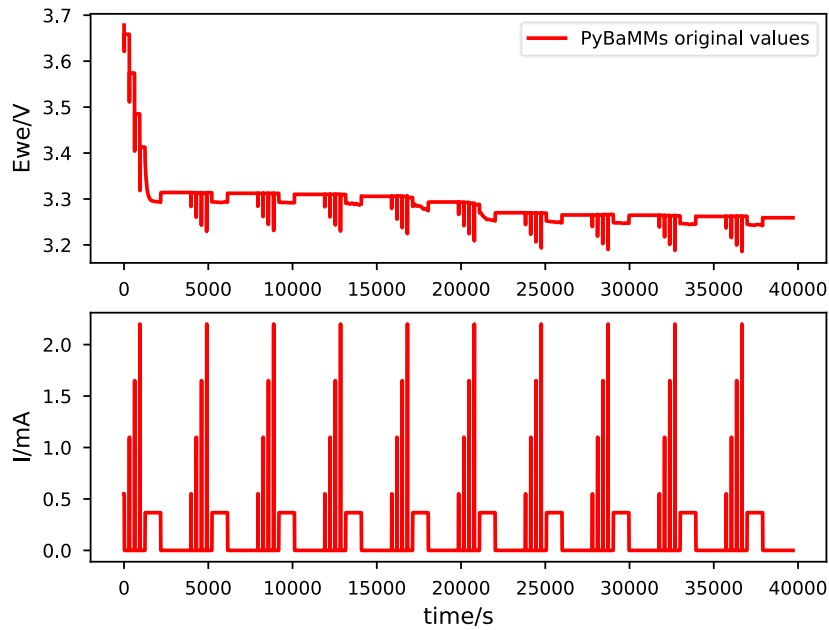
Figure 20, Pulse test simulation with Prada 2013 parameter set.

3.4 Parameter estimation method

In order to parametrize the SPM described in [37] that is available in PyBaMM, a series of experimental tests are conducted in a way described in [38] and [10] so that some parameters can be extracted from the data and through curve fitting. Three tests that describe different phenomena are conducted: low-rate cycling, GITT and pulse test. The low-rate cycling test explores the capacity phenomenon. The diffusion phenomenon is explored in the GITT test. In the pulse test, it is assumed that the diffusion phenomenon do not affect the results since the pulse is conducted under a short time, and the reaction rates can be explored. The settings for the experiments can be seen under the *Experiment descriptions*.

From the sensitivity analysis the parameter´s relative sensitivity is investigated for the GITT and pulse test. For each experiment, a few parameters have been selected since they are thought to be sensitive according to literature. For these chosen parameters that are taken from literature, a sensitivity analysis will be done on the simulations in PyBaMM to find out how sensitive the parameters are. The sensitivity analysis will be specific for the experiment and will be described in the section *Sensitivity analysis*.

For the parameters that are found to be sensitive for each experiment, the parameters will be tuned to make the PyBaMM simulation fit the experimental data as good as possible. The output will be three parametrizations: one to find the optimal parameter values for the cycling, GITT and pulse experiments, respectively. These experimental optimal parameters will then be part of the new parameter set that will make up the fully parametrized model. The parametrized model will be validated by comparing the simulations against data that aims to represent use of LFP/cells in BEV and mild-hybrid vehicles. This will also be compared to the default parameters found in PyBaMM. The parameters for GITT and Pulse test are found through a curve fitting procedure.

In order to get optimal values for the targeted parameters, Figure 13 presents how the parameter values will be found.

Figure 21 shows that the selected parameters are thermodynamic, transport and kinetic related. The parameter values found from the cell opening and the low-rate cycling will be used together with default values to find the parameter values of GITT and Pulse test that best match the experimental data.
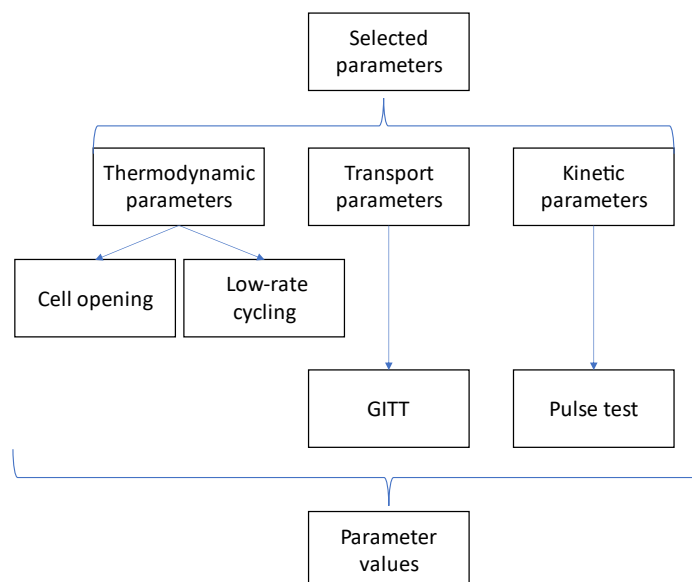

Figure 21, parametrization procedure*

*An alternative parametrization procedure can be found in Appendix D.

3.4.1 Cell opening

One cell is opened to measure some geometrical parameters. In Figure 22 (a) and (b) the measurement of the electrode and current collector can be seen. In order to get the geometrical parameters, a cell is opened. The cell is opened in a LABmasterPro Eco glove box from Mbraun by Matilda Klett Hudson at Scania material technology lab.

(a)   (b)

Figure 22 (a) and (b), measurement of geometrical parameters

The electrode heights and widths are measured with a mm spaced ruler seen in the lower part of Figure 22 b. The electrode thicknesses are measured with a micrometer that gives the result in micrometers on a digital display that can be seen in Figure 22 a. The electrodes in the cell are rolled upon itself, which is the structure of cylindrical cells, with the electrodes being a coated layer on top of the current collector as seen in the Figure 23.
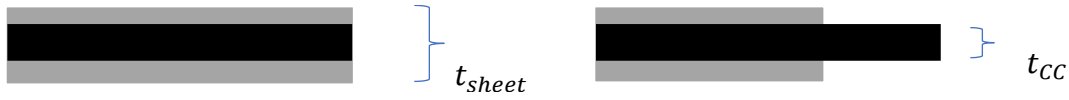

Figure 23, Measurement of thickness of electrode and current collector. The grey and black rectangles represent the electrode coating layers and the current collector.

In order to measure the thickness of the electrode coating layer the thickness of the whole sheet is measured, t_{sheet}. The layer of electrode coating is carefully scraped of using a scalpel. Some drops of dimethyl sulfoxide are used to loosen up the LFP coating layer while the graphite only needed the scalpel. The thickness of the current collectors is measured, t_{CC}. The thickness of the electrode coatings is calculated as in Equation 15.a and 15.b. The thickness of the electrodes is considered to include the coating on both sides of the current collector.

$$t_- = t_{sheet,-} - t_{CC,-} \tag{15.a}$$

$$t_+ = t_{sheet,+} - t_{CC,+} \tag{15.b}$$

The prefix of + and - symbolizes that the sheet and current collector is linked to the positive and negative electrode.

It was determined with eyesight that the electrode coating was removed from the current collector. There might still be coating present which will make the t_{CC} measurement prone to error. Therefore, several points on the scraped area are measured to get a mean value. The risk of damaging the current collector by creating holes in it with the scalpel is also a risk. When there is a visible hole, that area is excluded from the measuring points.

3.4.2 Low-rate cycling
The thermodynamic parameters from the cycling test are calculated in an order where the values found for one parameter is used to calculate the next one.

3.4.2.1 Cell capacity
The cell capacity at a certain c-rate can be calculated by Equation 16.

$$Q_{cell} = t_{discharge} \cdot \bar{I}_{discharge} \tag{16}$$

In Equation 16, Q_{cell} is the cell capacity discharged at a certain C-rate, $t_{discharge}$ is the time required to discharge the cell and $\bar{I}_{discharge}$ is the mean current during the discharge. The cell capacity is calculated from the low-rate cycling test. It is also possible to calculate the cell capacity during charging as well but only the discharging will be considered in the further calculations. Figure 24 shows the data from the full cycling test while Figure 25 shows the discharge part and the applied current.
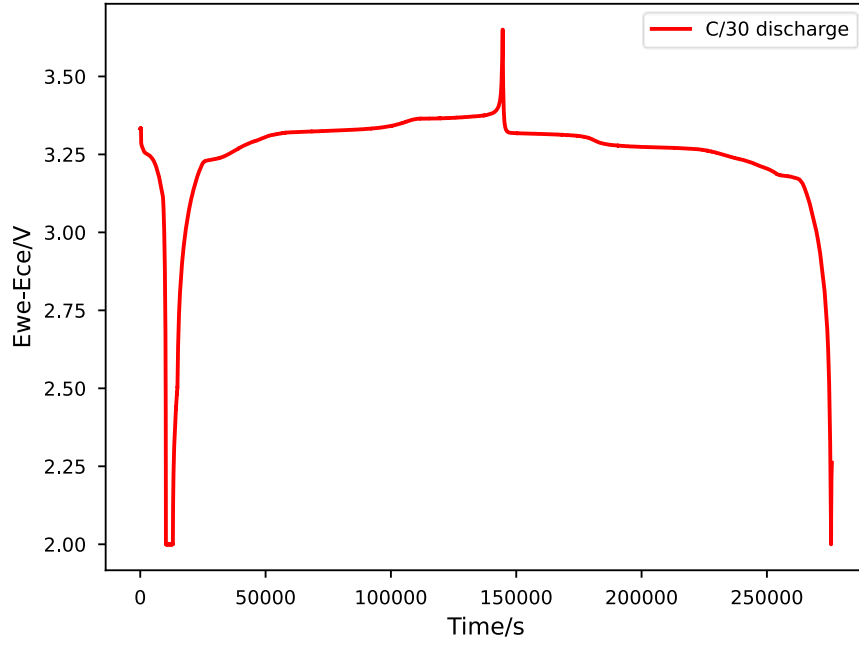
Figure 24, Low rate cycling (charge and discharge) cell D C/30
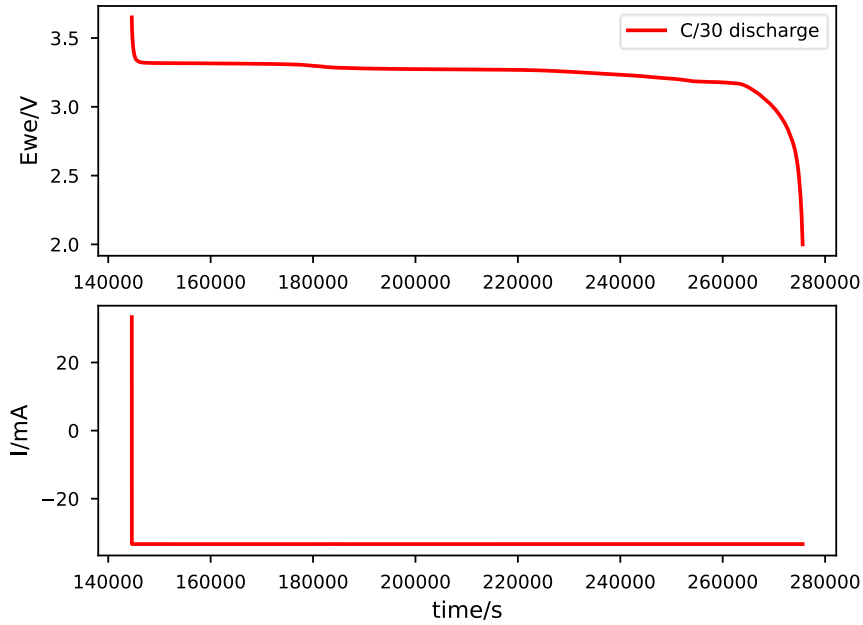

Figure 25, Low-rate cycling (discharge) cell D C/30

The nominal capacity, 1.1 Ah of the cell is obtained when the cell is discharged from fully charged at constant current and 1 C. In the low-rate cycling experiment the cell is discharged at C/30. The discharge capacity from cell D C/30 will be used for the following calculations.

The SOC is calculated according to Equation 17.

$$SOC = \frac{I \cdot t}{Q_{max}} \tag{17}$$

In Equation 17, I is the current, t is the time and Q_{max} is the maximum capacity of the cell. The equation is equivalent to finding the ratio between the capacity at a certain time and the maximum capacity.

3.4.2.2 OCV curve

In [39] it is stated that it is possible to determine the OCV curves as functions of the ion concentration in the electrode if the electrode material is known and literature is available. The OCV curves for each electrode are available as a parameter in Prada 2013, the LFP electrode as a function and the graphite as an array. Since these OCV curves are only for half cells, they need to be adapted to represent a full LFP/C cell. A wrapper function is used to make the LFP function to support iterables. Interpolation within the table data of the graphite is used to get values of the OCV. The SOC window is adapted and normalized between 0-1.

The OCV curves are related to the maximum and minimum concentrations of the individual electrodes. The values of these parameters will be fitted so that the OCV curve from the experimental data of the low-rate cycling matches the theoretical OCV functions of the electrode materials. The analytical OCV curve is set up according to Equation 18.

$$OCV_{fitted} = +OCP_+\left(z_{+,max}, z_{+,min}\right) - OCP_-\left(z_{-,max}, z_{-,min}\right) \qquad (18)$$

The difference between the electrodes OCV curves is found to describe the full cells OCV.

In order to calculate the *total available* capacity of the individual electrodes the stoichiometry at 0% and 100 % SOC in both electrodes need to be found through curve fitting. The capacities of the positive LFP and negative graphite electrode can be calculated as [39]:

$$Q_+ = \frac{Q_{cell}}{z_{+,max} - z_{+,min}} \qquad (18.a)$$

$$Q_- = \frac{Q_{cell}}{z_{-,max} - z_{-,min}} \qquad (18.b)$$

Where Q_+ and Q_- are the capacities of the positive and negative electrode, respectively. $z_{+,max}$ and $z_{+,min}$ are the stoichiometries at 100% and 0% SOC in the positive electrode. Alike goes for $z_{-,max}$ and $z_{-,min}$ but for the negative electrode. These stoichiometric values represent how much of the individual SOC window of each electrode that is used in the cell. The values will be in the range between 0 and 1, where 0 is linked to the lower stoichiometric value and 1 to the higher. If the entire SOC window of the electrode is used in the cell, the values will be 0 and 1.

This code was time-consuming to run. In order to reduce the number of times the code should run, bounds are found by manually changing the values until a reasonable good fit is achieved between the simulation and the experimental values. Smaller bounds around the manually found values are then used in the Scipy.optimize.curve_fit function in order to get an optimized fit.

In the fitting procedure, it is assumed to be of higher importance to get a good fit for the graphite bumps seen in Figure 26. To accomplish this, different regions of the SOC window was prioritized in the curve fitting procedure. The regions with the graphite bumps were prioritized higher while the other regions are weighted lower.

3.4.2.3 Active particles volume fractions in the electrodes

The active particles volume fractions in the electrodes can be calculated by rearranging equations 19.a and 19.b to equations 20.a and 20.b [41].

$$Q_- = A_+ \cdot t_- \cdot e_- \cdot C_{max,-} \cdot F \qquad (19.a)$$

$$Q_+ = A_+ \cdot t_+ \cdot e_+ \cdot C_{max,+} \cdot F \qquad (19.b)$$

$$e_- = \frac{Q_-}{A_+ \cdot t_- \cdot C_{max,-} \cdot F} \qquad (20.a)$$

$$e_+ = \frac{Q_+}{A_+ \cdot t_+ \cdot C_{max,+} \cdot F} \qquad (20.b)$$

In the Equations 19.a, 19.b, 20.a and 20.b A_p is the area of the positive electrode in m^2, t_- and t_+ are the thickness of the negative and positive electrode respectively in m, e_- and e_+ are the active particles volume fractions in the negative and positive electrode, respectively. $C_{max,-}$ and $C_{max,+}$ are the maximum solid phase concentration in the negative and positive electrode respectively and F is the Faraday constant of 96485 C/mol.

The values of the maximum solid phase concentration in the electrodes $C_{max,-}$ and $C_{max,+}$ are available in the Prada 2013 parameter set as $C_{max,-} = 33133 \ mol/m^3$ and $C_{max,+} = 22806 \ mol/m^3$. By inserting values in Equations 20.a and 20.b, the active particles volume fractions in the electrodes e_- and e_+ are calculated. Since these values are fractions, they will be expected to be between 0 and 1, where 0 means that there is no active material in the electrode and 1 means that all the electrode is made of active material.

4. RESULTS

4.1 Sensitivity analysis

The parameters relative sensitivity for the GITT and Pulse test can be found in the following headings.

4.1.1 Sensitivity analysis results for GITT

By following the parameter estimation method described in *Method,* the sensitivity values for pulse 2, 6 and 9 can be seen in Table 3 and 4.

Table 3. *The sensitivity in τ per pulse with a ± 10% change in parameter value*

Pulse	D_+	D_-	r_+	r_-	k_{f+}	k_{f-}	σ_+	σ_-
Nr 2	1.06e-2	1.52e-1	3.19e-2	3.03e-1	0.00	0.00	0.00	0.00
Nr 6	2.40e-05	1.86e-1	1.80e-3	3.72e-1	0.00	0.00	0.00	0.00
Nr 9	4.68e-3	1.68e-1	5.44e-3	3.33e-1	0.00	9.00e-1	0.00	0.00

Table 4. *The sensitivity in K per pulse with a ± 10% change in parameter value*

Pulse	D_+	D_-	r_+	r_-	k_{f+}	k_{f-}	σ_+	σ_-
Nr 2	-8.86e-3	-2.34e-1	-1.64e-2	-4.62e-1	0.00	0.00	0.00	0.00
Nr 6	2.47e-04	1.89e-1	3.00-4	3.74e-1	0.00	0.00	0.00	0.00
Nr 9	9.54e-5	2.15e-1	2.92e-4	4.25e-1	0.00	0.00	0.00	0.00

The values in the tables are calculated by taking the difference in τ or K, from the two runs

where a parameter is disturbed by ± 10% from its original value, divided by the τ or K when the parameters are not disturbed i.e., Equations 14.a and 14.b.

From the Tables 3 and 4 it seems like the electrode conductivities do not affect the relaxation time not the steady state gain since the σ_+ and σ_- are zero for all of the pulses. The negative reaction rate factor k_{f-} shows some sensitivity in τ for the ninth pulse but otherwise the reaction rates are also zero. The diffusivity and particle radiuses does seem to be sensitive for GITT, more for the negative electrode than the positive.

4.1.2 Sensitivity analysis results for Pulse test

Table 5. *The difference in lowest voltage point per pulse with a ± 10% change in parameter value*

Pulse	D_+	D_-	r_+	r_-	k_{f+}	k_{f-}	σ_+	σ_-
2	3.43e-7	2.65e-5	3.27e-5	5.37e-3	3.23e-5	5.36e-3	0	0
6	2.62e-7	1.59e-4	1.74e-5	5.06e-3	1.74e-5	4.78e-3	0	0
10	8.87e-9	3.36e-9	1.67e-5	4.66e-3	1.69e-5	4.70e-3	0	0
Mean	2.05e-7	6.18e-5	2.23e-5	5.03e-3	2.22e-5	4.95e-3	0	0

From the Table 5, it seems like the negative particle radius and the reaction rate have a large impact on the depth of the pulse because of the relatively large numbers. The change in conductivity does not seem to have any effect on the depth of the pulse since σ_+ and σ_- are zero for all the pulses.

4.1.3 Conclusion from sensitivity analysis

From the sensitivity analysis it can be seen that the diffusivities and particle radiuses are relatively sensitive for the relaxation period during GITT. The reaction rate is not relatively sensitive, in comparison to the other parameters, for GITT test but it is for the pulse test. For the pulse test, all parameters except for the conductivity are relatively sensitive. The negative reaction rate and the negative particle radius show the largest relative sensitivity.

The conductivities are not sensitive for either the GITT or the pulse test. The electrode conductivities are connected to the cell resistance and are therefore expected to be sensitive for the pulse test. The model does although not seem to capture this connection.

With this information it is determined that the parameters values for the D_+, D_-, r_+ and r_- are to be found through curve fitting to relaxation regions in the GITT experiment. The parameter value of k_{f-} will be found through curve fitting to the voltage drop in the pulse test. For the pulse test all the parameters k_{f+}, k_{f-}, σ_+ and σ_- will be seen individually to see how fitting these values change the model output. The r_- is relatively sensitive for both the GITT and the pulse test.

4.2 Cell opening

All the measured thicknesses of the current collectors can be found in the Table 6.

Table 6. T*hickness of current collectors*

Measurement	$t_{CC,-}$ Aluminium current collector [μm]	$t_{CC,+}$ Cupper current collector [μm]
a	15	20
b	16	18
c	18	20
Mean	16.33	19.33

The thickness of the sheets are $t_{sheet,-} = 82 \, \mu m$ and $t_{sheet,+} = 119$ μm. Inserting the values into Equation 15.a and 15.b gives the following.

$$t_n = t_{sheet,n} - t_{CC,n} = 82 - 16.33 = 65.67 \, \mu m$$

$$t_p = t_{sheet,p} - t_{CC,p} = 119 - 19.33 = 99.67 \, \mu m$$

The measured parameters from the cell opening can be seen below in Table 7.

Table 7. *Measured geometrical parameters*

	LFP electrode	C electrode	Separator	Al current collector	Cu current collector
Height [m]	5.7e-2	5.9e-2	-	-	-
Width [m]	0.895	0.937	-	-	-
Thickness [m]	9.97e-5	6.56e-5	1.6e-5	1.63e-5	1.93e-5

A summary of some measured parameters and their relative value in the Prada 2013 parameter set can be seen in the Table 8.

Table 8. *Measured geometrical parameters compared to Prada 2013*

Measured parameters [m]		Prada 2013 parameter values [m]	
Negative electrode thickness	6.57e-5	Negative electrode thickness	3.6e-5
Positive electrode thickness	9.97e-5	Positive electrode thickness	8.1e-5
Positive electrode height	0.057	Electrode height	0.0649
Negative electrode height	0.059	-	-
Positive electrode width	0.895	Electrode width	1.78
Negative electrode width	0.937	-	-

The positive LFP electrode has similar measured thickness as the one available in PyBaMM while the measured negative electrode thickness is almost double in comparison. This difference in cell dimensions is expected since this work uses another cell, but with same structure and chemistry, as the one in Prada 2013.

In PyBaMM, there is only one electrode dimension available as "Electrode height" and "Electrode width". The LFP electrode has smaller dimensions than the graphite electrode and will limit the number of Li-ions available for charge transfer. Therefor the PyBaMM electrode dimensions were matched with the positive LFP, i. e. the smallest, electrode. The electrode

areas are calculated below by multiplying the height and width since they are rectangular shaped. The areas were $5.53 * 10^{-2} \ m^2$ and $5.10 * 10^{-2} \ m^2$ for the negative and positive electrode, respectively.

4.3 Low-rate cycling

The results of the different calculations related to the low-rate cycling experiments can be found in the following sections.

4.3.1 Cell capacity

The cell capacity can be found for the discharging part of the cycling test but also during the charging.

Table 9. *Discharge, charge and mean capacity for different cell test*

Test cell	$Q_{Discharge}$ [Ah]	Q_{Charge} [Ah]
Cell D C/30	1.21	1.20
Cell C C/30	1.21	1.20
Cell D C/50	1.24	1.25

From Table 9, a small difference between the charge and discharge capacities can be seen. It is expected that the charge capacity would be a little larger than the discharge capacity due to irreversible side reactions. An error in the cycle test could be that the cells are not fully relaxed before the pulse starts. This effect could be avoided by adding a constant voltage step at the fully discharge state and the fully charge state. The effect from this is mostly visible in the charge step.

4.3.2 OCV curve

The best values found manually for the parameters $z_{-,min}$, $z_{-,max}$, $z_{+,min}$ and $z_{+,max}$ as well as the bounds used for the curve fit optimize procedure can be seen in Table 10.

Table 10. *Values from manual fit and the bounds for the optimizer.*

Parameter	Best found values manually	Bounds used for optimizer
$z_{-,min}$	0.1571	$0.07 < z_{-,min} < 0.2$
$z_{-,max}$	0.8768	$0.78 < z_{-,max} < 0.9$
$z_{+,min}$	0.005068	$0 \quad < z_{+,min} < 0.01$
$z_{+,max}$	0.9988	$0.98 < z_{+,max} < 1$

The simulations with the manually found values, the optimizers found values and the experimental data can be seen in Figure 26.
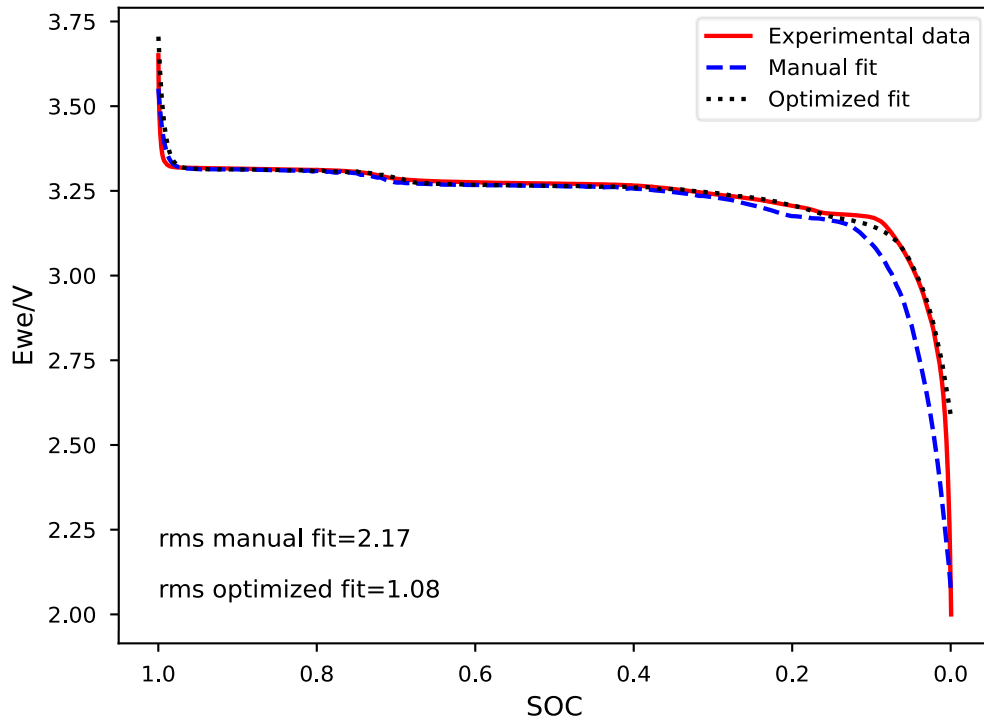
Figure 26, OCV curve fit

From Figure 26, the values found with the optimized fit seen as the black dotted curve follows the red curve that is the experimental data significantly better in the region SOC > 0.7 than the manually found values shown as the lined blue curve. The optimized values do however have a higher voltage at SOC=1 in comparison to the experimental data and manually found values. The root-mean-square error (RMS) for cell D C/30 is about 1.08 for the optimizer fit and 2.17 for the manually fitted curve. This is a quantitative sign that the found values are better at fitting the experimental data than the manually found values. This can also be seen qualitatively from Figure 26.

The stoichiometric values at 0 and 100% SOC for both the electrodes can be seen in Table 11.

Table 11. *Stoichiometry at SOC levels in electrodes*

Test cell	$z_{-,min}$	$z_{-,max}$	$z_{+,min}$	$z_{+,max}$
Cell D C/30	0.1270	0.8141	0.001653	0.98
Cell C C/30	0.1280	0.8158	0.001552	0.98
Cell A C/30	0.1270	0.8251	0.002288	0.98
STDEV	0.000452	0.004833	0.000326	0

The $z_{-,min}$ and $z_{-,max}$ values represent the range of the negative graphite electrodes SOC window that is use in the cell. The range of $0.12 - 0.81$ ($12 - 81\%$) is assumed to be reasonable since it is not less than 0 or above 1. The $z_{+,min}$ and $z_{+,max}$ values represent the range for the positive LFP electrode. The range $0.001 - 0.98$ ($0.1 - 98\%$) is very large. This would mean that most of the LFP electrodes SOC window is used in the cell.

4.3.3 Total available electrode capacity

With the cell capacity and the stoichiometry in both electrodes at 0 and 100% SOC in the cell are known, the capacities of the individual electrodes can be calculated with Equation 18.a and 18.b.

$$Q_+ = \frac{Q_{cell}}{z_{+,max} - z_{+,min}} = \frac{1.212}{0.98 - 0.00165} = 1.239$$

$$Q_- = \frac{Q_{cell}}{z_{-,max} - z_{-,min}} = \frac{1.212}{0.814 - 0.127} = 1.764$$

The *total available* capacities of the individual electrodes are about 1.240 Ah for the positive one and 1.764 Ah for the negative one.

4.3.4 Active particle volume fractions

The factors are calculated with Equations 20.a and 20.b.

$$e_- = \frac{Q_-}{A_+ \cdot t_- \cdot C_{max,-} \cdot F} = \frac{1.76}{0.0510 \cdot 6.57e{-}5 \cdot 33133 \cdot 96485 \cdot 3600} = 0.593$$

$$e_+ = \frac{Q_+}{A_+ \cdot t_+ \cdot C_{max,+} \cdot F} = \frac{1.24}{0.0510 \cdot 9.97e{-}5 \cdot 22806 \cdot 96485 \cdot 3600} = 0.398$$

A factor of 3600 is added in the denominator to change the capacity from Ah to As. The factors of e_- and e_+ are unitless.

The values of e_- and e_+ are between 0 and 1 and are therefore not unrealistic. A summary and comparison of the calculated parameters compared to the once in PyBaMM can be seen in Table 12.

Table 12. *Comparison between calculated parameter values and the values available in Prada 2013*

Parameter	Calculated	Prada 2013
e_- [-]	0.593	0.75
e_+ [-]	0.398	0.28485556

4.4 GITT

In the following headings, results and analysis of the parameter estimation for the GITT experiment can be found.

4.4.1 Parameter estimation from GITT

From the sensitivity analysis (see *Sensitivity analysis*) it is found that the parameters D_+, D_-, r_+ and r_- is sensitive during the relaxation region after the GITT pulses. It is also determined that the parameter values for these parameters were found by using experimental data from the GITT experiment. The values were found through fitting the simulation curve to the experimental data from the GITT experiment. The GITT experiment during discharge of cell A can be seen in Figure 27.
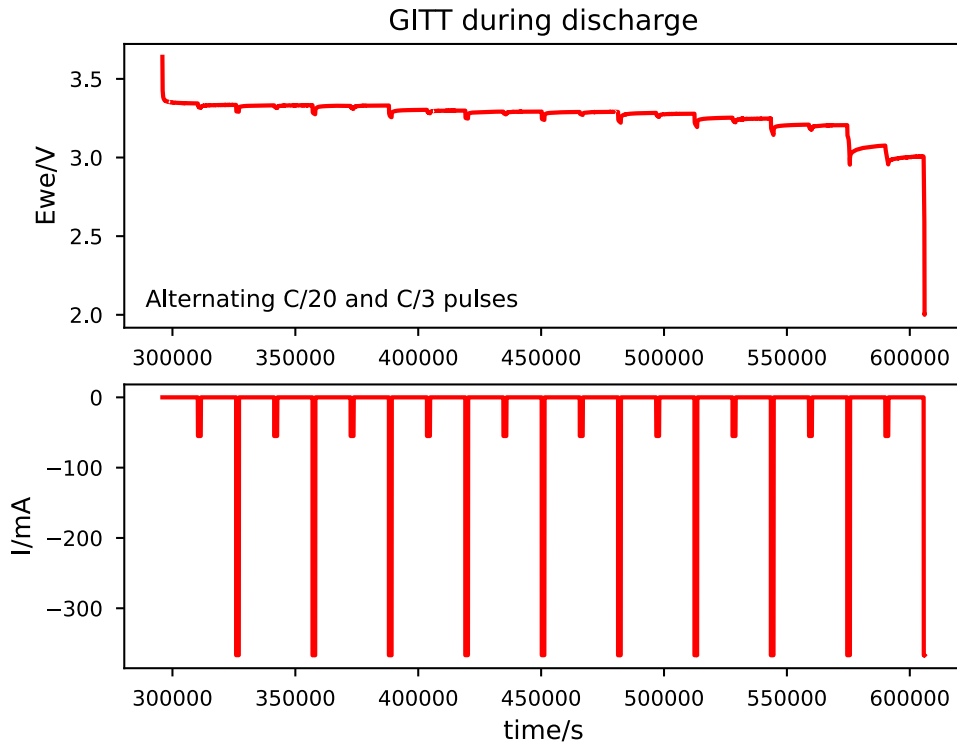
Figure 27, GITT during discharge

In Figure 27, ten C/20 pulses (smaller voltage drop) and ten C/3 pulses (larger voltage drop) can be seen in an alternating manner from the fully charged cell until the 2.0 V cut-off voltage is triggered. The smaller C/20 pulses are the GITT pulses and the larger C/3 pulses moves the cell into another SOC. In order to find optimal values for the parameters D_+, D_-, R_+ and R_- each C/20 pulse is individually fitted to the experimental data using scipy.optimix.curve_fit. The bounds for the parameters can be seen in Table 13.

Table 13. *Bounds for curve fitting procedure of GITT.*

Parameter	Unit	Prada 2013 value	Lower bound	Upper bound
D_+	m^2/s	5.9e-18	5.9e-19	5.9e-17
D_-	m^2/s	3.3e-14	3.3e-15*	3.3e-13*
R_+	m	1e-08	1e-09	1e-07
R_-	m	5.86e-6	5.86e-07	5.86e-05

The bounds of the negative particle radius will be limited to 1e-6 – 1e-5 m in a second iteration.

A selection of the plots from the curve fitting can be seen in Figure 28.
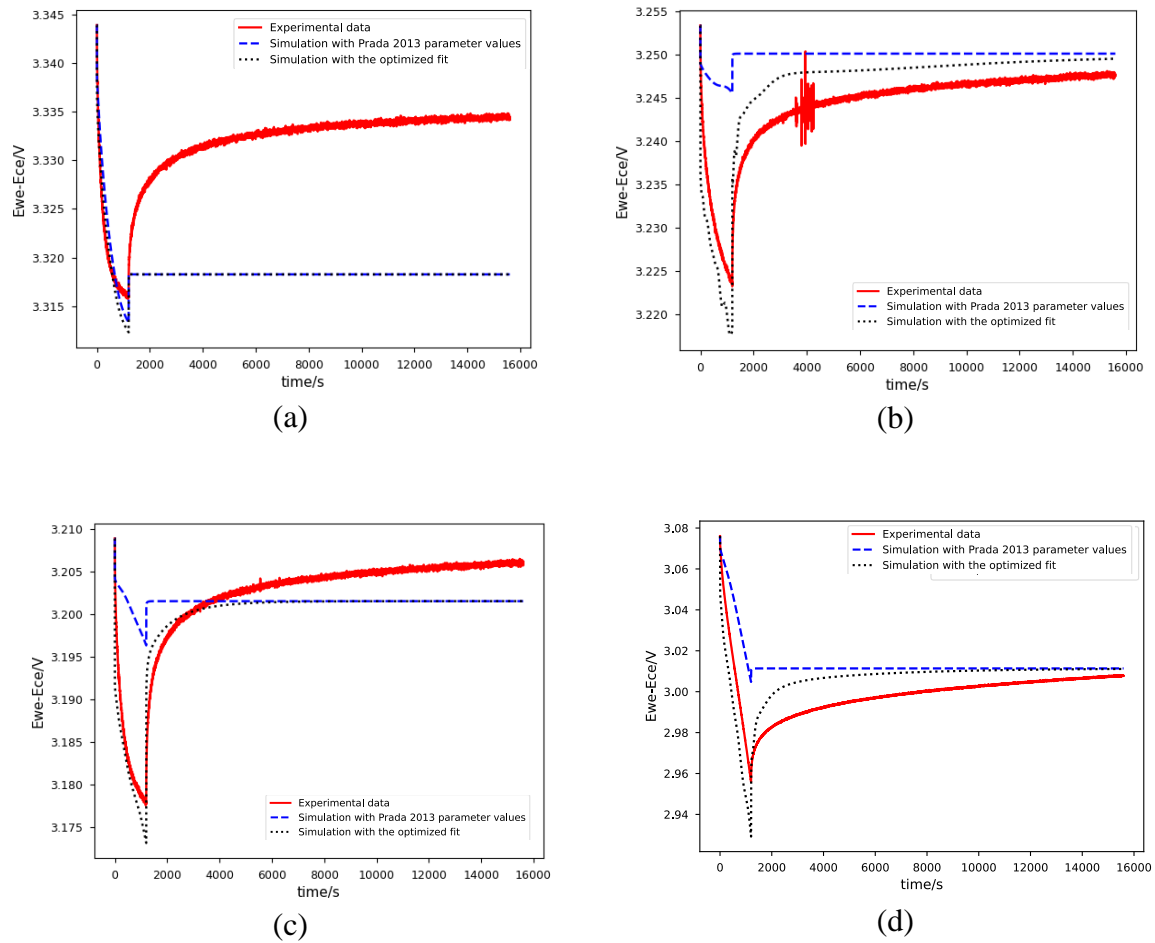
Figure 28, A selection of the fitted curves for four pulses. (a) shows the first C/20 pulse, (b) shows the eighth pulse, (c) shows the ninth pulse and (d) shows the tenth pulse. The fitted curves of the rest of the pulses can be found in Appendix C.

As explained in *Sensitivity analysis* for GITT, the region when the curve relaxes back to equilibrium after the pulse is the most interesting feature to fit for GITT. From Figure 29, (a) shows a fit that does not capture the relaxation relatively well. Both the simulation with the Prada 2013 and the optimized values has a sharp appearance in the region where the experimental data shows the relaxation. With these values it seems like the simulated response relaxes and reaches equilibrium conditions much faster relative to the experimental data shows. For most of the pulses (nr 1-7) the simulation does not capture the gradual relaxation in a realistic way. See the fit for all the pulses in Appendix C. For the eighth, ninth and tenth pulses the fit can be seen in Figure 29 (b), (c) and (d). The optimized values found for these pulses give a better fit than the Prada 2013 values and yield the gradual relaxation from the experimental data in a more realistic way than the other pulses. Figure 29 (b) shows some disturbance in the experimental data, which is also included in the curve optimization procedure. An observation from Figure 29 is that the simulated curves have higher voltages than the experimental data, (b) and (d), and sometimes lower, (a) and (c). The values found through the fitting procedure for the selected pulses as well as the values available in the Prada 2013 parameter set can be seen in Table 14.

Table 14. *Parameter values found via curve fitting for each GITT pulse*

Origin of values	$D_+ \left[m^2/_s \right]$	$D_- \left[m^2/_s \right]$	$R_+ [m]$	$R_- [m]$
Bounds	5.9e-19 − 5.9e-17	3.3e-15 – 3.3e-13	1e-9 – 1e-7	5.86e-7 – 5.86e-5
Prada 2013	5.9e-18	3.3e-14	1e-8	5.86e-6
Pulse 1	2.895e-18	3.317e-14	4.650e-8	6.608e-06
Pulse 8	5.900e-17	3.300e-15	1.000e-9	2.390e-05
Pulse 9	5.219e-17	1.716e-14	4.988e-8	2.195e-05
Pulse 10	5.770e-17	1.104e-14	1.016e-9	3.102e-05
Mean*	2.77e-17	4.95e-14	3.37e-08	1.66e-05
STDEV*	2.62e-17	7.12959e-14	2.97e-08	8.84e-06

* The mean value and the standard deviation are based on the values found for all the fitted pulses. See the fitted values for all the pulses in Appendix C.

From Table 14, it shows that the pulses nr 8, 9 and 10 (whose parameter values made the simulation match the gradual relaxation of the experimental data) goes towards the upper boundary for D_+, especially for pulse nr 8. The electrochemical implication of this would be that the diffusion goes faster at the positive electrode than the Prada 2013 values would give. D_- lays within the middle of the boundary except for pulse nr 8 who matches the lower bound. This would mean that the diffusion is slower at the negative electrode. The diffusivity in the negative electrode is however still larger than in the positive electrode. The R_+ goes to the lower boundary value while the R_- goes to the higher value. The particle radiuses are affected by the production process.

To see how the parameter values found for pulse 8, 9 and 10 would impact the simulation for the full discharge, Figure 29 is made. All ten pulses are not able to simulate because the lower cut-of voltage is triggered by the ninth C/3 pulse.
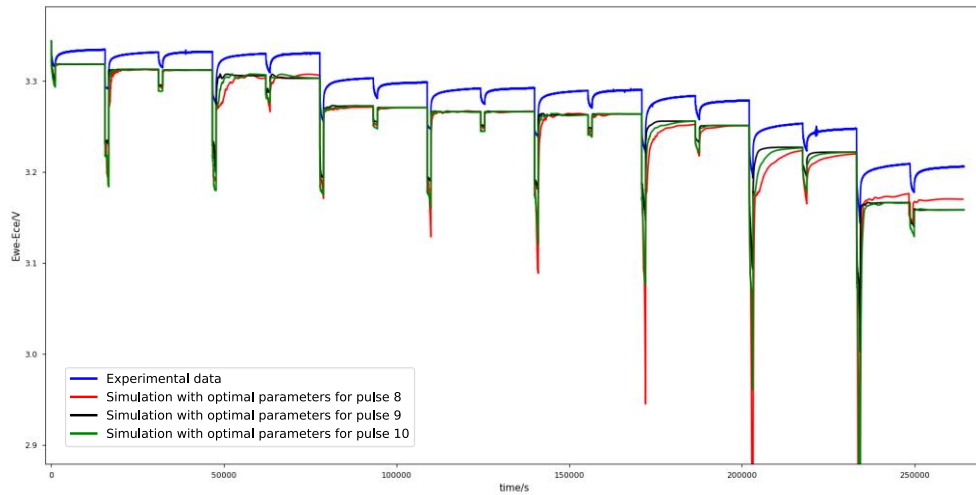
Figure 29, GITT experiment during discharge. The blue curve represents the experimental data, the red is the simulation with optimal parameters for pulse 8, the black is for pulse 9 and green is for pulse 10.

From Figure 29, it seems like the simulated relaxation is less visible in the region around 75000 - 125000 seconds while the slopes are more visible in the other pulses. The parameter values are found by fitting the simulation to the C/20 pulses. Although, since the GITT

experiment has both C/20 and C/3 pulses Figure 30 is created by zooming in on two different pulses to see the impact on fit that the C-rate gives.

(a)   (b)
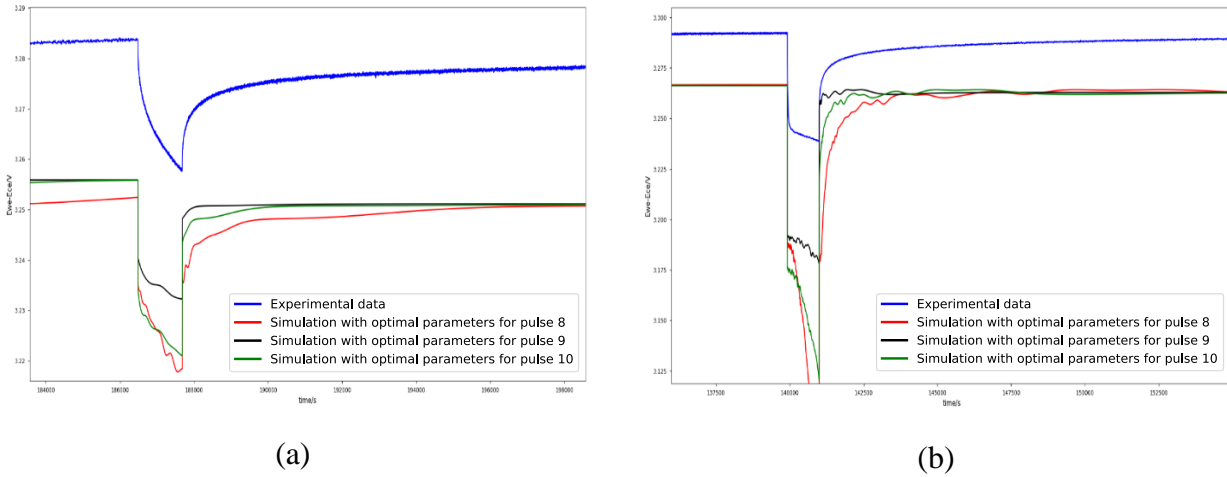
Figure 30, Zoom in on Figure 29 on (a) a C/20 pulse, and (b) a C/3 pulse.

From Figure 30 it seems like the simulated values from pulse 8 and 10 matches the gradual relaxation of the experimental data the best. For the C/20 pulse it looks like the values from pulse 8 has the best match. From Figure 30 the simulations do not have as smooth appearance as the experimental data. This is likely due to the numerical calculations that takes place in the simulation where the solver fits a polynomial to the experimental data. The parameters that best capture the relaxation time can be seen in the Table 15 below.

Table 15. *The parameter values of the best fitted pulse (8) compared to Prada 2013 parameter set*

Parameter	Unit	Value	Prada 2013
D_+	m^2/s	5.900e-17	3.3*10^-14
D_-	m^2/s	3.300e-15	3.3*10^-14
r_+	m	1.000e-09	1.00*10^-8
r_-	m	2.390e-05	5.86*10^-6

Another run when the bound of the relatively sensitive parameter r_- is limited in a tighter manner, 1e-6 < r_- < 1e-5, can be found in Appendix D.

4.4.2 Experiment analysis for GITT

From Figure 29 and 30, a voltage gap can be seen after each pulse where the experimental data often has a higher voltage than the simulated curves. To visualize this better, the Figure 31 below shows the experimental data and the simulation with optimized parameters from pulse 9 for the discharge involving nine C/20 pulses and eight C/3 pulses.
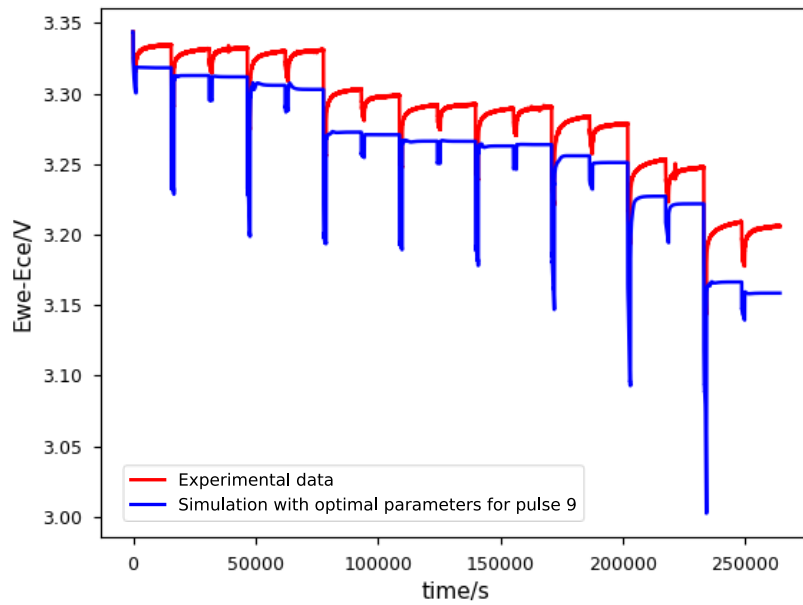
Figure 31, the voltage offset between the experimental data and the simulated data for the GITT experiment.

The simulated curve operates as a lower voltage than the experimental data. The size of the voltage gap differs in size throughout the experiment. This difference in voltage is not closely related to the concentration overpotential but once again a result of the OCV curve found from the low-rate cycling experiment. With correct OCV curves, the simulated pulses would relax to the same place as the experimental data. It can also depend on that the cell is not fully relaxed, at equilibrium, in the beginning of the GITT pulse.

In the GITT experiment, pulses with C/20 and C/3 are alternated. The C/3 pulses are used to shorten the time for the experiment but also to get data from different SOC levels by "fast forwarding" to the next level. Four hours of rest is used between the C/3 and C/20 pulses to give the cell time to go back to equilibrium conditions. The new pulse should start at relaxation, which might not always be correct as can be seen in the experimental data in Figure 32.
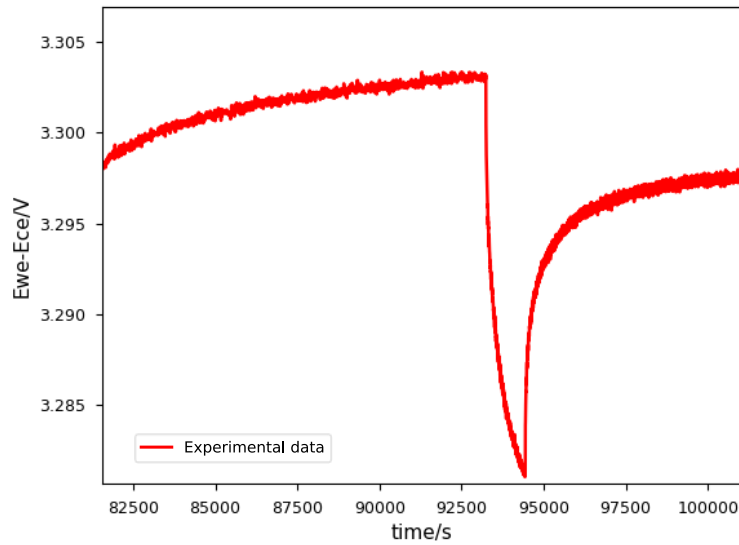
Figure 32, Unfinished relaxation before GITT pulse.

In Figure 32 the voltage is not completely flat but that there is a slope in the mV range taking place before the next pulse starts. This could mean that there is still relaxation taking place from the last pulse that influence the appearance of the next one.

When the cell is at equilibrium, the voltage points should be present on the OCV-curve. The voltage gap when the simulation is getting close equilibrium conditions, seen in Figure 31, is although still relatively large in the order of around 20-30 mV. This could be the result of the OCV curve fit that might have resulted in errors in the stoichiometric ratios for the electrodes, individual electrode capacity etc.

4.5 Pulse test
In the following headings, results and analysis of the parameter estimation for the Pulse test can be found.

4.5.1 Parameter estimation from Pulse test
From the sensitivity analysis (see *Sensitivity analysis*) it is determined that the values of the k_{f-} is going to be found from the pulse test. The bounds are $0.5 < k_{f-} < 5$. The pulse test experiment during discharge can be seen in Figure 33.
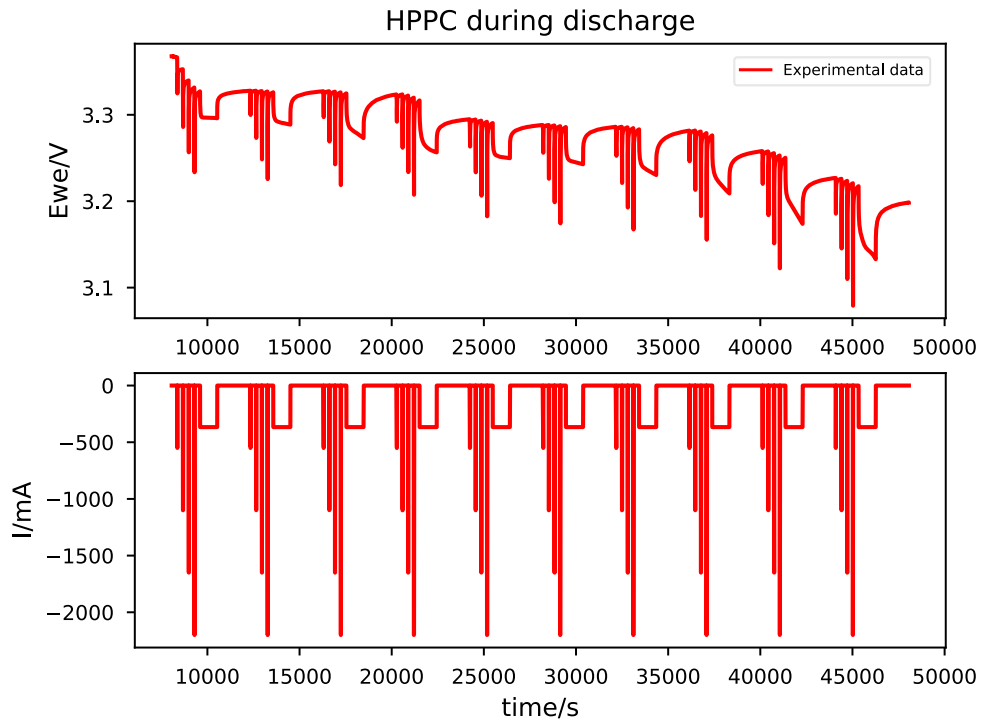
Figure 33, Pulse test during discharge

In Figure 33, there are ten pulse trains consisting of four ten-seconds pulses in each with a five-minute rest in between (see *Experiment methods* for more experimental details). It is decided that only the C/2 pulse in each pulse train was utilized for fitting the values due to time restrictions. A selection of the plots from the curve fitting can be seen in Figure 34.

(a)   (b)

(c)	(d)
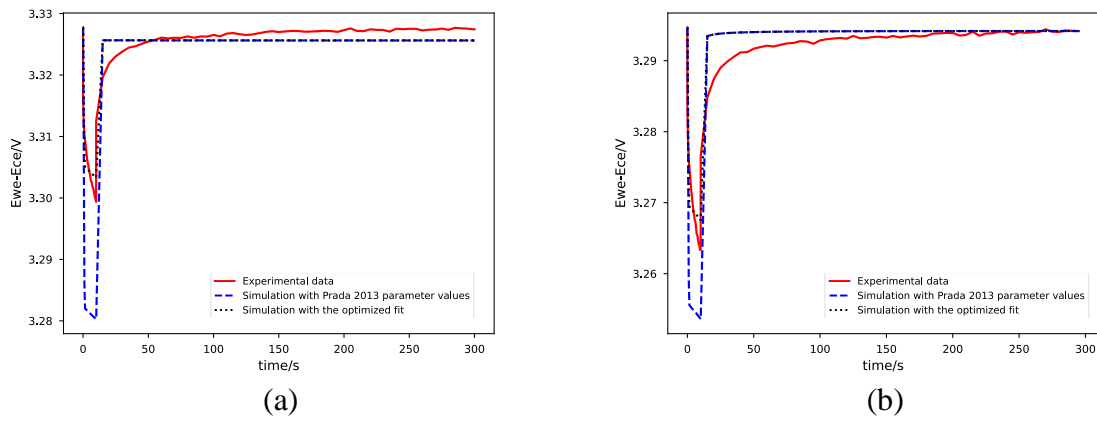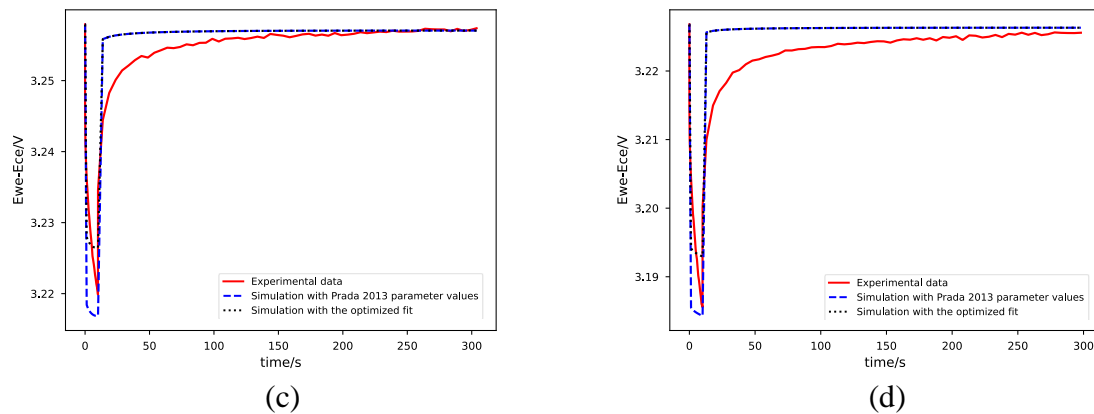
Figure 34, the plots when only k$_{f\text{-}}$ is fitted. (a) pulse 2, (b) pulse 5, (c) pulse 8 and (d) pulse 9.

As explained in *Sensitivity analysis* for the pulse test, the depth of the pulse is the most interesting feature to fit. From Figure 34, (a) shows a plot where the fitted k$_{f\text{-}}$ value give a relatively large improvement compared to the simulation with the default value. The simulation with the default value has a larger voltage drop compared to the experimental data. By comparing (a), (b), (c) and (d) it appears that the simulation with the default k$_{f\text{-}}$ value fit the experimental data better at lower SOC levels (higher pulse number). While the simulation using the default value fits the experimental data better for pulse 8 and 9, the simulation with the fitted k$_{f\text{-}}$ is lower than 0.01 V off compared to the experimental data in all the plots. By favouring the simulation that had a better match to the experimental data than the simulation with the default value, the parameter values of pulse 2 is considered the most suitable fit. It could be argued that the default value could also be of interest for lower SOC levels. The values found through the fitting procedure for the selected pulses as well as the values available in the Prada 2013 parameter set can be seen in Table 16.

Table 16. *The fitted parameter values from the simulation*

Origin of values	k_{f-} [-]
Bounds	$0.5 - 5$
Prada 2012	1
Opt. Train 2	2.26116222
Opt. Train 5	1.65668429
Opt. Train 8	1.38499424
Opt. Train 9	1.31931518
Mean*	1.746649983
SDEV*	0.330851661

* The mean value and the standard deviation are based on the values found for all the fitted pulses. See the fitted values for all the pulses in Appendix C.

From Table 16, it shows that the values of k_{f-} is in the lower part of the bound. As the pulses are found in the lower part of the SOC window, the k_{f-} value becomes closer to the default value.

4.5.2 Experiment analysis for Pulse test

In order to follow up on the sensitivity analysis for the pulse test, the parameters k_{f-}, k_{f+}, σ_- and σ_+ are fitted one-by-one to see the effect on the simulation. The bounds used can be seen in Table 17.

Table 17. *Bounds for parameters used in the experimental analysis for the Pulse test.*

Parameter	Unit	Prada 2013 value	Lower bound	Upper bound
k_{f-}	-	1	0.5	5
k_{f+}	-	1	0.5	5
σ_-	S/m	215	190	250
σ_+	S/m	0.338	0	0.5

Figure 35 show the fitted simulations together.
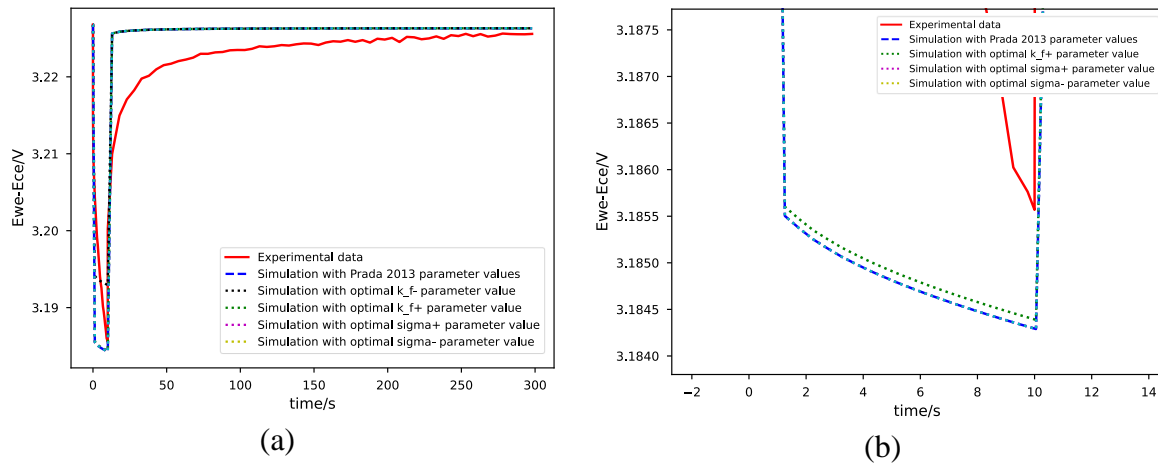
Figure 35. Fitting one parameter at the time. (a) shows a pulse with all simulations. (b) show a zoom in on the lower part of the pulse in (a).

Figure 35 confirms the sensitivity analysis because the simulations where the optimal values for the electrode conductivities are placed precisely on top of the simulation with the default values from the Prada 2013 parameter set. The simulation with the optimal value for the factor k_{f+} shows a small change compared to the default values, but not in the same range as the k_{f-} does.

4.6 Validation

The fitted values of the parameters can be seen in Table 18.

Table 18. *Estimated parameter values found from parametrization*

Parameter	Unit	New value	Prada 2013 value
Negative electrode thickness	m	6.57e-5	3.6e-5
Positive electrode thickness	m	9.970e-5	8.1e-5
Electrode height	m	5.7e-2	0.0649
Electrode width	m	0.895	1.78
Negative current collector thickness	m	1.633e-5	1e-5
Positive current collector thickness	m	1.933e-5	1.9e-5
Separator thickness	m	1.6e-5	1.8e-5
Positive electrode active material volume fraction	-	0.399	0.285
Negative electrode active material volume fraction	-	0.593	0.75
Positive electrode diffusivity	m^2/s	5.9e-17	5.9e-18
Negative electrode diffusivity	m^2/s	3.3e-15	3.3e-14
Positive particle radius	m	1e-09	1e-8
Negative particle radius	m	2.39e-05	5.86e-6
Reaction rate factor k_{f-}	-	1.747	1
Reaction rate factor k_{f+}	-	Unchanged	1
Positive electrode conductivity	S/m	Unchanged	0.33795074
Negative electrode conductivity	S/m	Unchanged	215.0

The parameter values were used in two different scenarios to validate in a qualitative manner to evaluate the simulation matches experimental data. For both validation scenarios, the cell capacity will have a large impact on how well the simulation matches the experimental data.

4.6.1 BEV application

The found parameter values were used to simulate a possible BEV application and is then compared to experimental data. The block diagram for the BEV application can be found in Figure 36.
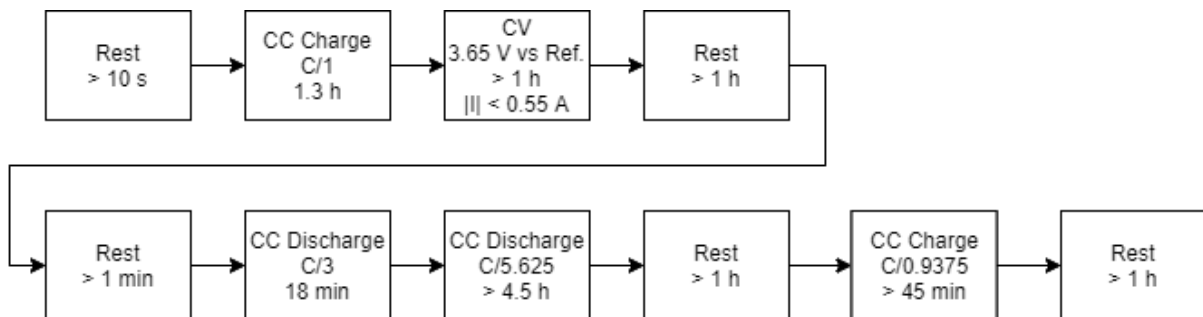
Figure 36, Potential BEV application block diagram

When trying to use the found value for the negative particle radius, the CasADI solver in PyBaMM fails due to exceed interpolation bounds. A trial is done by using the parameter values from the ninth and tenth GITT pulse, where the relaxation time is also reasonable, but

the same error message appeared. To be able to plot the simulation, the default value for the negative particle size is used instead of the fitted value.

The experimental data of the BEV application is compared with two simulations. One where only the thermodynamic values are changed from the default values and another where all the found parameter values are used (except for the negative particle radius where the default is used). See Figure 37 for the plots.

(a)

(b)

(c)
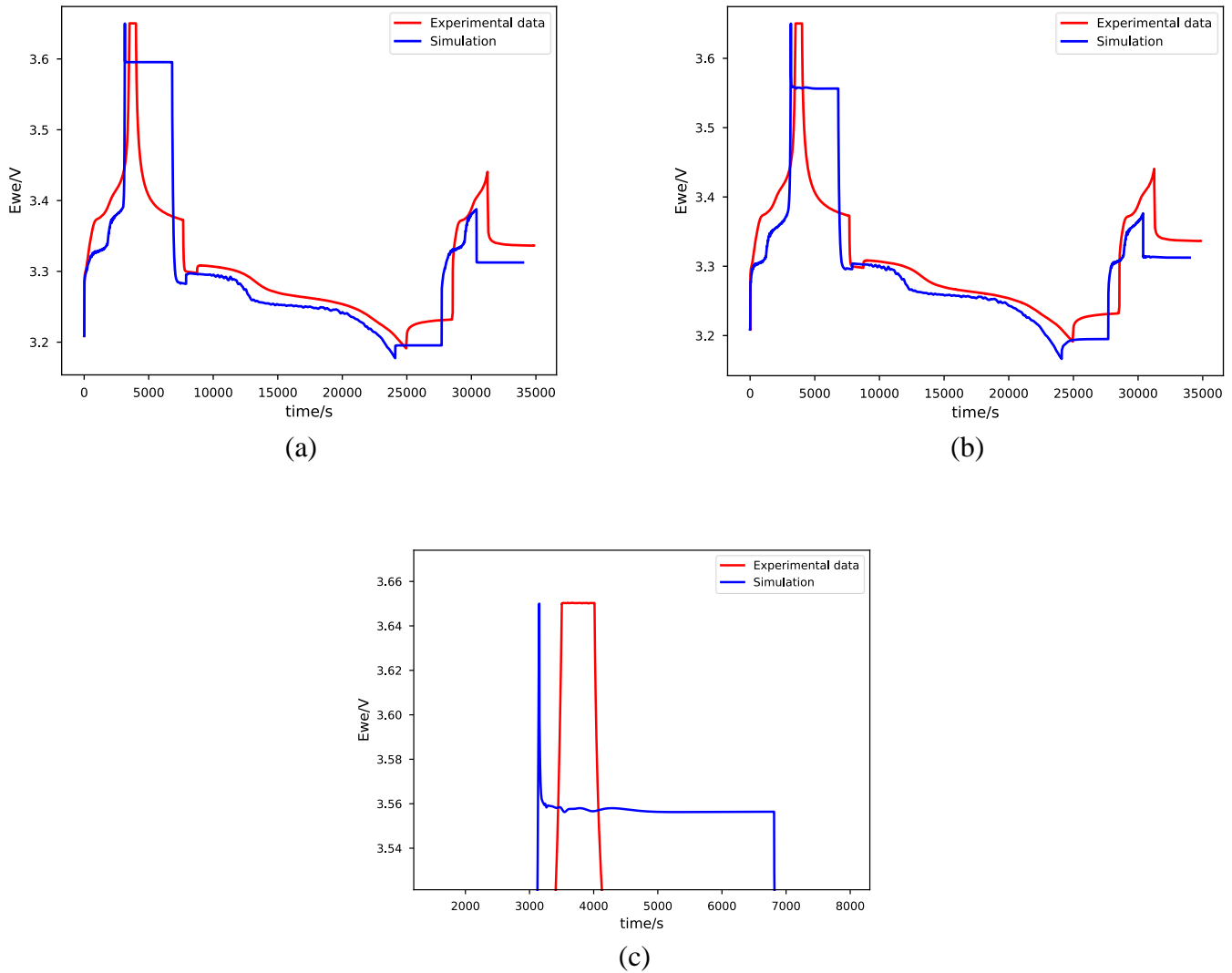
Figure 37, (a) shows the BEV application experimental data compared to a simulation with the thermodynamic values changed from default, (b) shows the same as (a) but when the simulation includes changed values for all the found parameters except for r_- which is default. (c) is a zoom in on the constant voltage and rest region in (a). The red curve is the experimental data, and the blue curve is the simulation.

From the Figure 37 (a) the full run can be seen. As Figure 37 (b) shows, the simulation has a longer resting phase between about 3000-10500 s compared to the experimental data where the phase is only between around 3500-4000 s. The flat part of the red curve is the constant voltage step that moves on to the next part of the sequence when limit |I|< 0.55 A is triggered or after 1 hour. The slope following the flat part of the red curve represents the 1-hour rest period when the cell relaxes to around 3.37 V. After that hour it can be seen that the slope is not flat and that the cell has not reached equilibrium yet. The experimental data and the

simulation indicate that the |I|-limit is triggered before the 1 hour had passed. In the simulation, this limit is triggered earlier and that the cell relaxes in a fast manner to around 3.56 V for the rest.

By moving in the simulated SOC window and plotting the experiment starting from the "Rest for 1 minute"-segment Figure 38 is made for the shortened experiment. The non-equilibrium state of the cell that exists in the experimental data before the segment is a bit difficult to account for in the simulation and will cause some difference between the graphs.
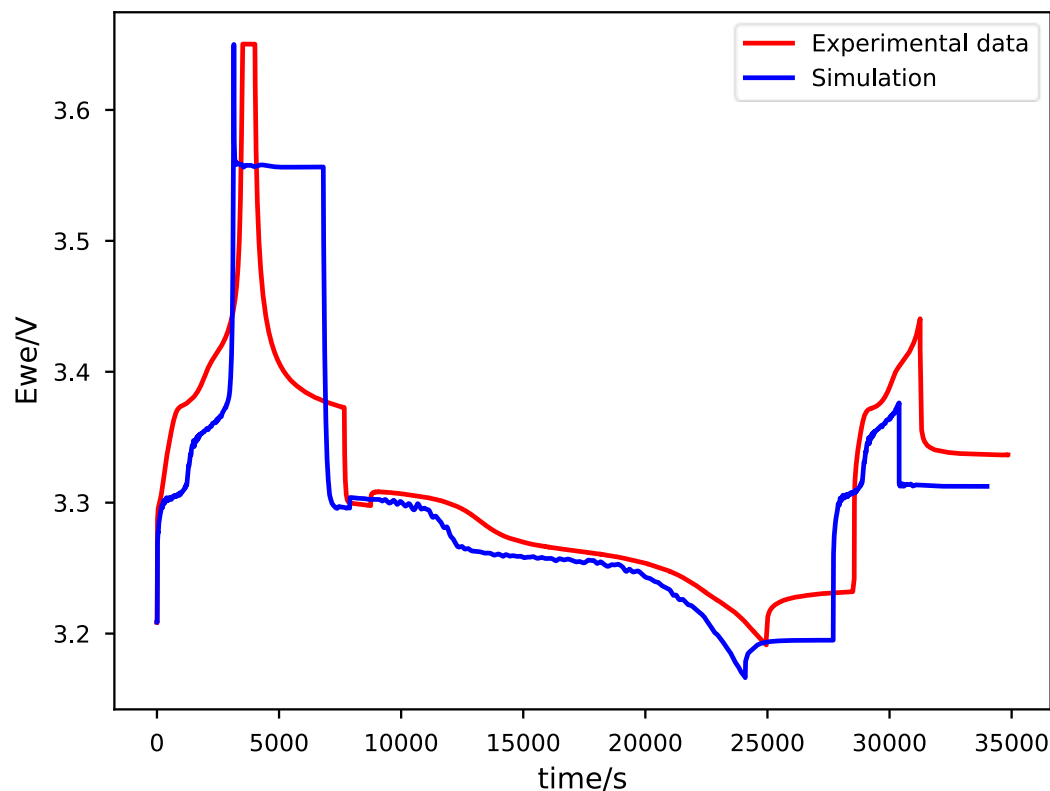
Figure 38, BEV application. The simulation with the found parameter values and with the negative particle radius value set to default.

From Figure 38 the simulation has similar curvature as the experimental data. The simulated curve matches the experimental data relatively well for the discharge parts of the run until around 17500 s, but that the voltage gap increases significantly as the cell is charged. At the endpoint, the voltage difference is clearly seen. It is unexpected since the same current is used which would result in a similar change in capacity and that the cell starts at the same voltage. This might be a result of that the cell is not at relaxed state in the start of these segment. The cell could continue to relax in the red curve which would give the endpoints different values. This could be tested by performing the test once again but letting the cell rest for more than 1 hour to reach equilibrium before starting the potential BEV application activities. Another theory is that the cell capacity is different in the experiment and simulation which would be the result of errors in the OCV-curve fitting and the found vales for the active particle fraction in the electrodes. A third theory to why there is a voltage in the end of the simulation is that

more capacity is entered into the cell in the experiment during the charge period than in the simulation as seen in Figure 38.

In Figure 39 (a), (b) and (c) below the thermodynamic, transport and kinetic parameters values are changed from the default to the new values one by one to see how the shape of the simulation changes.

(a)

(b)

(c)
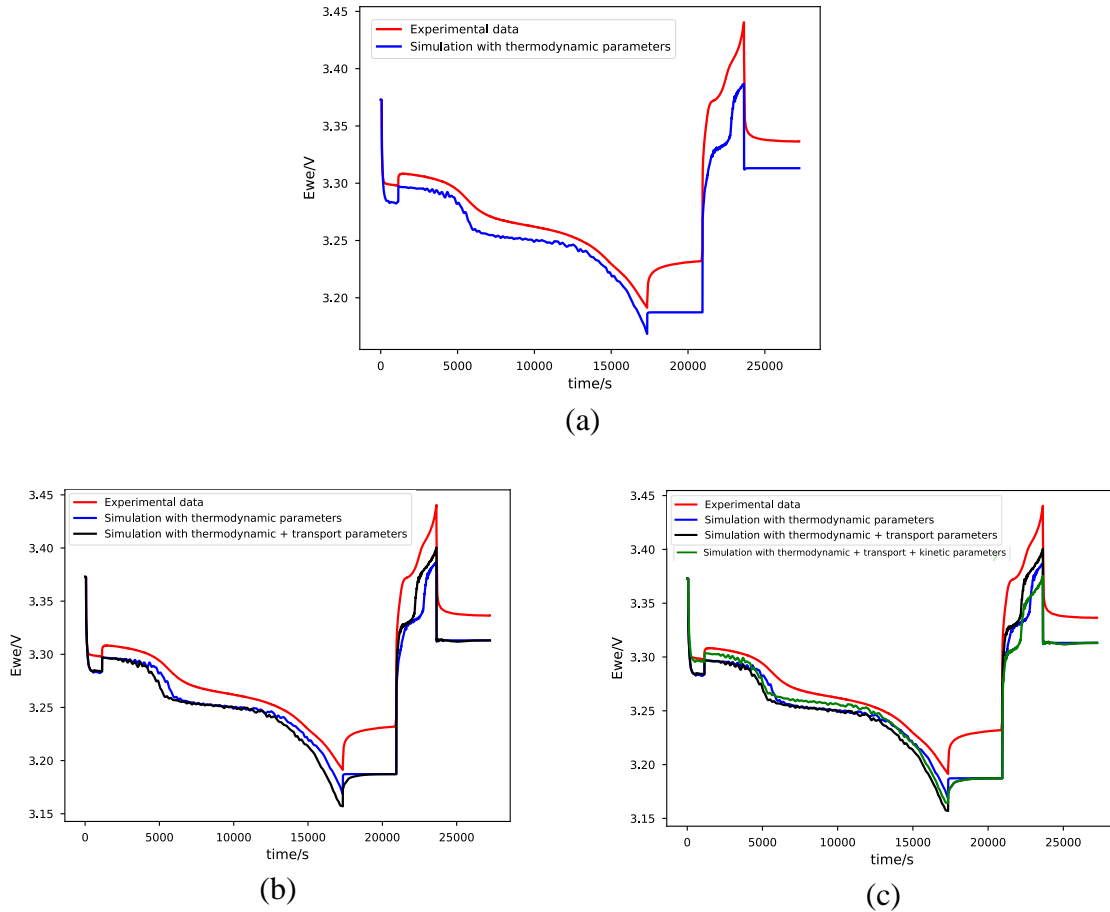
Figure 39, (a), (b) and (c). Red curve is the experimental data. All simulated curves have the negative particle radius set as default.

From Figure 39 (b) it can be seen that the simulation with the found thermodynamic and transport parameter values relaxes more than the simulation that only uses the found thermodynamic values at the 1-hour rest between the discharge and charge phase, around 17000 seconds. From Figure 39 (c) it can be seen that the simulation that uses the found thermodynamic, transport and kinetic parameter values fits closer to the experimental data than the other simulations for most of the discharge part but is further away during the charge part.

Alternative parameter values

By limiting the bounds of the negative particle radius and repeating the method but with some modifications seen in Appendix D, the BEV run is done with another set of parameter values to compare. For these parameter values, the simulation does not stop due to the negative particle radius but the simulation becomes infeasible since the maximum positive particle

surface concentration is triggered. The error lies in the new value of the k_{f-}. If all the parameter values are changed while the default value for k_{f-} is used, Figure 40 is created.
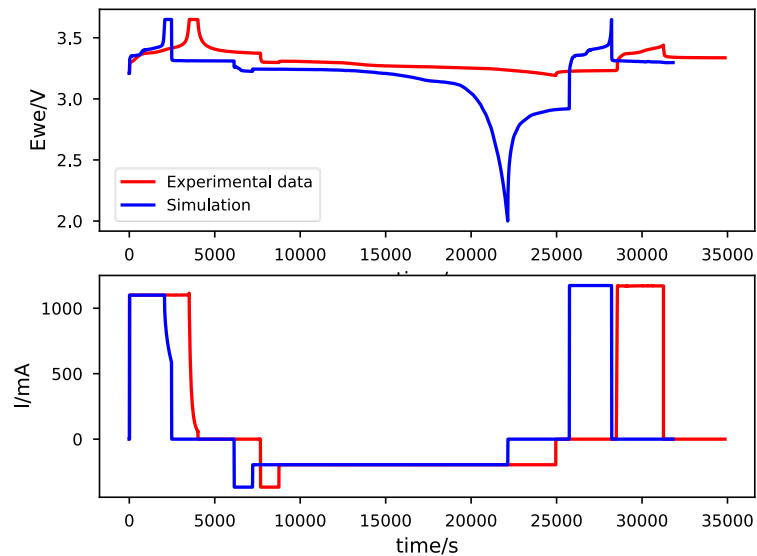
Figure 40, BEV run with alternative parameter values.

In comparison to Figure 38, Figure 40 shows a relatively deep discharge, almost down to the cut-off voltage.

4.6.2 Mild hybrid application

The found parameter values are used to simulate a possible mild hybrid application and is then compared to experimental data. The block diagram for the potential mild hybrid application can be found in Figure 41.
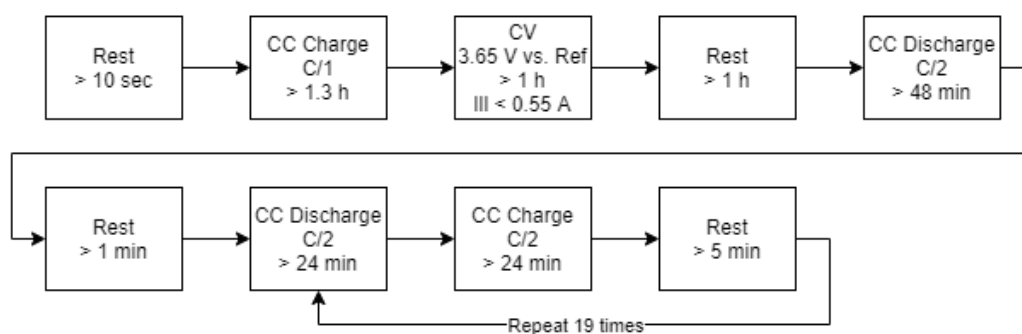
Figure 41, potential mild hybrid application block diagram

By plotting the full run with only the thermodynamic parameters, the beginning of the plot looks similar to the one for the BEV application. See Figure 42 below.
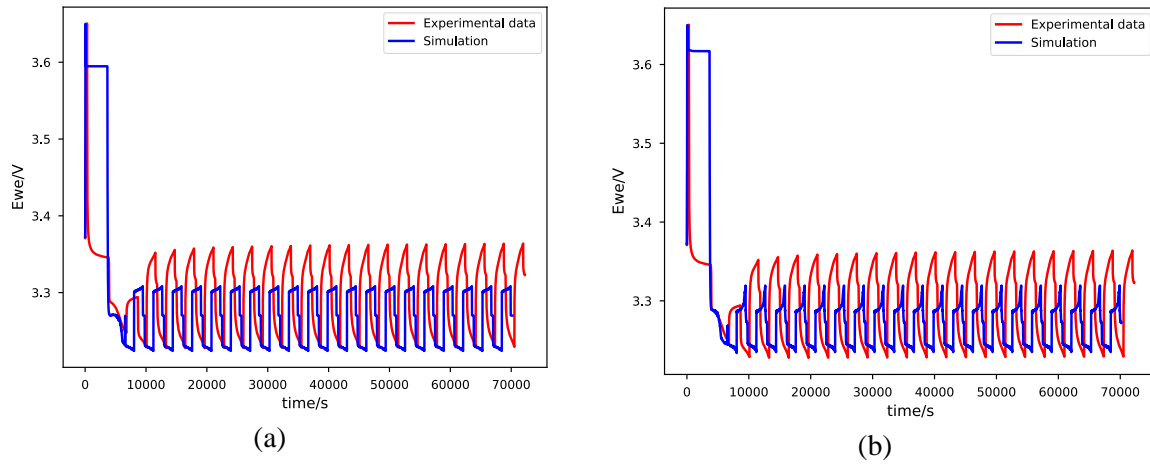
Figure 42, full Mild hybrid run (a) with only thermodynamic values changed (b) with all new values except for the negative particle radius.

Since the negative particle radius causes the simulation to stop in the potential BEV application, a simulation with the default value of that parameter can be seen in Figure 43 while the other found parameter values are used.
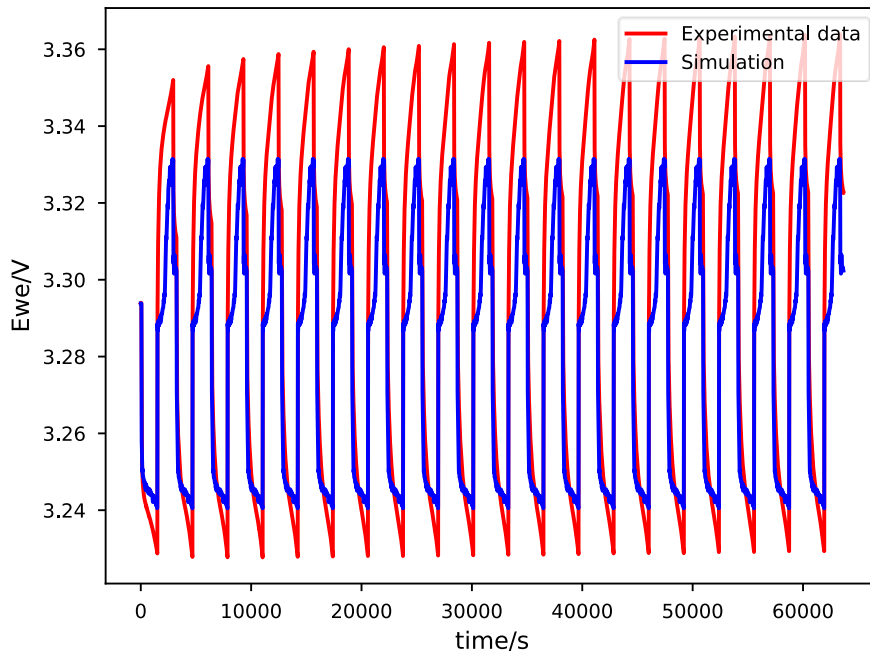
Figure 43, Potential mild hybrid application with the red curve representing experimental data and the blue curve the simulation with the found parameter values except for negative particle radius.

Figure 43 shows a better match between the simulation and experimental data, although the simulation does not reach the experimental end points of each charge and discharge phase. The experimental data moves higher up in voltage for each charging phase while the simulation reaches about the same voltage level.

In Figure 44 below, the difference from adding a set (thermodynamic, transport and kinetic parameters) of found parameter values can be seen. Figure 44.a shows the experimental data

and the simulation where the thermodynamic parameter values has been changed from the default. Figure 44.b shows the difference in appearance when the other parameter sets are used in the simulation.
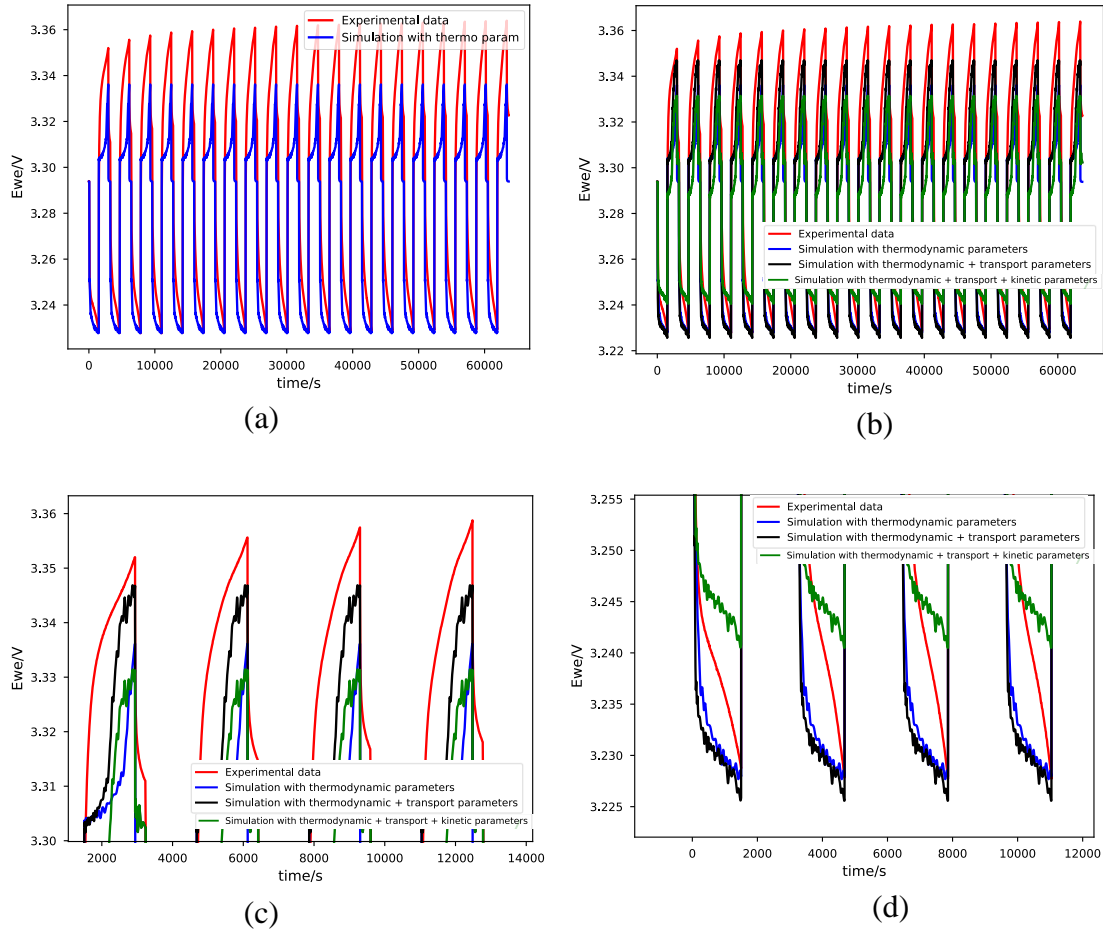
Figure 44. a, b, c, d. All simulated curves have the negative particle radius excluded.

Figure 44.c and 44.d it seems like the simulation comes closer to the end points of charge and discharge pulses of the experimental data when the kinetic parameter is not included. The voltage at the end of discharge is reached with only the thermodynamic parameters but the transport parameters make the relaxation more similar the experimental data. The simulation with all parameters except for the negative particle radius influences which voltage the simulation reaches after charge and discharge.

Alternative parameter values

Just as for the BEV application, the alternative parameter set found by limiting the bounds of the negative particle radius and repeating the method just as but with some modifications seen in Appendix D, the mild hybrid run will also be investigated. If all the parameter values are changed to the alternative parameter values while the default value for k_{f-} is used, Figure 45 is created.
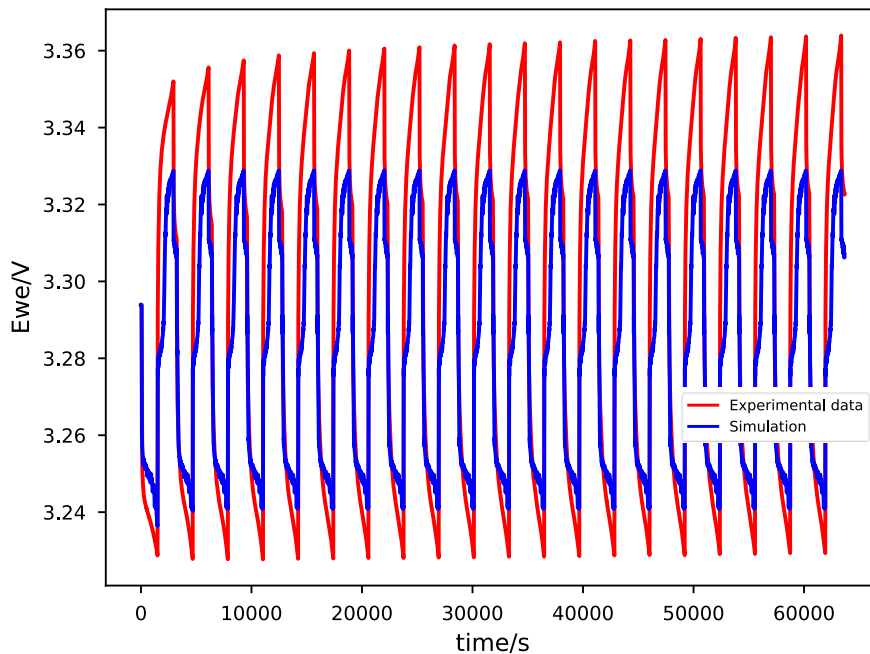
Figure 45, Mild hybrid run with alternative parameter values

In comparison to Figure 43, Figure 45 has a rather similar appearance.

5. DISCUSSION

From the sensitivity analysis, to disturb the parameters by ± 10 % might be an unrealistic disturbance if the parameters values would pass outside of a physical boundary. An alternative method is to find within which ranges the parameters are usually found and then disturb the parameters within that range. The risk of using the simpler method is assumed to be acceptable in order to get a quick and simple overview of the parameter's sensitivity.

From the sensitivity analysis, it seems like the electrode conductivities are not sensitive to the small changes of ± 10 % in the parameter values. This is an unexpected result since the conductivity is related to the resistance in the cell which would give linear dependence according to Ohms law. The lowest conductivity in the LFP electrode should reasonably limit the reaction rate more than the graphite electrode, although no difference is found. The effect is looked at in the *Sensitivity analysis* and in the *Mild hybrid application* and they gave similar outputs. The exchange current density for the LFP is lower than for graphite. From the Butler-Volmer equation, the largest exchange current density has the largest impact. It might be that the effect from the changed reaction rate for the LFP cannot be seen after 10 seconds and that the effect is visible first after a longer rest. This might also be something that the SPM does not capture.

The cell´s geometric parameters were measured in a reasonable accurate way to values that are comparable to the Prada 2013 parameter values. Even more points could have been used to measure the thickness of the current collector.

From the low-rate cycling curve fitting seen in Figure 26, the fitted simulation curve has a higher voltage at 100 % SOC compared to the experimental data. This error could lead to

unrealistic voltage values when the cell is working on high SOC levels. The OCV-curve is weighted extra to the graphite bumps in the middle of the SOC window while the endpoints are weighted less. In real applications, the full SOC window of the battery cell is rarely used because the risk is higher for irreversible side reaction, shorter lifetime etc. The LFP/C has a rather flat OCV curve and the change in voltage is concentrated at the higher SOC value. By operating up to around 83% SOC, the simulation fits reasonably well to the experimental data.

The stochiometric values within the electrodes are found through the OCV-curve fitting. For the LFP electrode these values are between 0.001-0.98 which would mean that a very large part of the SOC window of the LFP electrode is also used in the cell. This is a large usage of the LFP´s SOC window since the maximum range was 0-1. The method used gave these values but maybe another could be used to compare and validate the values. During conversation with Alexander Bessman and Pontus Svens, these ranges seem realistic.

Since thermodynamic parameters (geometric and found through the low-rate cycling test) are set before the transport and kinetic parameters are found, an error in them would cause errors in the other parameter values as well. The thickness of the geometrical parameters were measured in micrometers, and is sensitive to errors. When the electrode coating was scarpaed of, eyesight was used to determine when the surface was free of coating. Small rest pieces that were not visible with the eye might still be present on the surface which generate an error in the measurement.

In Table 9, there is a small difference between the charge and discharge capacity. It is expected that the charge capacity would be smaller than the discharge capacity due to irreversible side reactions. When the cell was cycled at C/50, this was seen. For the experimental tests, it would be good to make sure that the cell is at equilibrium condition before the comparison or fitting procedure begins. The risk is otherwise that possible relaxation from a previous activity on the cell can disturb and make it difficult to use as has been seen in the thesis.

In relation to Figure 37, the lack of relaxation in the simulation is likely due to errors in the OCV-curve from the low-rate cycling experiment. The OCV-curve is fitted with weights around the graphite "bumps" in the middle of the curve while the endpoints, when the cell is or is near fully charged or discharged, is weighted less to promote the fit of the bumps. This could be a reason why equilibrium points in the simulation does not fit the experimental data very well compared to other parts of the curve.

In relation to Figure 37. This difference could be a result of that all the parameter values has been found and fitted to experimental data when the cell is discharged. This is a weakness in the method that could be investigated in future work. Physically, the found parameters should be the same for charge and discharge but because of this validation, it seems reasonable to question if that is really the case. It might have been better to find mean values for the found and fitted parameters for both charge and discharge.

From the BEV application validation, the negative particle radius hit the upper bound in PyBaMM which stopped the simulation. This means that the parametrization is not optimal for this parameter and that the bounds are set too freely. The interpolation ranges within the literature that PyBaMM bases its values on could not work with the parameter value. From the mild hybrid application validation, it is seen that the negative particle radius affected the

fit in an unwanted way and gave unrealistic results. This is a further indicator that the parametrisation of the negative particle radius is not effective. A solution to this would be to limit the bounds more. The bounds for the negative particle radius were limited more, and an alternative method where the values from both the cell opening, low-rate cycling and GITT are used before the values of the factor to the negative electrodes reaction rate is found. The negative particle radius and reaction rate seem to be tightly connected when they aim to be fitted to the GITT or pulse test. When the bounds are less restricted, the negative particle radius finds its optimal value above the interpolation limit during the BEV run while the factor of the negative reaction rate stays in the middle of the bounds. The negative electrode radius bounds are limited, the factor to the negative electrodes reaction rate hits goes to the upper bound value and makes the BEV run unfeasible. A theory is that there are some other phenomenon taking place that is related to the negative particle radius and the negative electrode reaction rate that the adapted parameters does not capture. There can be some other unknown parameter that better represents the phenomena.

For the mild hybrid validation run, a theory why the experimental data and simulation look different from charge and discharge is related to the voltage level used. Around 3.3 V is the position of a graphite "bump" in the OCV curve which can be seen in *Background.*

The negative particle radius is shown to be relatively sensitive for both the GITT and the pulse test. The initial procedure is to find the parameter values from GITT and Pulse test when using the default and thermodynamic values. An alternative method when the parameter for the Pulse test is found when using both the default, thermodynamic and transport parameters is also tested. From both the procedures, it seems like the values for negative particle radius and negative electrode reaction rate are not successfully found. A conclusion can be made that the negative particle radius cannot be estimated accurately with this method.

From the *BEV* and *Mild hybrid validation* runs, the simulation appeared to fit better during discharge than charge. The physical parameter values should be the same for discharge and charge. A way to investigate this could be to make the parametrization for the charge part of the experiment, or to use data from both scenarios.

5.1 Future Work

For future work, the literature review could be extended in order to set even tighter bounds for the curve fit procedure. The reasonability of changing the parameters by 10% or more within the fitting procedure would also be relevant to investigate.

It would be interesting to fit even more parameters for every test to see which are sensitive for different experiments. By finding which parameters that are sensitive under which conditions, optimal tests could be formulated and tested to parameters experimentally. The particle radius could for example be analysed through scanning electron microscope.

The OCV has a big impact on the simulations. In the pseudo OCV-fitting (see *Results*) the experimental data, which the fitting is made on, is weighted to fit the graphite "bumps" in order to capture the phenomena well. In order to get a satisfying fit over the bumps, a lower weight is given to the endpoints of the experimental data. This gives a less accurate fit in the simulation when being in high and low SOC-regions. In order to get more accurate OCV-curves a GITT experiment with many more GITT pulses that maps up the equilibrium voltage

along the SOC window would be recommended. This is a time-consuming process that can take months and is not included in this thesis but could be done in future work.

The value of the diffusivity in the solid can vary depending on the choice of method as described in the *Background*. This makes it tricky to get an accurate value of the parameter. A comparison could be done by conducting tests with other methods such as current pulse relaxation, potential step chronoamperometry and AC impedance spectroscopy and compare the values received from GITT. The parameters gotten from the other tests could be used as parameter values in order to which value, and method, that is most suitable to use. This can be a part of future work since it did not fit within the time frame of this thesis.

During the curve fitting procedure of the simulation to the experimental data, the pulses in the end of the discharge, pulses eight, nine and ten with the low SOC levels, are the once that showed the most relaxation and matched the experimental data the best. A future work could be to investigate why the simulation showed that behaviour for these pulses and not for the others.

The pulse test is related to the SOC but not to the current rate since only the C/2 pulses are investigated due to time restrictions. The pulses with the lowest current rates are chosen to look at because they had a longer relaxation time before them. The effect of current rates is interesting to investigate in future work.

The long time needed for the cell to reach equilibrium conditions in the GITT test is likely due to the flat OCV-curve of the LFP/C cell. By running the time consuming GITT test first with 2-hour rest period and then the 4-hour rest took over half a month to conduct. A setting on the instrument that could sense when the variation in voltage is acceptably small would have been useful in this scenario. For future work, it would be recommended to be able to use this setting when performing GITT tests on LFP/C cells to make sure that equilibrium conditions are reached.

It would be interesting to investigate how parameters change due to degradation mechanisms with PyBaMM simulations. This could be done in future work.

When a method of parametrization has been found to be successful, there are computational problems that need to be solved in order to take the next step and use electrochemical battery models instead of empirical models for applications like BMS. To tackle the computational problems is a future work.

6. CONCLUSION

The goals of the thesis were to parameterize the SPM from the open source PyBaMM modelling library for commercial LFP cells. 17 parameters are investigated, and 14 parameter values are adapted from the Prada 2013 parameter set. Another goal is to use literature survey as well as experiments in the parametrization procedure. This took form as Table 2 as well as the methods used. Three types of experimental tests are done to be able to estimate the parameter values from the data. The third goal is to validate the model against drive cycles. Two potential applications for a BEV and Mild hybrid are tested experimentally and used as validation cycles.

The validation shows that this method and model cannot be used to find parameter values for the negative particle radius.

Physics-based models have several advantages towards empirical models when it comes to describing electrochemical systems. Parametrization is a time-consuming process but necessary to make the model describe the system in an accurate way. A method to parameterize a battery cell is complicated and more research is needed in the field.

7. REFERENCES

[1]   IPCC, 2014: *Climate Change 2014: Synthesis Report. Contribution of Working Groups I, II and III to the Fifth Assessment Report of the Intergovernmental Panel on Climate Change* [Core Writing Team, R.K. Pachauri and L.A. Meyer (eds.)]. IPCC, Geneva, Switzerland, 151 pp. Avaliable: https://www.ipcc.ch/report/ar5/syr/

[2]   Lindsey, Rebecca and Dahlman, LuAnn. *Climate Change: Global Temperature*. NOAA Climate.gov. March 15, 2021. Accessed June 4, 2021. Avalaible: https://www.climate.gov/news-features/understanding-climate/climate-change-global-temperature

[3]   Ritchie, Hannah. *Sector by sector: where do global greenhouse gas emissions come from?*, Our world in data. September 18, 2020. Accessed on: April 5, 2021. Avaliable: https://ourworldindata.org/ghg-emissions-by-sector

[4]   Ritchie, Hannah and Roser, Max. *CO_2 and Greenhouse Gas Emissions,* Our world in data. Published May 2017 and last revised August 2020. Accessed on: April 5, 2021. Avaliable: https://ourworldindata.org/co2-and-other-greenhouse-gas-emissions

[5]   Göran Lindbergh, "Class lecture, topic: Lecture 1 Electrochemcial energy devices KE2300". Course: Electrochemical energy devices KE2300. Applied Electrochemistry, Department of Chemical Engineering School of Engineering Sciences in Chemistry, Biotechnology and Health, KTH - Royal Institute of Technology. 8 N," 2019.

[6]   A. Fotouhi, D. J. Auger, K. Propp, S. Longo, and M. Wild, "A review on electric vehicle battery modelling: From Lithium-ion toward Lithium-Sulphur," *Renewable and Sustainable Energy Reviews*, vol. 56. Elsevier Ltd, pp. 1008–1021, Apr. 01, 2016, doi: 10.1016/j.rser.2015.12.009.

[7]   P. Svens, "Class lecture, topic: 'Lithium-ion batteries for electrified vehicles', Course: Electrochemical energy devices KE2300. Applied Electrochemistry, Department of Chemical Engineering School of Engineering Sciences in Chemistry, Biotechnology and Health, KTH ," 2019.

[8]   Dahn, Jeff and Ehrlich, "*Lithium-ion batteries*", Linden's handbook of batteries, 4th ed. New York: McGraw-Hill, 2011. Chapter 26.

[9]   W. Chen, J. Liang, Z. Yang, and G. Li, "A review of lithium-ion battery for electric vehicle applications and beyond," in *Energy Procedia*, Feb. 2019, vol. 158, pp. 4363–4368, doi: 10.1016/j.egypro.2019.01.783.

[10]   A. M. Bizeray, J. Kim, S. R. Duncan, and D. A. Howey, "Identifiability and Parameter Estimation of the Single Particle Lithium-Ion Battery Model," *IEEE Transactions on Control Systems Technology*, pp. 1862–1877, Sep. 2019.

[11]   2020 PyBaMM Team. "*PyBaMM*." Accessed Jun. 05, 2021. Avaliable at: https://www.pybamm.org

[12]   E. Prada, D. Di Domenico, Y. Creff, J. Bernard, V. Sauvant-Moynot, and F. Huet, "A Simplified Electrochemical and Thermal Aging Model of LiFePO 4-Graphite Li-ion Batteries: Power and Capacity Fade Simulations," *J. Electrochem. Soc.*, vol. 160 (4), pp. A616–A628, 2013, doi: 10.1149/2.053304jes.

[13]   R. Lindström Wreland, "Class lecture, topic: 'Battery II', Course: Electrochemical energy devices KE2300. Applied Electrochemistry, Department of Chemical

Engineering School of Engineering Sciences in Chemistry, Biotechnology and Health, KTH - Royal Institute of Technology. 8 N," 2019.

[14] A. Cornell, "Class lecture, topic: 'Cell voltage and electrode potential', Course: Applied electrochemistry KE2110. Applied Electrochemistry, Department of Chemical Engineering School of Engineering Sciences in Chemistry, Biotechnology and Health, KTH - Royal institut," 2019.

[15] R. Lindström Wreland, "Class lecture, topic: 'Battery I', Course: Electrochemical energy devices KE2300. Applied Electrochemistry, Department of Chemical Engineering School of Engineering Sciences in Chemistry, Biotechnology and Health, KTH - Royal Institute of Technology. 5 No."

[16] A. Cornell, "Class lecture, topic: 'Electrode kinetics', Course: Applied electrochemistry KE2110. Applied Electrochemistry, Department of Chemical Engineering School of Engineering Sciences in Chemistry, Biotechnology and Health, KTH - Royal institute of technology.," 2019.

[17] Newman, John S, "*Introduction* 1", in Electrochemical engineering,second edition. New Jersey, USA. Prentice Hall, 1991, *The diffusion layer*, section 1.5., 9 pp.

[18] A. K. Padhi, K. 5 Nanjundaswamy, and J. B. Goodenough, "Phospho-olivines as Positive-Electrode Materials forRechargeable Lithium Batteries," *16. E. M. Genies S. Picart, Synth. Met*, vol. 144, no. 4, p. 16, 1997.

[19] J.-M. Tarascon and M. Armand, "Issues and challenges facing rechargeable lithium batteries," *Nature*, vol. 414, no. 6861, pp. 359–367, Nov. 2001, doi: 10.1038/35104644.

[20] A. R. Huggins, "Insertion Reaction Electrodes," in *Advanced Batteries*, Boston, MA: Springer US, 2009, pp. 101–122.

[21] A. Blidberg, "LFP-course," May 18, 2021. Internal course at Scania CV.

[22] H. D. Abruña, Y. Kiya, and J. C. Henderson, "Batteries and electrochemical capacitors," *Phys. Today*, vol. 61, no. 12, pp. 43–47, 2008.

[23] N. Sharma and M. Wagemaker, "Lithium-Ion Batteries," Springer, Cham, 2015, pp. 139–203.

[24] Ogumi Z., Inaba M. (2002) Carbon Anodes. In: van Schalkwijk W.A., Scrosati B. (eds) Advances in Lithium-Ion Batteries. Springer, Boston, MA. https://doi-org.focus.lib.kth.se/10.1007/0-306-47508-1_3

[25] C. Delmas, M. Maccario, L. Croguennec, F. Le Cras, and F. Weill, "Lithium deintercalation in LiFePO4 nanoparticles via a domino-cascade model," *Nat. Mater.*, vol. 7, no. 8, pp. 665–671, Aug. 2008, doi: 10.1038/nmat2230.

[26] A. Barai *et al.*, "A comparison of methodologies for the non-invasive characterisation of commercial Li-ion cells," *Progress in Energy and Combustion Science*, vol. 72. Elsevier Ltd, pp. 1–31, May 01, 2019, doi: 10.1016/j.pecs.2019.01.001.

[27] M. A. Danzer and M. Petzl, "Advancements in OCV Measurement and Analysis for Lithium-Ion Batteries," *IEEE Trans. ENERGY Convers.*, vol. 28, no. 3, pp. 675–681, Sep. 2013, Accessed: May 24, 2021. [Online]. Available: https://ieeexplore-ieee-org.focus.lib.kth.se/stamp/stamp.jsp?tp=&arnumber=6517504.

[28] W. Dreyer, J. Jamnik, C. Guhlke, R. Huth, J. Moškon, and M. Gaberšček, "The thermodynamic origin of hysteresis in insertion batteries," *Nat. Mater.*, vol. 9, no. 5, pp. 448–453, May 2010, doi: 10.1038/nmat2730.

[29] V. Srinivasan and J. Newman, "Existence of Path-Dependence in the LiFePO[sub 4] Electrode," *Electrochem. Solid-State Lett.*, vol. 9, no. 3, p. A110, 2006, doi: 10.1149/1.2159299.

[30] M. A. Roscher and D. U. Sauer, "Dynamic electric behavior and open-circuit-voltage modeling of LiFePO4-based lithium ion secondary batteries," *J. Power Sources*, vol. 196, no. 1, pp. 331–336, Jan. 2011, doi: 10.1016/j.jpowsour.2010.06.098.

[31] S. Lee, J. Kim, J. Lee, and B. H. Cho, "State-of-charge and capacity estimation of lithium-ion battery using a new open-circuit voltage versus state-of-charge," *J. Power Sources*, vol. 185, no. 2, pp. 1367–1373, Dec. 2008, doi: 10.1016/j.jpowsour.2008.08.103.

[32] J. Groot, "III THESIS FOR THE DEGREE OF LICENTIATE OF ENGINEERING State-of-Health Estimation of Li-ion Batteries: Cycle Life Test Methods."

[33] D. A. Howey *et al.*, "Making a case for battery modelling," *Interface - Electrochem. Soc.*, vol. 29, no. 4, pp. 32–33, 2020, Accessed: Jun. 05, 2021. [Online]. Available: https://issuu.com/ecs1902/docs/2020-if-win.

[34] G. Alexander and H. Anton, "Parametrization Of A Simplified Physical Battery Model," Feb. 2019, pp. 215–220, doi: 10.3384/ecp19157215.

[35] W. Li *et al.*, "Parameter sensitivity analysis of electrochemical model-based battery management systems for lithium-ion batteries," *Appl. Energy*, vol. 269, p. 115104, Jul. 2020, doi: 10.1016/j.apenergy.2020.115104.

[36] "Development of Experimental Techniques for Parameterization of Multi-scale Lithium-ion Battery Models," 2020, doi: 10.1149/1945-7111/ab9050.

[37] S. G. Marquis, V. Sulzer, R. Timms, C. P. Please, and S. J. Chapman, "An asymptotic derivation of a single particle model with electrolyte," *arXiv*. arXiv, May 29, 2019, doi: 10.1149/2.0341915jes.

[38] M. Doyle, T. F. Fuller, and J. Newman, "Modeling of Galvanostatic Charge and Discharge of the Lithium/Polymer/Insertion Cell," *J. Electrochem. Soc.*, vol. 140, no. 6, pp. 1526–1533, Jun. 1993, doi: 10.1149/1.2221597.

[39] E. Namor, D. Torregrossa, R. Cherkaoui, and M. Paolone, "Parameter identification of a lithium-ion cell single-particle model through non-invasive testing," *J. Energy Storage*, vol. 12, pp. 138–148, Aug. 2017, doi: 10.1016/j.est.2017.04.008.

[40] A. Raue *et al.*, "Structural and practical identifiability analysis of partially observed dynamical models by exploiting the profile likelihood," *Bioinformatics*, vol. 25, no. 15, pp. 1923–1929, Aug. 2009, doi: 10.1093/bioinformatics/btp358.

[41] N. Jin, D. L. Danilov, P. M. J. Van den Hof, and M. C. F. Donkers, "Parameter estimation of an electrochemistry-based lithium-ion battery model using a two-step procedure and a parameter sensitivity analysis," *Int. J. Energy Res.*, vol. 42, no. 7, pp. 2417–2430, Jun. 2018, doi: 10.1002/er.4022.

[42] Lain, Brandon, and Kendrick, "Design Strategies for High Power vs. High Energy

Lithium Ion Cells," *Batteries*, vol. 5, no. 4, p. 64, Oct. 2019, doi: 10.3390/batteries5040064.

[43] The PyBaMM Team. "*Parameters Sets — PyBaMM 0.4.0 documentation.*" Avaliable at: https://pybamm.readthedocs.io/en/latest/source/parameters/parameter_sets.html. Accessed Jun. 05, 2021.

[44] M. Farkhondeh and C. Delacourt, "Mathematical Modeling of Commercial LiFePO 4 Electrodes Based on Variable Solid-State Diffusivity," *J. Electrochem. Soc.*, vol. 159, no. 2, pp. A177–A192, Jan. 2011, doi: 10.1149/2.073202jes.

[45] T. R. Ashwin, A. McGordon, and P. A. Jennings, "A mass transfer based variable porosity model with particle radius change for a Lithium-ion battery," *Electrochim. Acta*, vol. 232, pp. 203–214, Apr. 2017, doi: 10.1016/j.electacta.2017.02.129.

[46] V. Srinivasan and J. Newman, "Discharge Model for the Lithium Iron-Phosphate Electrode," *J. Electrochem. Soc.*, vol. 151, no. 10, p. A1517, Sep. 2004, doi: 10.1149/1.1785012.

[47] M. Park, X. Zhang, M. Chung, G. B. Less, and A. M. Sastry, "ARTICLE IN PRESS A review of conduction phenomena in Li-ion batteries," *J. Power Sources xxx*, 2010, doi: 10.1016/j.jpowsour.2010.06.060.

[48] T. D. Tran, J. H. Feikert, R. W. Pekala, and K. Kinoshita, "Rate effect on lithium-ion graphite electrode performance," 1996.

[49] T. L. Kirk, C. P. Please, and S. J. Chapman, "Physical modelling of the slow voltage relaxation phenomenon in lithium-ion batteries."

[50] A. M. Bizeray, J.-H. Kim, S. R. Duncan, and D. A. Howey, "Identifiability and Parameter Estimation of the Single Particle Lithium-Ion Battery Model," *IEEE Trans. Control Syst. Technol.*, vol. 27, no. 5, pp. 1862–1877, Sep. 2019, doi: 10.1109/TCST.2018.2838097.

[51] X. G. Yang and C. Y. Wang, "Understanding the trilemma of fast charging, energy density and cycle life of lithium-ion batteries," *J. Power Sources*, vol. 402, pp. 489–498, Oct. 2018, doi: 10.1016/j.jpowsour.2018.09.069.

[52] R. Zhao, J. Liu, and F. Ma, "Cathode Chemistries and Electrode Parameters Affecting the Fast Charging Performance of Li-Ion Batteries," *J. Electrochem. Energy Convers. Storage*, vol. 17, no. 2, May 2020, doi: 10.1115/1.4045567.

[53] Askeland D.R. (1996) Ceramic Materials. In: The Science and Engineering of Materials. Springer, Boston, MA. https://doi-org.focus.lib.kth.se/10.1007/978-1-4899-2895-5_14

[54] Tran, T. D, Feikert, J. H, Pekala, R. W, and Kinoshita, K, "Rate effect on lithium-ion graphite electrode performance," *Journal of applied electrochemistry*, vol. 26, no. 11, pp. 1161–1167, 1996, doi: 10.1007/BF00243741.

[55] Chang, Y.-C, Jong, J.-H, and Fey, G. T.-K, "Kinetic characterization of the electrochemical intercalation of lithium ions into graphite electrodes," *Journal of the Electrochemical Society*, vol. 147, no. 6, pp. 2033–2038, 2000, doi: 10.1149/1.1393481.

[56] E. Frackowiak and F. Béguin, "Carbon materials for the electrochemical storage of

energy in capacitors," *Carbon*, vol. 39, no. 6. Elsevier Ltd, pp. 937–950, May 01, 2001, doi: 10.1016/S0008-6223(00)00183-4.

[57]   Z. Hui and L. Tao, "Lithium-ion Battery Series Product Specification Lithium-ion Battery Series." Available at: www.heter.biz.

[58]   The SciPy community. "Scipy.optimize.curve_fit — SciPy v1.6.3 Reference Guide." Avaliable at: https://docs.scipy.org/doc/scipy/reference/generated/scipy.optimize.curve_fit.html. Accessed June 5, 2021.

[59]   M. Dubarry and G. Baure, "Perspective on Commercial Li-ion Battery Testing, Best Practices for Simple and Effective Protocols," *Electronics*, vol. 9, no. 1, p. 152, Jan. 2020, doi: 10.3390/electronics9010152.

[60]   A. Barai *et al.*, "A comparison of methodologies for the non-invasive characterisation of commercial Li-ion cells," *Prog. Energy Combust. Sci.*, vol. 72, pp. 1–31, May 2019, doi: 10.1016/j.pecs.2019.01.001.

[61]   Häggblom, Kurt-Erik. "*5. Enkla dynamiska system.*" Reglerteknik grundkurs. 2005. Chapter 5. Accessed: Apr. 19, 2021. [Online]. Available at: http://www.users.abo.fi/khaggblo/RTG/RTGk.pdf.

8. APPENDIX

Appendix A – Parameter values in the Prada2013 parameter set

Table 19. *Prada 2013 parameter values.*

Parameter	Value	Unit	Parameter	Value	Unit
1 + dlnf/dlnc	1.0	-	Ambient temperature	298.15	K
Cation transference number	0.2594	-	Cell capacity	1.1	Ah
Current function	4.4	A	Electrode height	0.0649	m
Electrode width	1.78	m	Electrolyte conductivity	function electrolyte_conductivity_Nyman2008 at 0x000002D24C482D30	S.m-1
Electrolyte diffusivity	function electrolyte_diffusivity_Nyman2008 at 0x000002D24C482DC0	m2.s-1	Heat transfer coefficient	10.0	W.m-2.K-1
Initial concentration in electrolyte	1200.0	mol.m-3	Initial concentration in negative electrode	28831.45783	mol.m-3
Initial concentration in positive electrode	35.3766672	mol.m-3	Initial temperature	298.15	K
Lower voltage cut-off	2.0	V	Maximum concentration in negative electrode	33133.0	mol.m-3
Maximum concentration in positive electrode	22806.0	mol.m-3	Negative current collector conductivity	58411000.0	S.m-1
Negative current collector density	8960.0	kg.m-3	Negative current collector specific heat capacity	385.0	J.kg-1.K-1
Negative current collector	401.0	W.m-1.K-1	Negative current collector thickness	1e-05	m

thermal conductivity					
Negative electrode Bruggeman coefficient (electrode)	1.5	-	Negative electrode Bruggeman coefficient (electrolyte)	1.5	-
Negative electrode OCP entropic change	0.0	V.K-1	Negative electrode active material volume fraction	0.75	-
Negative electrode cation signed stoichiometry	-1.0	-	Negative electrode charge transfer coefficient	0.5	-
Negative electrode conductivity	215.0	S.m-1	Negative electrode density	1657.0	kg.m-3
Negative electrode diffusivity	3.3e-14	m2.s-1	Negative electrode double-layer capacity	0.2	F.m-2
Negative electrode electrons in reaction	1.0	-	Negative electrode exchange-current density	function graphite_LGM50_electrolyte_exchange_current_density_Chen2020 at 0x000002D24C4073A0	A.m-2
Negative electrode porosity	0.25	-	Negative electrode specific heat capacity	700.0	J.kg-1.K-1
Negative electrode thermal conductivity	1.7	W.m-1.K-1	Negative electrode thickness	3.6e-05	m
Negative particle radius	5.86e-06	m	Negative tab centre y-coordinate	0.06	m

Negative tab centre z-coordinate	0.1369999999999998	m	Negative tab width	0.04	m
Number of cells connected in series to make a battery	1.0	-	Number of electrodes connected in parallel to make a cell	1.0	-
Positive current collector conductivity	36914000.0	S.m-1	Positive current collector density	2700.0	kg.m-3
Positive current collector specific heat capacity	897.0	J.kg-1.K-1	Positive current collector thermal conductivity	237.0	W.m-1.K-1
Positive current collector thickness	1.9e-05	m	Positive electrode Bruggeman coefficient (electrode)	1.5	-
Positive electrode Bruggeman coefficient (electrolyte)	1.5	-	Positive electrode OCP	function LFP_ocp_ashfar2017 at 0x000002D24C4B1160	V
Positive electrode OCP entropic change	0.0	V.K-1	Positive electrode active material volume fraction	0.28485556	-
Positive electrode cation signed stoichiometry	-1.0	-	Positive electrode charge transfer coefficient	0.5	-
Positive electrode conductivity	0.33795074	S.m-1	Positive electrode density	2341.17	kg.m-3
Positive electrode diffusivity	5.9e-18	m2.s-1	Positive electrode double-layer capacity	0.2	F.m-2
Positive electrode	1.0	-	Positive electrode	function LFP_electrolyte	A.m-2

electrons in reaction			exchange-current density	_exchange_current_density_kashkooli2017 at 0x000002D24C4B10D0	
Positive electrode porosity	0.12728395	-	Positive electrode specific heat capacity	1100.0	J.kg-1.K-1
Positive electrode thermal conductivity	2.1	W.m-1.K-1	Positive electrode thickness	8.1e-05	m
Positive particle radius	1e-08	m	Positive tab centre y-coordinate	0.147	m
Positive tab centre z-coordinate	0.1369999999999998	m	Positive tab width	0.04	m
Reference OCP vs SHE in the negative electrode	nan	V	Reference OCP vs SHE in the positive electrode	nan	V
Reference temperature	298.15	K	Separator Bruggeman coefficient (electrode)	1.5	-
Separator Bruggeman coefficient (electrolyte)	1.5	-	Separator density	397.0	kg.m-3
Separator porosity	0.47	-	Separator specific heat capacity	700.0	J.kg-1.K-1
Separator thermal conductivity	0.16	W.m-1.K-1	Separator thickness	1.8e-05	m
Typical current	30.0	A	Typical electrolyte concentration	1000.0	mol.m-3
Upper voltage cut-off	4.4	V	Negative electrode OCP	graphite_LGM50_ocp_Chen2020	V

Appendix B – Potential Mild hybrid application validation plots with the positive particle radius
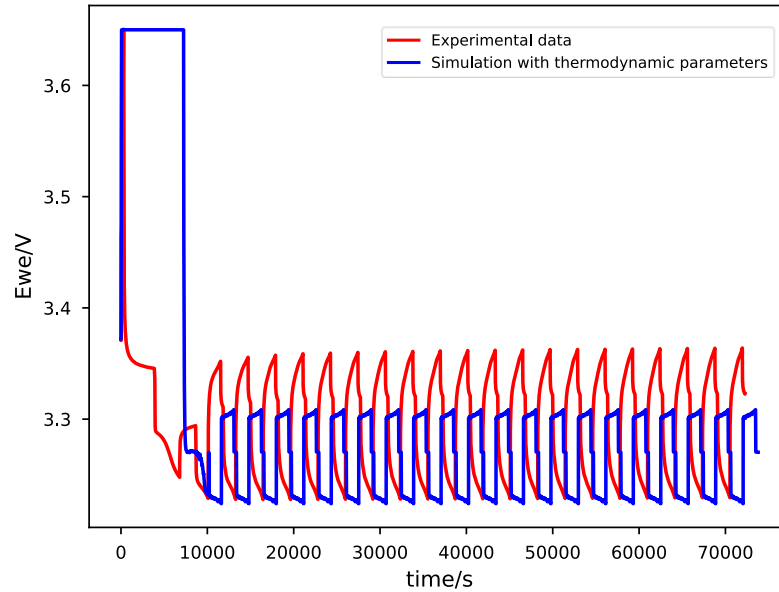
Figure 46, full run of mild hybrid potential application.

Just as for the potential BEV application plot, the constant voltage phase is ended since the |I| limit is reached in the experimental data while not in the simulation. The simulation also misses the relaxation during the one hour rest phase. In a similar way as the potential BEV application, the potential mild hybrid application run will also be shorten in Figure 47.
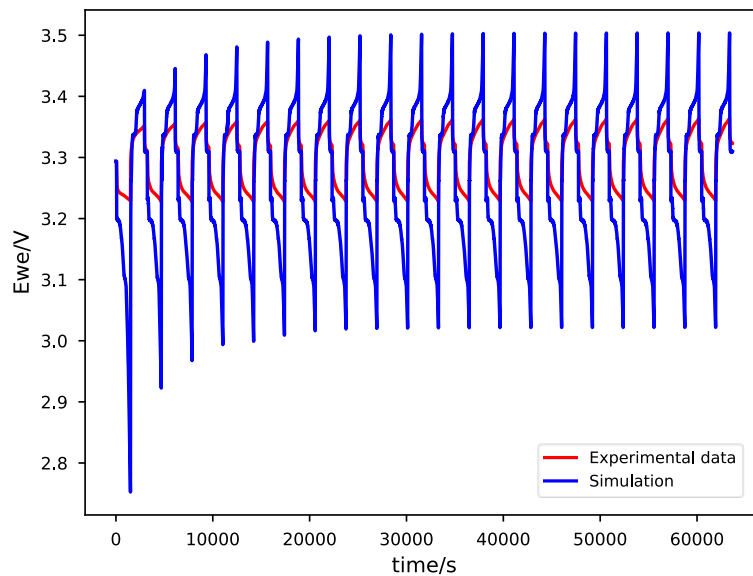
Figure 47, Potential mild hybrid application. The blue curve the simulation with the found parameter values.

Figure 47 shows a bad match between the simulated and experimental data. For this simulation PyBaMM did not stop the run because of interpolation issues as for the potential BEV application. The simulated blue curve moves in a large voltage range than the experimental data. In order to see each parameter types effect, Figure 48 is made.

(a)

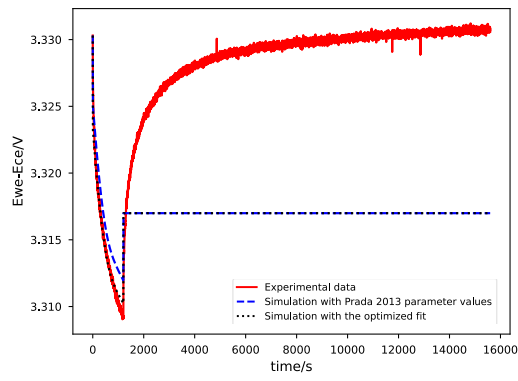

(b)

(c)
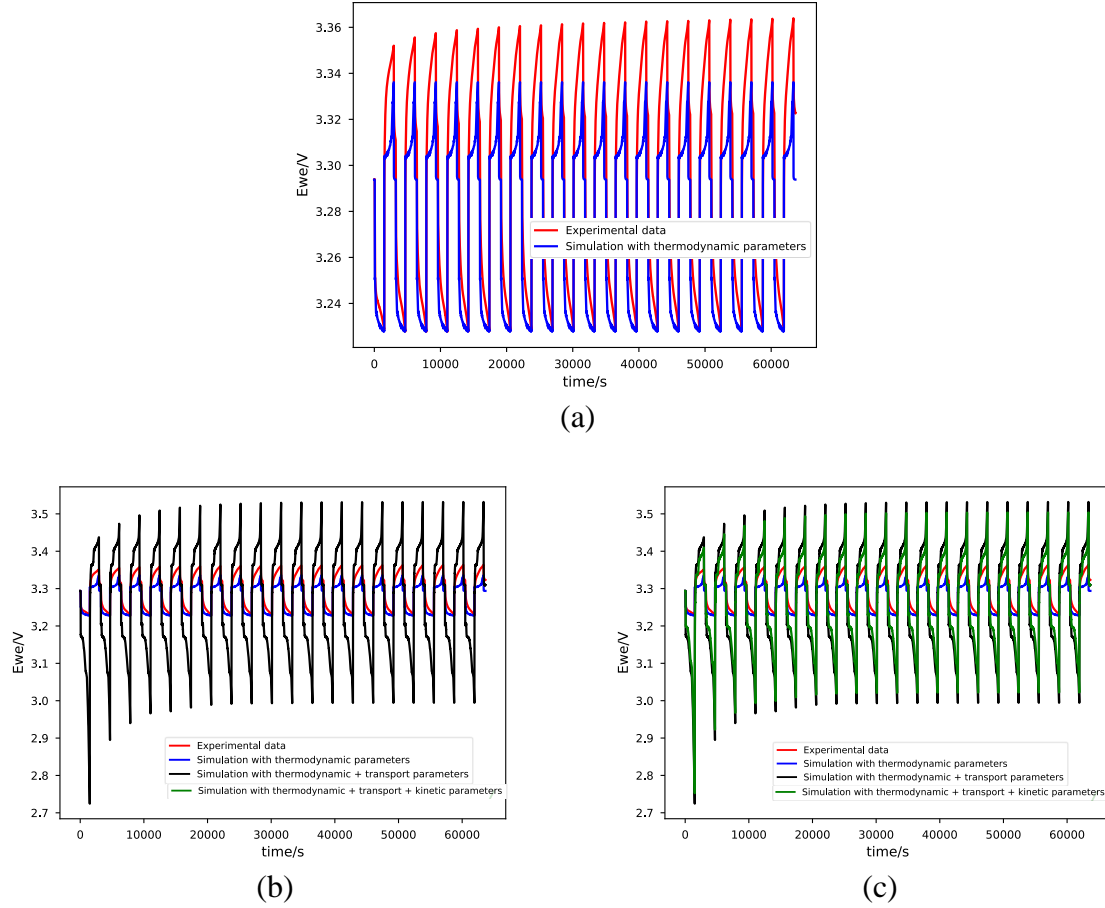
Figure 48 a, b and c.

Appendix C – Curve fit plots for each pulse

<u>GITT version 1</u>

(a)

(b)

(c)

(d)

(e)

(f)

(g)

(h)

(i)

(j)
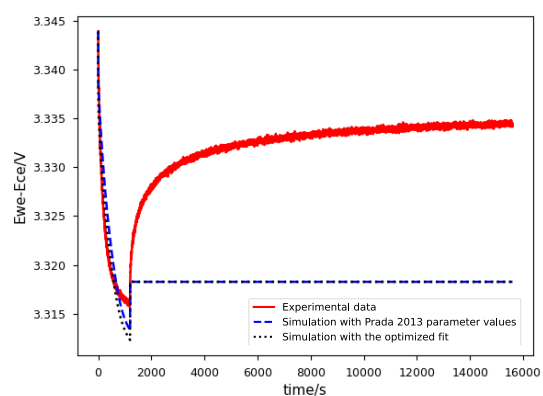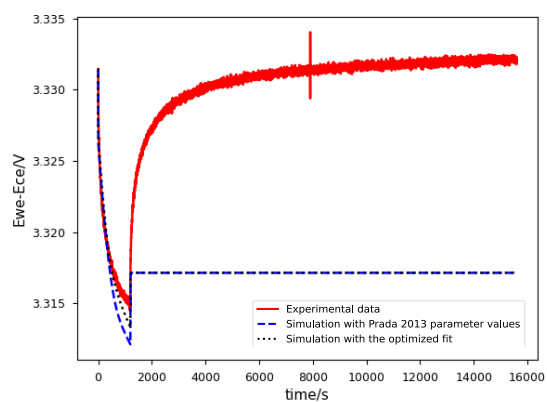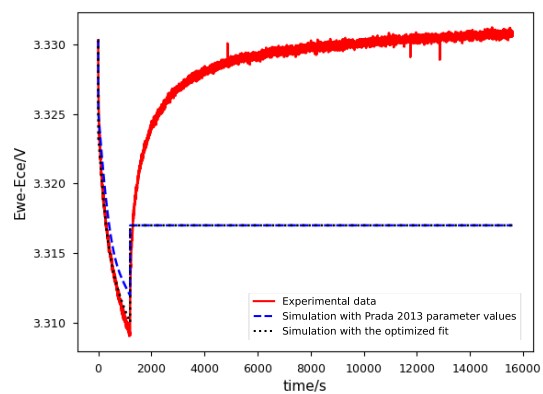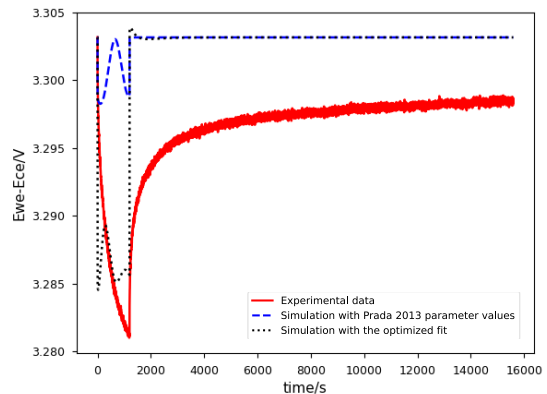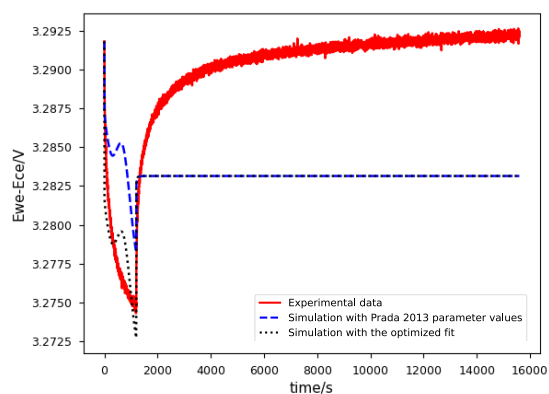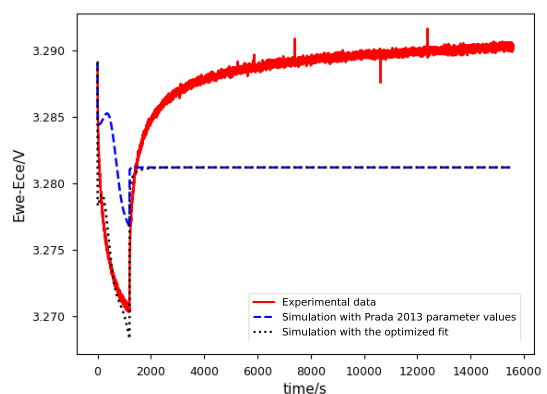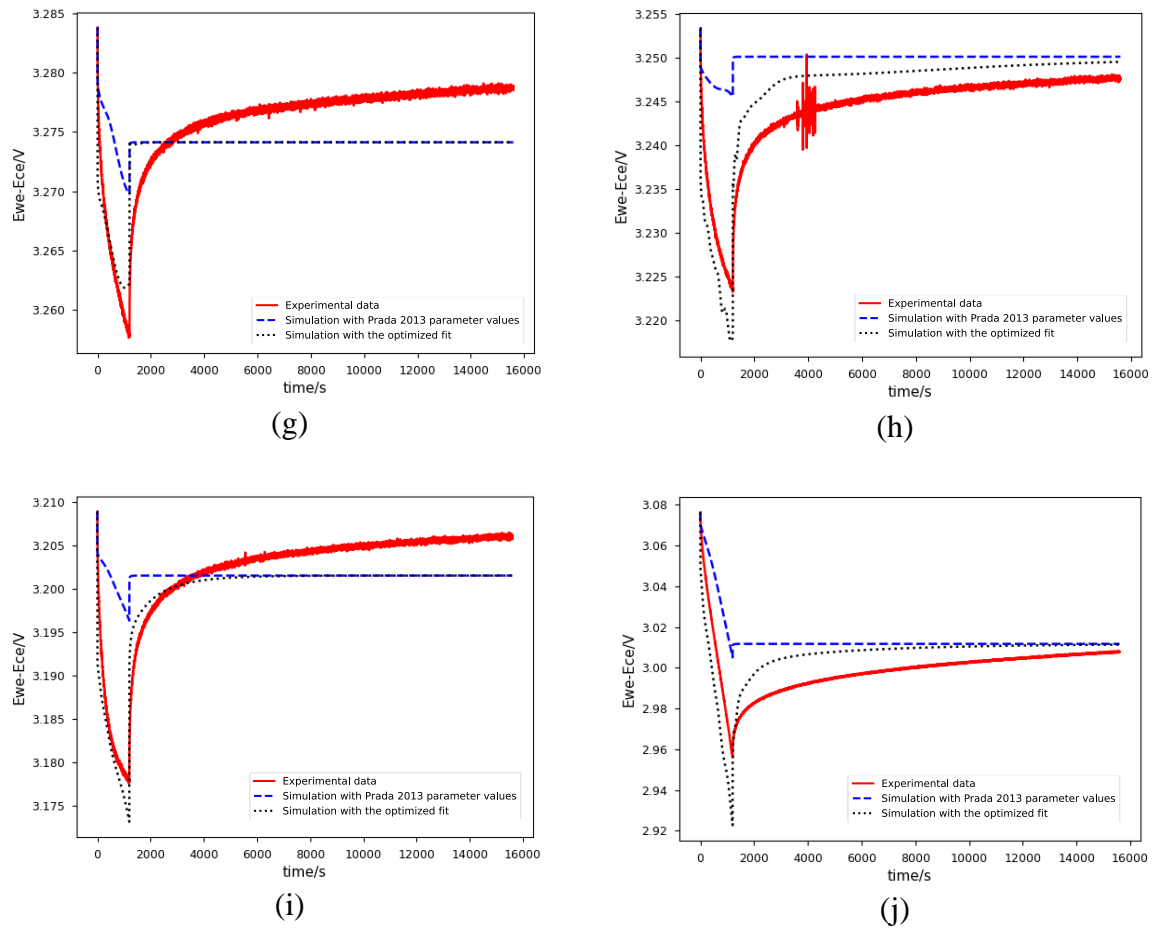
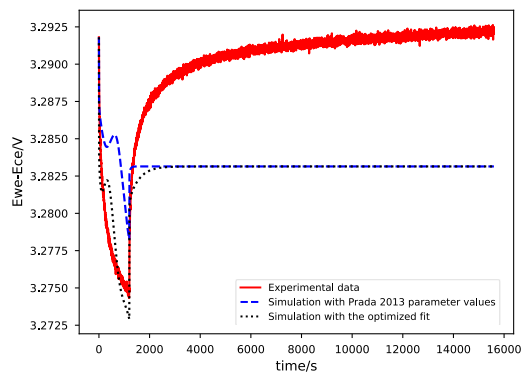*Figure 49, the experimental data, simulation with the Prada 2013 parameters as well as a simulation with fitted parameter values for each of the ten GITT pulses. The order of the plots represents the order of the pulses in the experiment.*

Table 20. *Parameter values found via curve fitting for each GITT pulse*

Orgin of values	$D_+ \left[m^2/s \right]$	$D_- \left[m^2/s \right]$	r_+ [m]	r_- [m]
Prada 2013	5.9e-18	3.3e-14	1e-08	5.86e-06
Pulse 1	2.89e-18	3.32e-14	4.65e-08	6.61e-06
Pulse 2	2.78e-18	4.43e-15	4.70e-08	4.01e-06
Pulse 3	5.90e-17	1.73e-14	7.90e-09	8.02e-06
Pulse 4	5.90e-19	6.68e-14	9.99e-08	2.49e-05
Pulse 5	1.08e-17	2.42e-13	2.86e-08	1.39e-05
Pulse 6	2.60e-17	3.71e-14	2.35e-08	1.45e-05
Pulse 7	6.28e-18	6.31e-14	3.17e-08	1.72e-05
Pulse 8	5.90e-17	3.30e-15	1.00e-09	2.39e-05
Pulse 9	5.22e-17	1.72e-14	4.99e-08	2.20e-05
Pulse 10	5.77e-17	1.10e-14	1.02e-09	3.10e-05
Mean	2.77e-17	4.95e-14	3.37e-08	1.66e-05
STDEV	2.62e-17	7.13e-14	2.97e-08	8.84e-06

Pulse test version 1
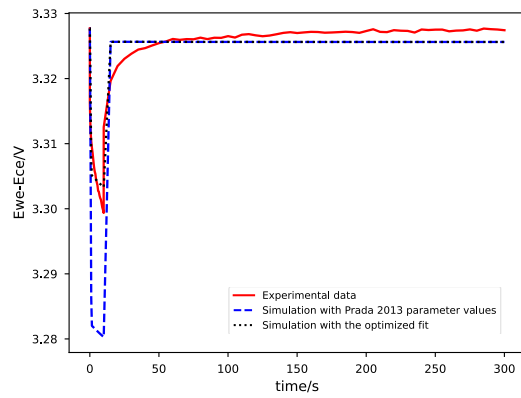
(a)
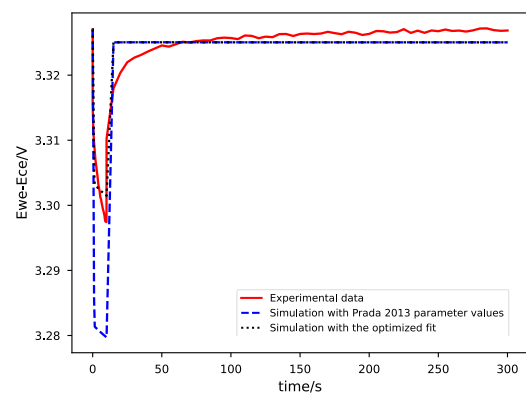
(b)
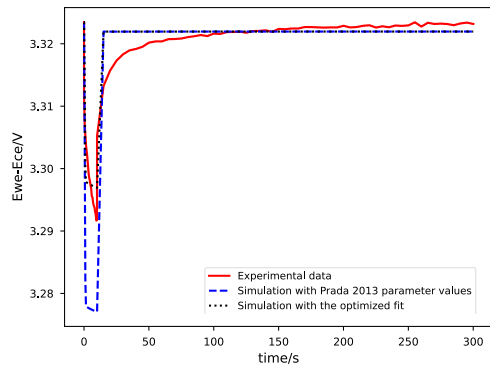
(c)
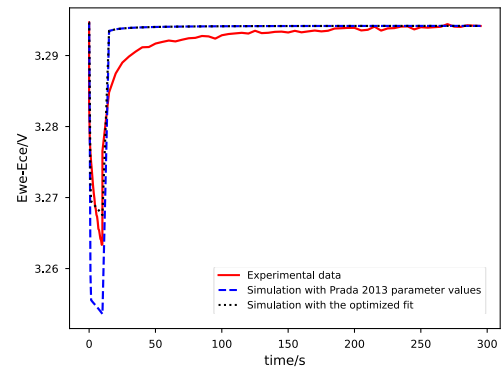
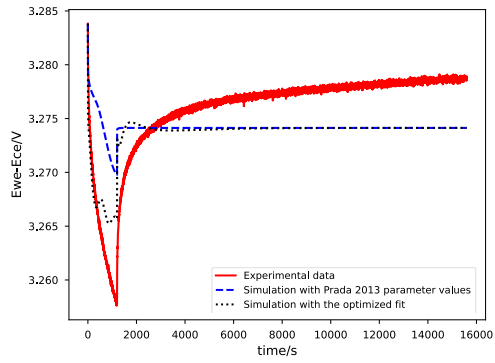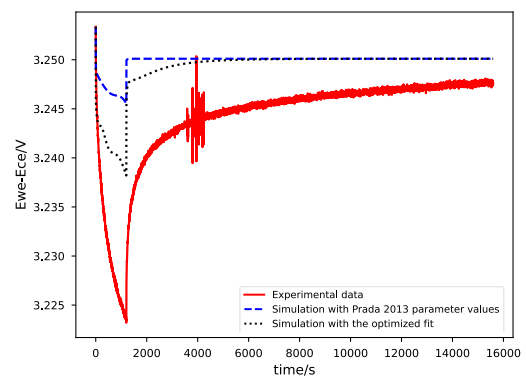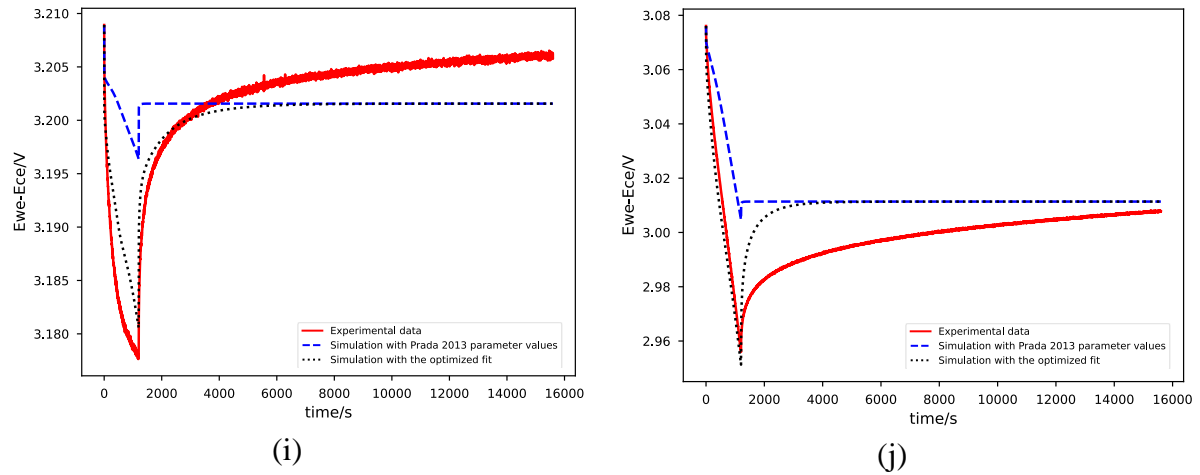(d)
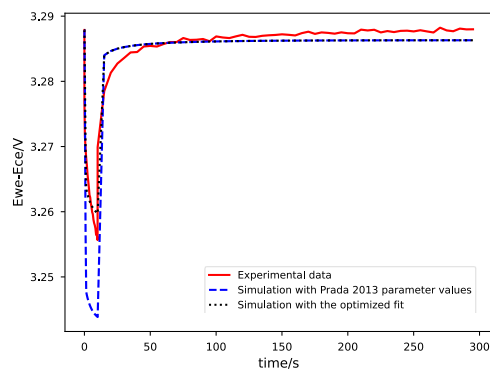
(e)
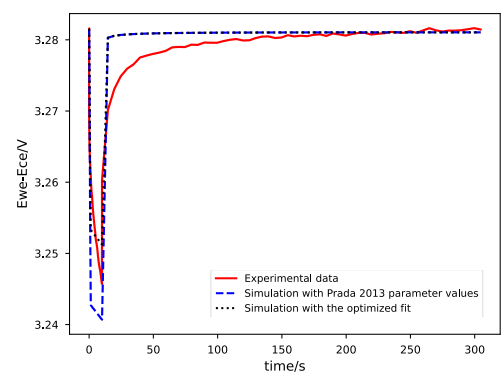
(f)
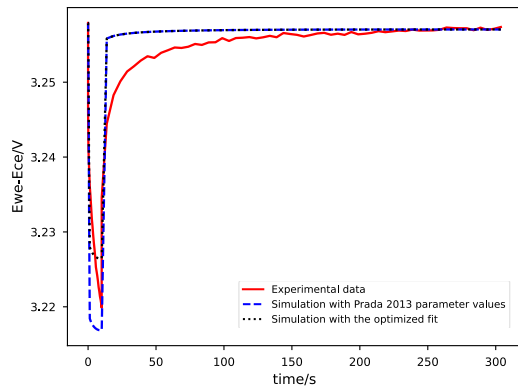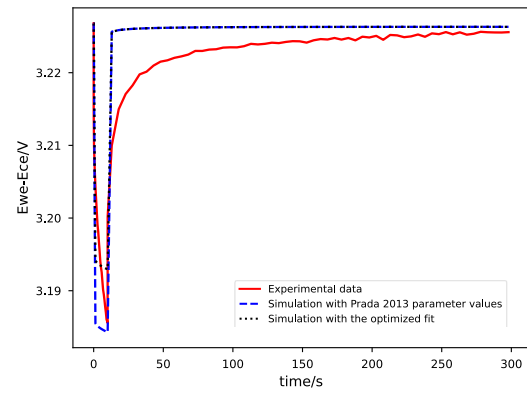
(g)   (h)

Figure 50, the experimental data, simulation with the Prada 2013 parameters as well as a simulation with fitted k_{f-} for eight of the C/2 pulses. The order of the plots represents the order of the pulses in the experiment starting with pulse nr 2.

Table 21. *The fitted parameter values from the simulation*

Orgin of values	k_{f-} [-]
PyBaMM	1
Opt. Train 2	2.26116222
Opt. Train 3	2.12878617
Opt. Train 4	1.96182209
Opt. Train 5	1.65668429
Opt. Train 6	1.81734881
Opt. Train 7	1.44308686
Opt. Train 8	1.38499424
Opt. Train 9	1.31931518
Mean	1.746649983
SDEV	0.330851661

Appendix D – Parametrization with changed r. bounds
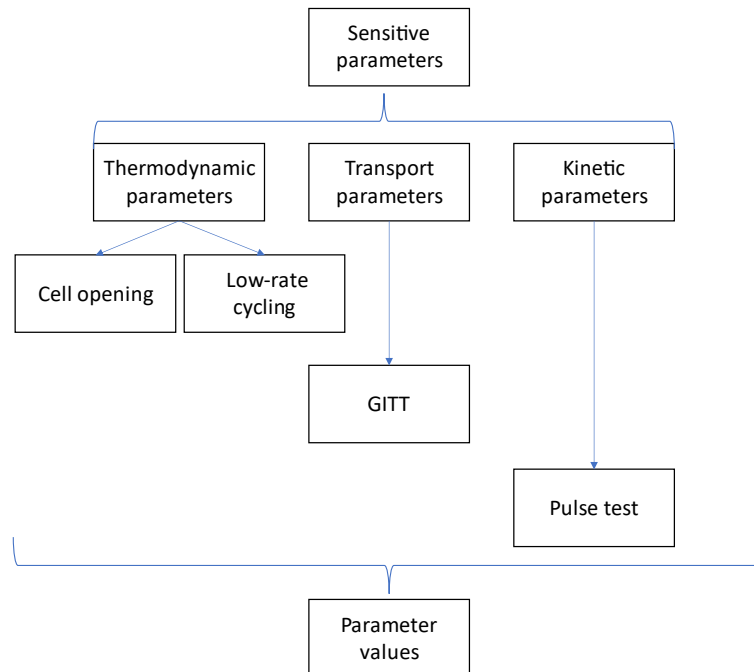
Figure 51. Alternative parametrization process

By changing the bounds for the negative particle radius from 5.86e-7 - 5.86e-5 m to1e-6 – 1e-5 m the results below are given.

GITT version 2

(a)

(b)

(c)
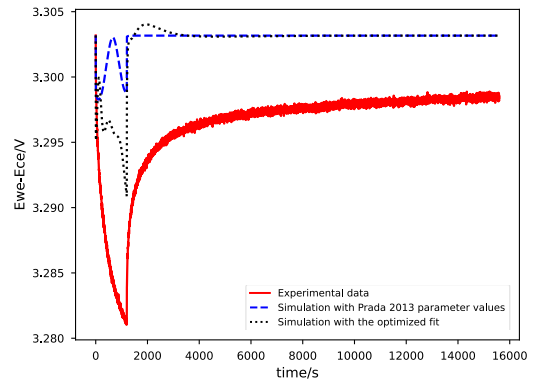
(d)

(e)
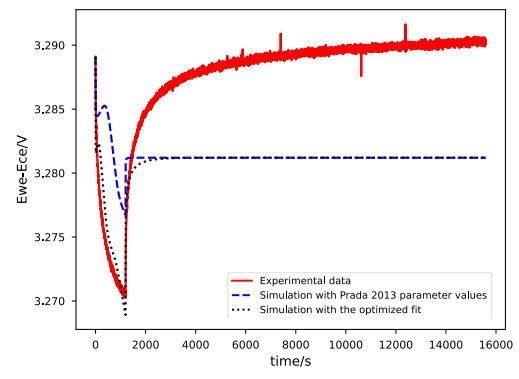
(f)

(g)

(h)

$$(i) \qquad\qquad (j)$$

Figure 50, the experimental data, simulation with the Prada 2013 parameters as well as a simulation with fitted parameter values for each of the ten GITT pulses. The order of the plots represents the order of the pulses in the experiment.

Table 22. *Parameter values found via curve fitting for each GITT pulse*

Orgin of values	$D_+ \left[m^2/s \right]$	$D_- \left[m^2/s \right]$	r_+ [m]	r_- [m]
Prada 2013	5.9e-18	3.3e-14	1e-08	5.86e-06
Pulse 1	1.85e-18	3.30e-15	5.32e-08	6.44e-06
Pulse 2	7.32e-18	9.33e-15	4.64e-08	4.11e-06
Pulse 3	5.90e-17	3.30e-13	3.14e-08	7.81e-06
Pulse 4	5.90e-19	3.30e-15	9.99e-08	9.99e-06
Pulse 5	7.91e-19	1.42e-14	9.86e-08	9.92e-06
Pulse 6	6.27e-19	9.92e-15	9.56e-08	9.79e-06
Pulse 7	5.90e-19	3.30e-15	1.00e-07	1.00e-05
Pulse 8	5.90e-19	3.30e-15	1.00e-07	1.00e-05
Pulse 9	5.90e-19	3.30e-15	9.99e-08	9.99e-06
Pulse 10	9.50e-19	5.15e-15	9.90e-08	9.95e-06
Mean	7.29e-18	3.85e-14	8.24e-08	8.80e-06
STDEV	1.73e-17	9.72e-14	2.59e-08	1.94e-06

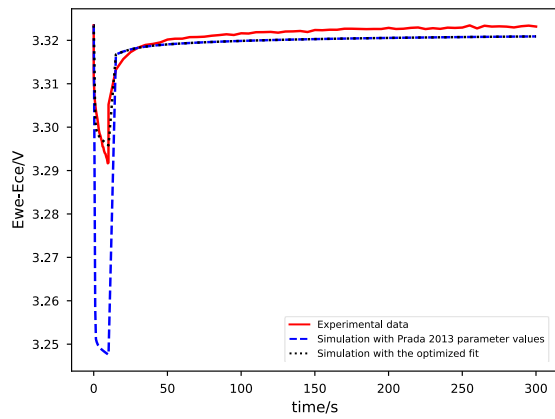The simulation for the ninth pulse had the best fit to the experimental data.
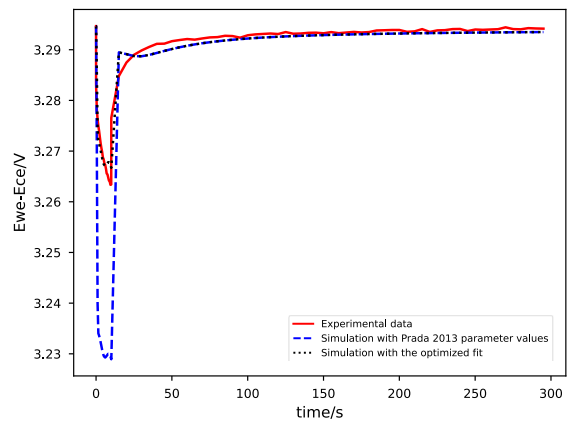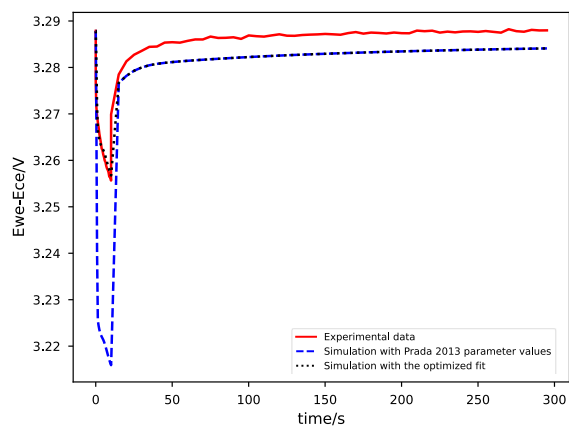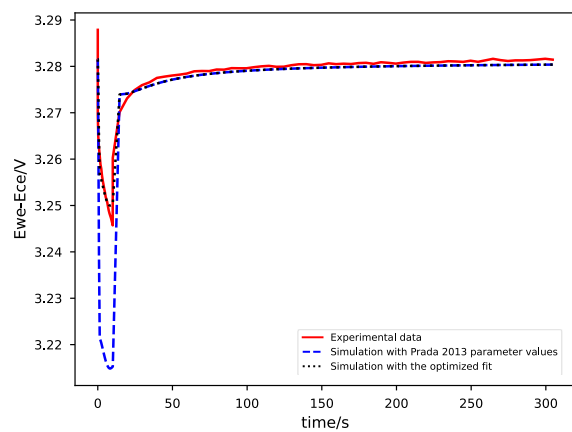
Pulse test version 2
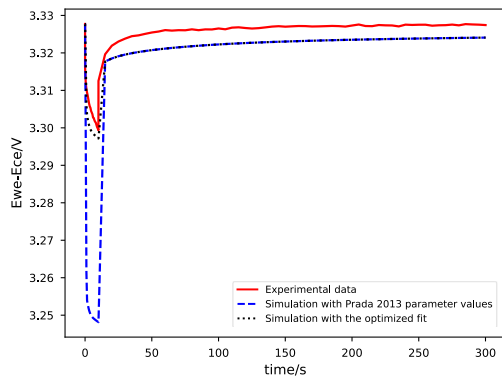
(a)
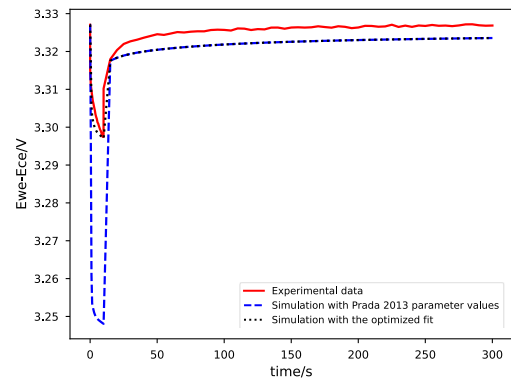
(b)

(c)

(d)

(e)

(f)
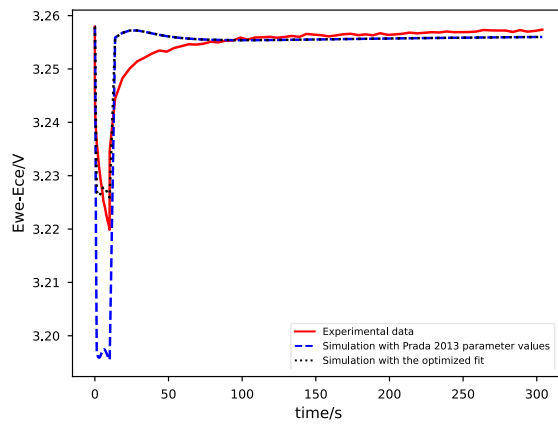
(g)
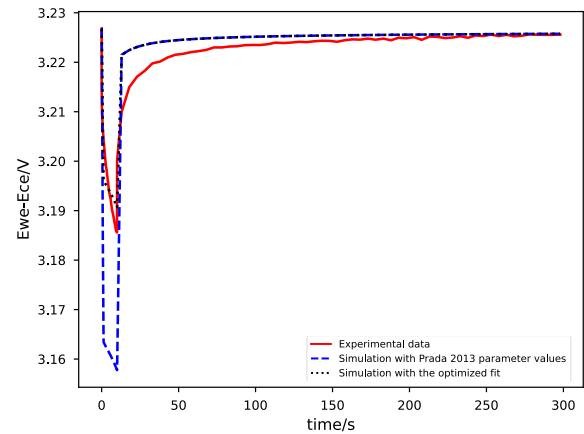
(h)

Table 23. *The fitted parameter values from the simulation*

Orgin of values	k_{f-} [-]
PyBaMM	1
Opt. Train 2	4.99
Opt. Train 3	4.99
Opt. Train 4	4.78
Opt. Train 5	3.41
Opt. Train 6	4.07
Opt. Train 7	3.02
Opt. Train 8	2.43
Opt. Train 9	2.56
Mean	3.78
SDEV	1.00

The simulation of the third pulse showed the best match with the experimental data.
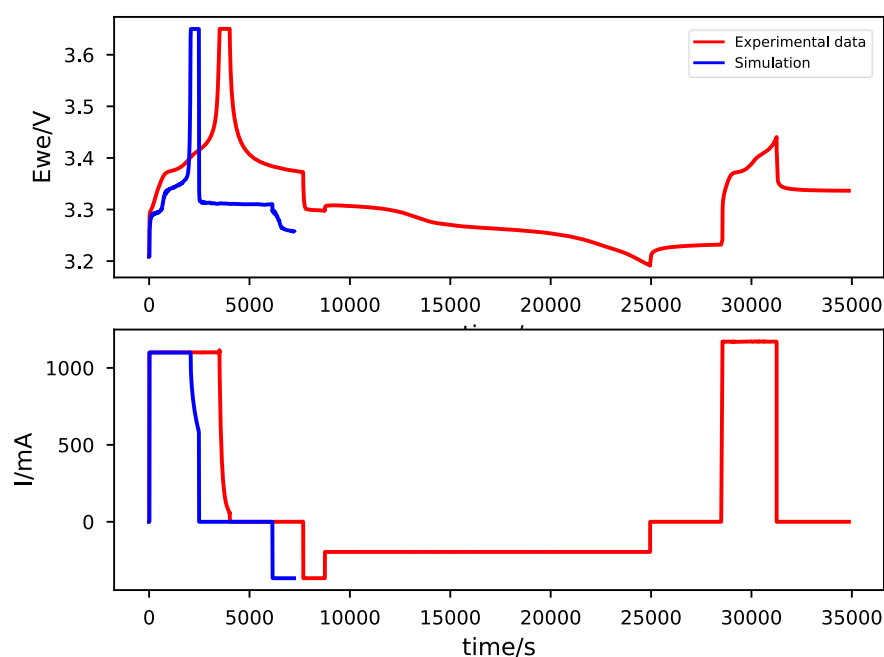
BEV validation curve version 2

Figure 52, Stopped simulation for alternative parameter values

The simulation is stopped since the experiment was infeasible. The maximum positive particle surface concentration' is triggered during 'Discharge at C/5.625 for 4.5 hours or until 2 V'. The error lies in the k_{f-} value now. Before the bounds of r_- is tightened this error message is shown and the problem is related to the negative particle radius.

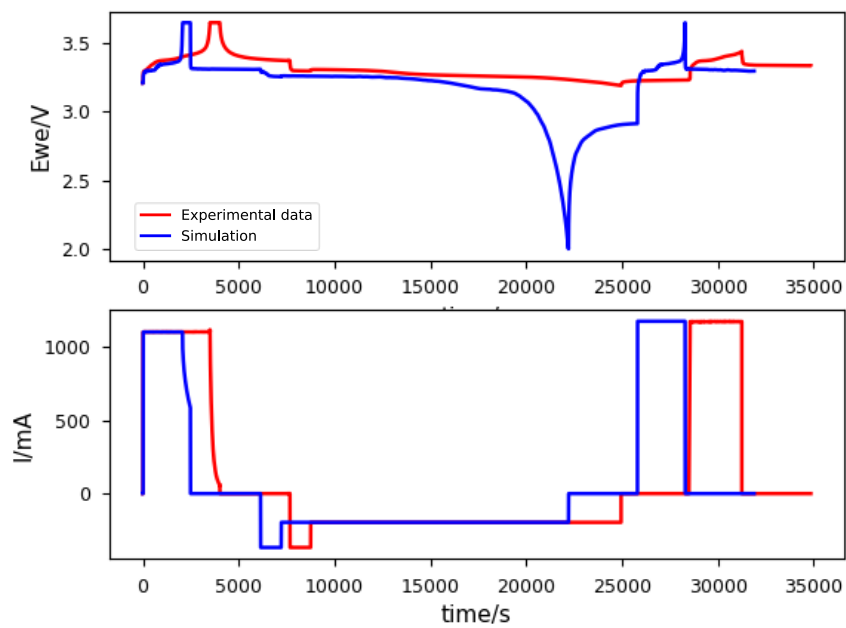## With k$_{f-}$ from pulse 6 instead

Figure 53, BEV simulation with alternative values except the k_f- is default.
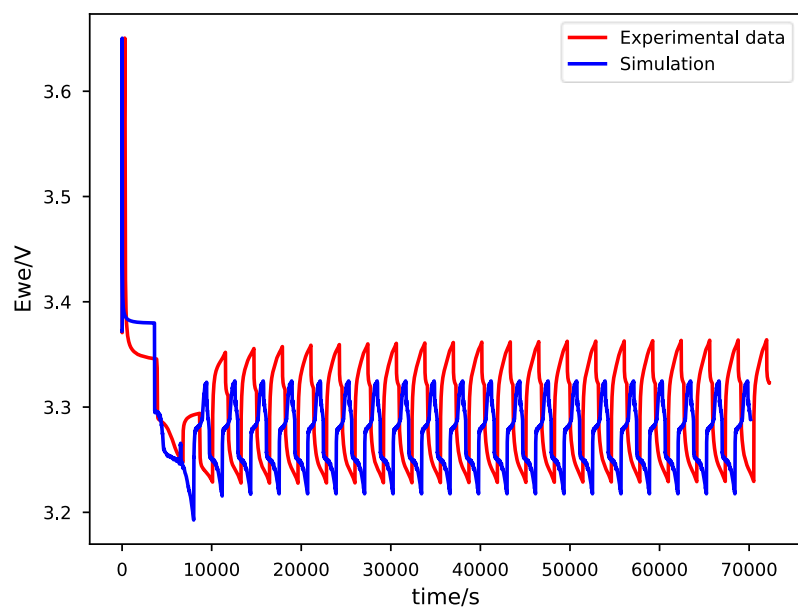
Mild hybrid validation curve version 2

Figure 54. Mild hybrid run with alternative parameter values.